

Visualization of Industrial 3DXCT Data

DISSERTATION

zur Erlangung des akademischen Grades

Doktor der technischen Wissenschaften

eingereicht von

Artem Amirkhanov

Matrikelnummer 0828422

an der
Fakultät für Informatik der Technischen Universität Wien

Betreuung: Ao.Univ.Prof. Dipl.-Ing. Dr.techn. Eduard Gröller
Dipl.-Ing. (FH) Dr.techn. Christoph Heinzl

Diese Dissertation haben begutachtet:

(Dr. Eduard Gröller)

(Dr. Klaus Mueller)

Wien, 27.09.2012

(Artem Amirkhanov)

Visualization of Industrial 3DXCT Data

DISSERTATION

submitted in partial fulfillment of the requirements for the degree of

Doctor of technology

by

Artem Amirkhanov

Registration Number 0828422

to the Faculty of Informatics
at the Vienna University of Technology

Advisors: Ao.Univ.Prof. Dipl.-Ing. Dr.techn. Eduard Gröller
Dipl.-Ing. (FH) Dr.techn. Christoph Heinzl

The dissertation has been reviewed by:

(Dr. Eduard Gröller)

(Dr. Klaus Mueller)

Wien, 27.09.2012

(Artem Amirkhanov)

Erklärung zur Verfassung der Arbeit

Artem Amirkhanov
Favoritenstrasse 9-11, A-1040 Vienna, Austria

Hiermit erkläre ich, dass ich diese Arbeit selbständig verfasst habe, dass ich die verwendeten Quellen und Hilfsmittel vollständig angegeben habe und dass ich die Stellen der Arbeit - einschließlich Tabellen, Karten und Abbildungen -, die anderen Werken oder dem Internet im Wortlaut oder dem Sinn nach entnommen sind, auf jeden Fall unter Angabe der Quelle als Entlehnung kenntlich gemacht habe.

(Ort, Datum)

(Unterschrift Verfasser)

Abstract

Three-dimensional X-ray computed tomography (3DXCT) is a powerful technique for generating a digital 3D volumetric representation of a specimen from a series of 2D X-ray penetration images. The main advantage of 3DXCT is its ability to detect both the interior and the exterior structure of a specimen in one single scan. Having been used in medical diagnostics for a long time, 3DXCT is increasingly employed in industry as a method for nondestructive testing and quality control. One especially challenging industrial application is metrology, which has to fulfill the demands of today's standards in industrial quality control. 3DXCT facilitates dimensional measurements of internal structures and of inaccessible parts of a component. However the successful industrial application of 3DXCT is constrained by a set of major problems:

Artifacts: Industrial 3DXCT systems face problems due to various types of artifacts. The appearance of artifacts in the 3DXCT scan data distorts its correlation to the actual evaluated industrial object and can lead to errors in measurements and false analysis results. Some types of artifacts are affected by the placement of a specimen in the scanning device.

Multi-material components: Another problem is occurring when multi-material components (MMCs) are inspected using industrial 3DXCT. Common industrial MMCs may contain metal parts surrounded by plastic materials. A major problem of this type of components is the presence of metal-caused streaking artifacts and distortions. They are located around metal components and significantly influence the material characterization. Furthermore these streaking artefacts and distortions may even prevent any further analysis (especially for the plastic components).

Measurements uncertainty: If metrology using 3DXCT is performed, the location of the specimen surface is estimated using the reconstructed 3D volume data. As opposed to mechanical or optical measurement techniques, the surface is not explicit and has a particular positional uncertainty depending on the artifacts and noise in the scan data and the surface extraction algorithm. Conventional CT metrology software does not account for the uncertainty of the data.

This thesis is devoted to the development of techniques overcoming the aforementioned problems of common industrial tasks involving the usage of 3DXCT for nondestructive testing and quality control with a main focus on industrial 3DXCT metrology. Several novel contributions utilizing visualization techniques and visual analysis methods were implemented in integrated tools assisting typical industrial 3DXCT tasks during different stages of the data pipeline.

This includes: a novel method for optimal specimen placement analysis taking into account the orientational stability, a visual analysis tool for metal artifact reduction with preview-based parameter estimation, and finally an integrated system visualizing measurements uncertainty on different levels-of-detail. The produced results are presented and evaluated using various industrial components and test parts.

Kurzfassung

Mit Hilfe der drei dimensionalen Röntgen-Computertomographie (3DXCT) kann aus einer Serie von zwei dimensionalen Röntgenbildern eine drei dimensionale volumetrische Repräsentation eines Prüfkörpers erstellt werden. Somit besteht ein großer Vorteil dieser Technik darin, dass in nur einem Scanvorgang sowohl innere, als auch äußere Strukturen eines Prüfkörpers detektiert werden können. 3DXCT ist schon seit längerem eine bekannte und vielgenutzte Technik im Bereich der medizinischen Diagnostik. Nun findet sie auch Anwendung im Bereich der Industrie, wo sie zur zerstörungsfreien Werkstoffprüfung und Qualitätskontrolle eingesetzt wird. Hier erleichtert 3DXCT Dimensionsmessungen von inneren und somit schwer zugänglichen Strukturen in industriell gefertigten Werkstücken. Trotz dieser Vorteile stellt die Anwendung von 3DXCT in der Industrie eine besondere Herausforderung dar, weil speziell im Bereich der Messtechnik hohe Qualitätsstandards erfüllt werden müssen. Die Hauptprobleme bei der industriellen Verwendung von 3DXCT sind:

Artefakte: Durch unterschiedliche Einflüsse (z.B. die Platzierung des Prüfkörpers im 3DXCT-Scanner) können in den Datensätzen verschiedene Arten von Artefakten auftreten. Diese können später nicht nur die Scandaten des eigentlichen Prüfkörpers verfälschen, sondern können auch zu Fehlern in den Mess- und Analyseergebnissen führen.

Verbundmaterialien: Viele industrielle Komponenten werden aus verschiedenen Materialien gefertigt, die während der Produktion miteinander verbunden werden. Häufig werden dabei Metallteile mit einer Verkleidung versehen, welche zumeist aus Kunststoff bestehen. In solchen Fällen kommt es dann zu Artefakten und Verzerrungen in den Daten, welche durch die metallischen Teile verursacht werden. Solche Störungen können später die Analyse der nicht-metallischen Materialien beeinträchtigen, oder sie im schlechtesten Fall sogar unmöglich machen.

Messunsicherheit: Um Messungen in 3DXCT-Daten durchführen zu können, muss zuerst anhand der drei dimensional Volumsdaten bestimmt werden, welche Daten die Oberfläche des Prüfkörpers repräsentieren. Aufgrund der Tatsache, dass die Oberfläche nicht explizit definiert ist und gegebenenfalls vorhandene Artefakte und Verzerrungen in den Daten die Analyse erschweren, ist die Messung der Oberfläche immer mit einer gewissen Unsicherheit behaftet. Diese Messunsicherheiten werden von aktuellen Softwareprodukten, welche in der Messtechnik Anwendung finden, nicht berücksichtigt.

Im Rahmen dieser Dissertation werden neue Methoden zur industriellen Verwendung von 3DXCT für zerstörungsfreie Werkstoffprüfungen und Qualitätskontrollen vorgestellt, welche Lösungen für die oben erwähnten Probleme anbieten. Ein besonderer Schwerpunkt liegt dabei auf der Verwendung von 3DXCT im Bereich der Messtechnik. Ziel war es, Methoden zu entwickeln, welche die einzelnen Stufen in der Erstellung und Analyse industrieller 3DXCT-Daten unterstützen und verbessern. Basierend auf Technologien aus den Bereichen Visualisierung und Visual Analytics wurden neue Methoden implementiert und in Werkzeuge integriert, die den Anwender in typischen 3DXCT Auswertungen unterstützen sollen. Diese umfassen: eine neue Methode zur optimalen Platzierung von Prüfkörpern im 3DXCT-Scanner unter Berücksichtigung der Stabilität der Platzierung, ein System zur visuellen Analyse und Reduktion von Artefakten, welche durch das Vorhandensein von metallischen Teilen verursacht wurden, und ein System zur visuellen Darstellung von Messunsicherheiten in den Daten in verschiedenen Detaillierungsgraden. In dieser Arbeit werden die verwendeten Methoden beschrieben und ihre Anwendungen anhand von verschiedenen industriellen 3DXCT-Datensätzen dargestellt.

Contents

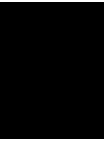
1	Introduction	1
1.1	Quality Control and Nondestructive Testing	1
1.2	Industrial Metrology and Geometric Tolerancing	1
1.3	Industrial 3DXCT	3
1.3.1	3DXCT Scanning Workflow	3
1.3.2	Applications	7
1.3.3	Artifacts	7
1.4	Contributions of the Thesis	8
2	Visual Optimality and Stability Analysis of 3DXCT Scan Positions	11
2.1	Introduction	11
2.2	Related Work	15
2.3	Penetration-Length Analysis	17
2.4	Radon-Space Analysis	19
2.4.1	Background and Theory	19
2.4.2	Radon-space Analysis	20
2.5	Placement-Stability Analysis	21
2.6	Data Visualization, Exploration and Visual Analysis	21
2.6.1	Visualization of Placement Parameters.	21
2.6.2	Comparative Visualisation of Placement Parameters	22
2.6.3	Feature Selection	22
2.6.4	Color-Coding Bad Areas	23
2.6.5	Penetration-Length Histograms	23
2.6.6	Visualization of Ray Subsets	25
2.7	Implementation and Performance	26
2.7.1	Parallelization	28
2.7.2	Performance	28
2.8	Results	28
2.8.1	Evaluation	28
2.9	Conclusion	34
3	Projection-Based Metal-Artifact Reduction for 3DXCT	37
3.1	Introduction	37

3.2	Related Work	40
3.3	Projection-Based Metal-Artifact Reduction	43
3.3.1	Reconstruction	46
3.3.2	Material Separation	46
3.3.3	Forward Projection	47
3.3.4	Interpolation	48
3.3.5	Fusion	50
3.4	Visual-Analysis Tool for Metal-Artifact Reduction	50
3.4.1	Visual Parameter Estimation for Material Separation	51
3.4.2	Visual Result Exploration	53
3.5	Implementation	55
3.6	Results	55
3.7	Conclusion	61
4	Fuzzy CT Metrology: Dimensional Measurements on Uncertain Data	63
4.1	Introduction	63
4.2	Related Work	67
4.3	Geometric Tolerancing	69
4.4	Measuring Procedure	72
4.5	Statistical Analysis	72
4.5.1	Bayesian Classification	73
4.5.2	Material-Interface Probabilities	73
4.6	3D Labels	74
4.7	Reference Shapes	78
4.8	Measurement Plots	80
4.8.1	Uncertainty Aura	80
4.8.2	Uncertainty as Context	81
4.9	Implementation	81
4.10	Results	81
4.11	Conclusions	86
5	Summary	87
	Bibliography	91
	Curriculum Vitae	99
	Contact Information	99
	Personal Details	99
	Education	100
	Employment History	100
	Publications	101

Preface

This thesis results from three years of research at the Institute of Computer Graphics and Algorithms, Vienna University of Technology done from October 2009 until September 2012. I want to thank Meister Eduard Gröller and Christoph Heinzl who were supervising this work. It would not have been possible without their kind guidance, motivation, and expertise. I also want to thank Stefan Bruckner, Muhammad Muddassir Malik, Martin Haidacher, Peter Rautek, Erald Vuçini, Andrej Varchola, Gabriel Mistelbauer, Peter Mindek, Peter Sikachev, Johanna Schmidt, Alexey Karimov, Michael Reiter, Johann Kastner, Dietmar Salaberger, Marius Gavrilescu, Paul Herghelegiu, Gibs the Kaiser of Imperium, Anita Mayerhofer-Sebera, Stephan Plepelits, Andreas Weiner, and all the others for their valuable help and creating such a great environment during all this time. I am especially grateful to my beloved family in Ufa and to my girlfriend Ekaterina whose support and love I could always feel despite being so far away. This thesis is dedicated to the old blue sofa in our office for providing me and other members of the Vis Group with precious rest hours during the deadline rushes.

The presented work has been funded by the Bridge-Project SmartCT and the K-Project ZPT (<http://www.3dct.at>) of the Austrian Research Promotion Agency (FFG).



Introduction

1.1 Quality Control and Nondestructive Testing

The complexity of modern industrial products increases continuously to keep up with the high demands and requirements imposed by the industry. Greater robustness and durability, lighter weight, larger functionality, and lower costs are only a few of the demands on new industrial materials and components. In this respect, testing methods which allow thorough, precise, and efficient quality control are needed.

Quality in general is the standard of something as measured against other things of a similar kind; the degree of excellence of something. [1] In engineering and industrial production quality control defines the quality using custom requirements and specifications of the production process. *Nondestructive testing* (NDT) covers a wide group of analysis techniques used in science and industry to evaluate the properties of a material, a component or a system without causing damage [11]. The ability to preserve the integrity and functionality of the inspected specimen makes NDT methods highly cost-effective and useful for evaluation, troubleshooting, and research. NDT is applied in a broad range of engineering fields and includes various methods, e.g., ultrasonic testing, visual testing, radiographic testing, acoustic emission monitoring, and coordinate measurements.

1.2 Industrial Metrology and Geometric Tolerancing

Geometric tolerancing and dimensional measurements are well established methods in industrial quality control. They are the basis of assuring the manufacturing quality of industrial products. To achieve the geometric tolerancing and dimensional measurements of the features of interest, first, a measurement plan has to be set up. The measurement plan incorporates measurement features as required for the quality control of the manufacturing processes. After the measurements are performed and all measurement features are evaluated, properties as line straightness, flatness or circularity are computed. These properties are analyzed and interpreted using visual

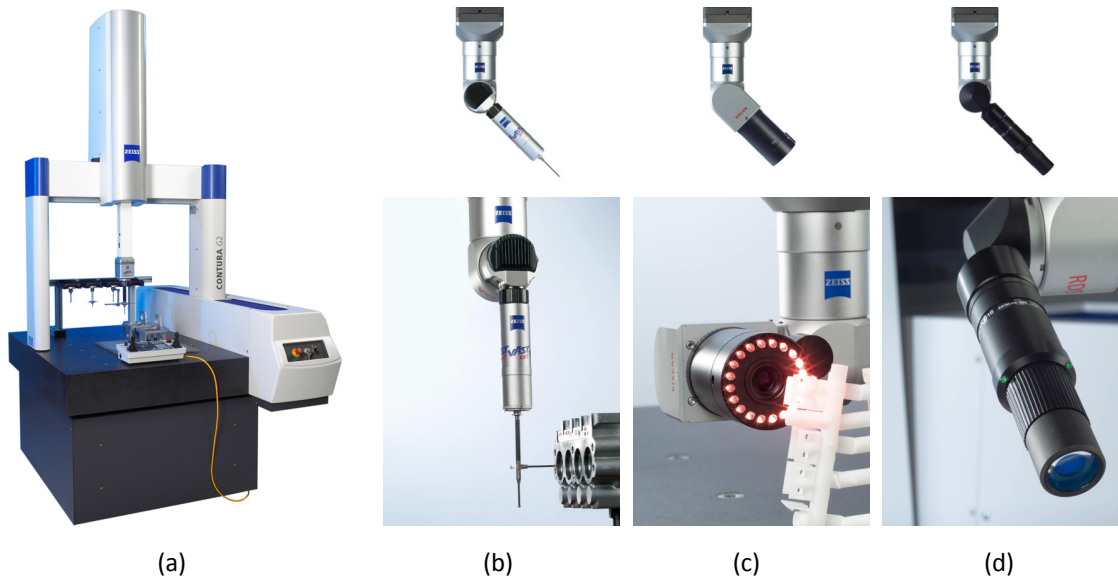


Figure 1.1: Bridge-type coordinate measurement machine from Zeiss (a) with interchangeable probes. Tactile stylus sensor (b), camera-based 2D optical probe (c), and optical diode stylus probe (d) are shown (images are courtesy of Carl Zeiss Industrial Metrology).

representations as line profiles or polar plots. In most cases tactile measurements using *coordinate measurement machines* (CMMs) or optical coordinate measurement techniques are the methods of choice. An example of a CMM with interchangeable tactile and optical sensors is given in Figure 1.1. The tactile sensor (Figure 1.1b) is using a stylus to directly contact the surface of a measured article. The stylus is a measuring tool in the shape of a shaft with a sphere of an exactly known radius on the tip. The shaft can be made of carbon fiber reinforced polymer or of the steel and the sphere can be made of ruby depending on the construction and manufacturer. During the movement of the stylus along the surface, its coordinates are recorded with high precision. The measured 3D point set is then processed in a specialized measurement software. This software derives geometrical tolerances like planarity or circularity for the measured features corresponding to the measurement plan. An alternative to the tactile probing is a camera based optical sensor (Figure 1.1c). Such sensors utilize high definition cameras with interchangeable lenses: First, an adaptive illumination system projects patterns on the objects. Then, in the second step, the resulting images are recorded. Finally, the images are processed by the software and the required measurements are performed using triangulation algorithms. Such sensor systems are especially suitable for measurement of parts with very small or two-dimensional geometries and/or soft materials, e.g., micro schemes, circuit boards or rubber parts. The sensor in Figure 1.1d is a compromise between tactile and optical camera probes. It behaves almost as a tactile stylus but does not require a direct contact with the surface as it utilizes a LED diode stylus system.

The precisions CMMs deliver is calibrated and standardized in accordance to valid standards of industrial metrology. However, there are several significant disadvantages that tactile and optical sensors are suffering from:

- applying tactile measurement systems to soft and deformable materials or specimens with extremely fragile structure is problematic
- optical sensors are experiencing problems with measuring non-planar geometries, and with highly glossy, transparent, or reflective materials
- both tactile and optical probing tools are not able to measure internal features of the inspected specimen.

1.3 Industrial 3DXCT

Three-dimensional X-ray computed tomography (3DXCT) is a powerful technique for generating a digital 3D volumetric dataset of a specimen from 2D projections (X-ray penetration images). The main advantage of 3DXCT is its ability to capture both the interior and the exterior structures of a specimen including a detailed material characterization in one single scan. Its characteristics imply the following important advantages over conventional CMM metrology:

- 3DXCT may be used for a *wide range of materials* without applying any restrictions or taking compromises. Transparent, reflective, soft, and deformable materials may be characterized, measured and analyzed.
- 3DXCT allows a *full characterization* of the specimen's material interfaces including *exterior and interior* structures without destroying or disassembling it. Inner or hidden features like pores, cracks, and cavities may be detected and evaluated.

1.3.1 3DXCT Scanning Workflow

The general overview of the 3DXCT data acquisition and processing workflow is shown in Figure 1.2. It starts with the *scan planning and setup*. During this stage a specimen to be scanned is chosen. A set of optimal scan parameters has to be defined based on the size, the material or their combination, as well as on the geometry of the selected part. The scan parameters include amongst others:

- voltage and current for the X-ray tube
- number of projections
- integration time
- orientation and position of the specimen in the scanning device.

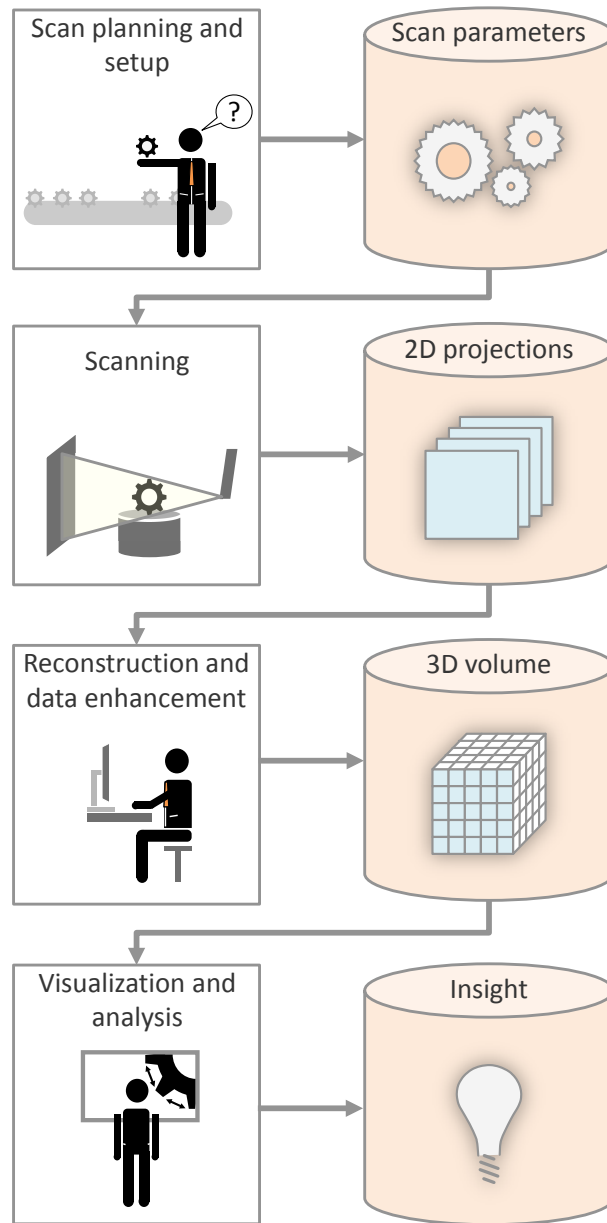


Figure 1.2: Industrial 3DXCT scanning workflow overview.

Finding an optimal set of scan parameters may lead to significantly better scanning results by improving contrast and by reducing noise and the amount of artifacts. After the parameters are defined, the scanning device is set up correspondingly.

The next step is the *scanning* itself. It is the main data acquisition step of the pipeline. Figure 1.3 shows the typical scheme of an industrial 3DXCT system. The test specimen is placed

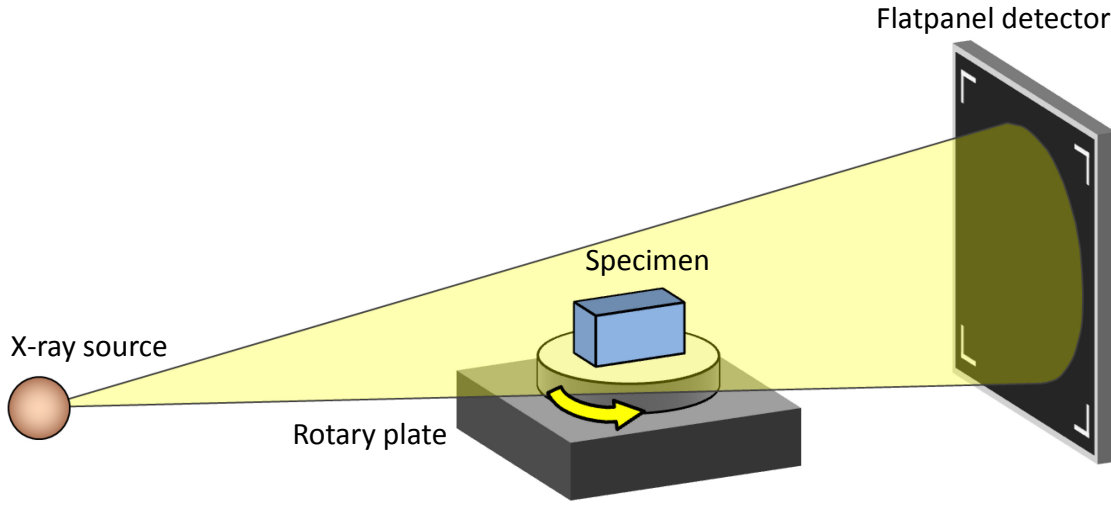
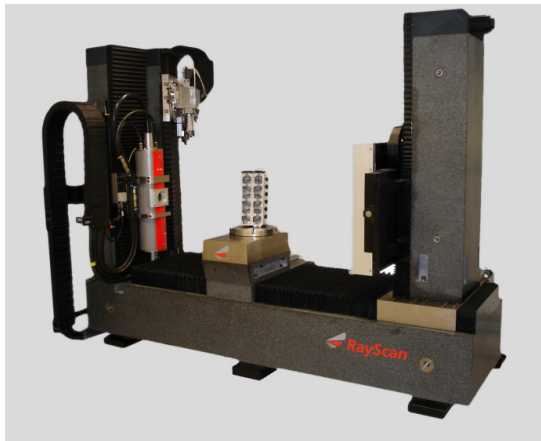
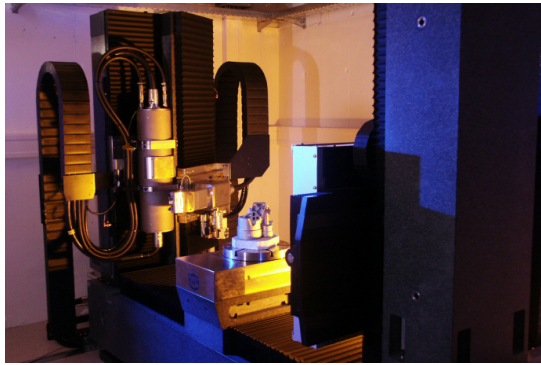


Figure 1.3: Geometry of a 3DXCT circular cone-beam scanning system.

on a rotary plate, which is between an X-ray radiation source and a flat panel detector. The cone-beam radiation generated by the source is penetrating the specimen. On the other side of the setup the flatpanel detector is located. It detects the X-ray attenuation through the specimen and records it in a 2D projection image. Pixels of a 2D projection contain corresponding grayscale attenuation values. In order to obtain all the necessary projections of a specimen for a full scan, the specimen is rotated stepwise on the rotary plate. A rotation of 360 degrees is typically used for a full reconstruction of the 3D dataset. The rotation corresponds to a circular trajectory of the cone-beam X-ray source. This circular cone-beam (CB) scanning scheme is commonly used in industrial 3DXCT and is thus considered in this work. Usually from 360 to 1440 projections of the specimen are taken depending on the specimen, task and scanning parameters. This requires typical scan times from 15 minutes to one hour [20]. Figure 1.4 shows the 3DXCT scanning devices, which were used to generate data sets presented in this work. The device in Figure 1.4a is used to scan larger industrial components. It features a dual X-ray source setup typically used to scan industrial components with diameters from 5 up to 600 mm. The system has two X-ray sources: The microfocus X-ray source features lower acceleration voltages, and yields better resolutions. The macrofocus X-ray source is able to penetrate bigger specimens due to the higher energy, but has a lower resolution. The device in Figure 1.4b is used for scanning smaller specimens like material probes with diameters smaller than 68 mm. The system is equipped with a high resolution flatpanel detector and with an X-ray source reaching a focal point size less than $1\ \mu\text{m}$.

The next step is the *reconstruction and data enhancement* step. A 3D volumetric data set is reconstructed from the set of projections by applying a reconstruction algorithm. Filtered backprojection as described in Feldkamp et al. [16] is the reconstruction method that is widely used for industrial 3DXCT cone-beam scanning.



HWM RayScan 250E:	
<i>X-ray source (dual):</i>	microfocus 10 – 250 kV macrofocus 50 – 450 kV
<i>Focal spot:</i>	3 – 250 μm ; 0.4 mm
<i>Detector:</i>	2048 \times 2048
<i>Object size:</i>	1 – 600 mm; 1 – 1500 mm

(a)

Phoenix X-ray Nanotom 180:	
<i>X-ray source:</i>	up to 180 kV
<i>Focal spot:</i>	< 1 μm
<i>Detector:</i>	2300 \times 2300
<i>Object size:</i>	up to 120 mm

(b)

Figure 1.4: Industrial 3DXCT scanning devices at the Upper Austrian University of Applied Sciences - Wels Campus.

Finally, the reconstructed 3D volume is visually represented and is used to perform measurements or material characterization and analysis during the *visualization and analysis* step. Visualizations of the 3DXCT data serve a specific purpose: they allow experts to get insight into the quality of a specimen by visually exploring attributes and parameters of the data through of

3D or 2D renderings. Additionally, various computational tools and algorithms allow to estimate or derive such parameters and attributes. The final goal of the industrial 3DXCT pipeline is to provide domain experts with useful insights into the quality or properties of the evaluated industrial object.

1.3.2 Applications

Industrial 3DXCT has its own peculiarities and problems compared to medical 3DXCT. Medical 3DXCT systems are optimized on a well defined application area with well-known materials such as blood, tissue, or bone. As a young application field, industrial 3DXCT does not yet have established protocols or generally applicable metrology standards that can be relied upon.

The ability to capture internal and external interfaces of different materials makes 3DXCT highly convenient for *material analysis* and *characterization of material interfaces*. Inspection of *multi-material components* (MMCs) is challenging for such an analysis. MMCs are specimens, which are manufactured from different materials with high density variations, e.g., plastic-metal components or composite materials with metal inlays. Such combinations of weakly and strongly X-ray absorbing materials in a single industrial component are very common in engineering. For MMCs one important goal of data analysis is material characterization. Another key goal is the interface detection to measure dimensional features of interest in each of the materials. A high dynamic range of the attenuation values in the scan data causes a variety of artifacts and complicates the characterization of component and material. Additionally, the process of tuning a 3DXCT scanning device for MMCs is getting more complex and tedious.

The 3DXCT is also a very attractive tool for *metrology* purposes. It allows performing measurements of parts not accessible by tactile or optical systems as well as of not-metrology-friendly objects, e.g., transparent, reflecting, soft, or deformable materials. When employing 3DXCT, it is not required to disassemble a specimen. Thus, this technique is increasingly employed in industrial metrology, as the spatial resolution and the mechanical precision of modern 3DXCT systems are continuously improved and both are nowadays high enough to perform measurements at the required level of accuracy.

1.3.3 Artifacts

One of the most critical issues in the area of metrology using industrial 3DXCT is the problem of artifacts. Artifacts are artificial structures in the reconstructed dataset, which do not correspond to structures of the scanned specimen. In the area of metrology artifacts may seriously affect or even prevent reliable measurements [20]. They show up as greyvalue variations and deviations in the reconstructed dataset. The presence of artifacts generates distortions in the resulting volume dataset and produces measurement errors. In severe cases the insufficient quality of the resulting data might prevent any further exploration and analysis. Some of the most prominent artifact types are noise, streaking, beam hardening, partial volume effects, aliasing, and scattered radiation [26]. Examples of common artifact types are given in Figure 1.5. In cone-beam CT the characteristics and magnitude of an artifact are mainly determined by the specimen's geometry, its position and its orientation in the cone beam, the scan parameters and the specimen's material combination.

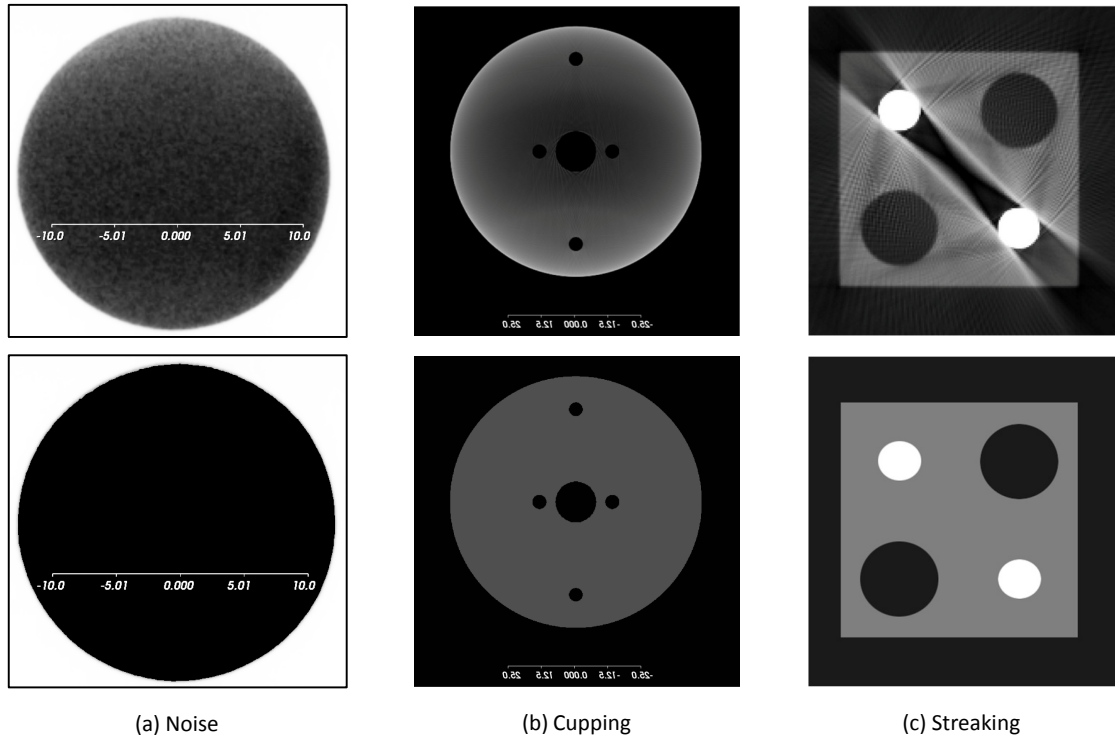


Figure 1.5: Common types of artifacts present in industrial 3DXCT data. Slices of 3D volumes are shown. Data with (top) and without (bottom) artifacts are shown.

For polychromatic radiation, as used in 3DXCT, the correlation between attenuation and penetration length is nonlinear. The polychromatic spectrum of an X-ray beam is hardened as it traverses through the material of a specimen. This means that higher energy photons pass through the material, while lower energy photons are absorbed. What remains is a modified (a hardened) spectrum containing mainly the higher energy portions. Thus, thicker objects reduce radiation by a smaller amount per unit length compared to thinner objects [20]. This effect is called beam-hardening. Beam-hardening causes two types of artifacts: cupping artifacts (see Figure 1.5b) and streaking artifacts, i.e., bright or dark bands or streaks between dense objects in the image (see Figure 1.5c) [7]. Streaking artifacts are commonly known as metal artifacts since they usually appear when the low-absorbing material of a specimen contains metal inclusions such as pins, screws, or nails.

1.4 Contributions of the Thesis

Industrial 3DXCT for NDT and quality control shows a list of prominent advantages over other conventional methods such as CMM metrology. The ability to evaluate industrial products with a broader range of material compositions, including characterization of external and internal

interfaces in a single scan, attracts an increasing number of companies from a wide range of engineering fields as mechanical and electrical engineering. 3DXCT with its relatively low costs and high versatility turns out to be highly beneficial in various areas, e.g., aeronautics, automotive, and electronic-circuitry industries. Driven by such applications 3DXCT scanning devices are receiving continuous improvements by means of higher accuracy and resolution, faster scanning times and better data processing and handling. However, industrial 3DXCT is still subject to various drawbacks. Moreover achieving optimal results is not yet completely automated and heavily relies on the knowledge of domain experts.

In this work we improve different steps of the 3DXCT data acquisition and processing pipeline by providing meaningful visualizations and visual analysis tools. We consider NDT and metrology application scenarios with the main focus on process automation, artifact reduction, and gaining additional insights into the data. To address these issues we present three novel methods:

- **Visual Optimality and Stability Analysis of Scan Positions** targets finding an optimal orientation of the specimen on the rotary plate using its 3D CAD model. This contributes to the *scan planning and setup* stage of the 3DXCT workflow.
- **Projection-Based Metal-Artifact Reduction** deals with reduction of metal artifacts in multi-material components containing metal using the projection data. This contributes to the *reconstruction and data enhancement* stage of the 3DXCT workflow.
- **Fuzzy CT Metrology: Dimensional Measurements on Uncertain Data** presents a system, which employs uncertainty visualizations to provide additional information on the uncertainty of 3DXCT measurements. This contributes to the *visualization and analysis* stage of the 3DXCT workflow.

Visual Optimality and Stability Analysis of 3DXCT Scan Positions

Industrial cone-beam X-Ray computed tomography (CT) systems often face problems due to artifacts caused by a bad placement of the specimen on the rotary plate. This chapter presents a visual-analysis tool for CT systems which provides a simulation-based preview and estimates artifacts and deviations of a specimen's placement using the corresponding 3D geometrical surface model as input. The presented tool identifies potentially good or bad placements of a specimen and regions of a specimen which cause the major portion of artefacts. The tool is used for a preliminary analysis of the specimen before CT scanning, in order to determine the optimal way of placing the object. The analysis includes: penetration lengths, placement stability and an investigation in Radon space. Novel visualization techniques are applied to the simulation data. A stability widget is presented for determining the placement parameters' robustness. The performance and the comparison of results provided by the tool compared with real world data is demonstrated using two specimens [2] [21].

2.1 Introduction

In cone-beam CT the characteristics and magnitude of an artifact are mainly determined by the specimen's geometry, its position and orientation in the cone beam, the measurement parameters and the specimen's material combination. In this chapter we focus on artifacts depending on the specimen placement on the rotary plate. Finding an optimal specimen placement is crucial for the technicians. In many cases picking the appropriate specimen placement reduces the amount of artifacts and significantly improves measurement accuracy. An example of a bad and a good positioning of a specimen is given in Figure 2.1. Currently, the optimal placement of a specimen is based on the knowledge and experience of the technicians operating the 3DXCT machine. The application of this knowledge to specimens with a complex geometry is subjective and quite difficult even for the domain specialists. Scanning a specimen several times in order to

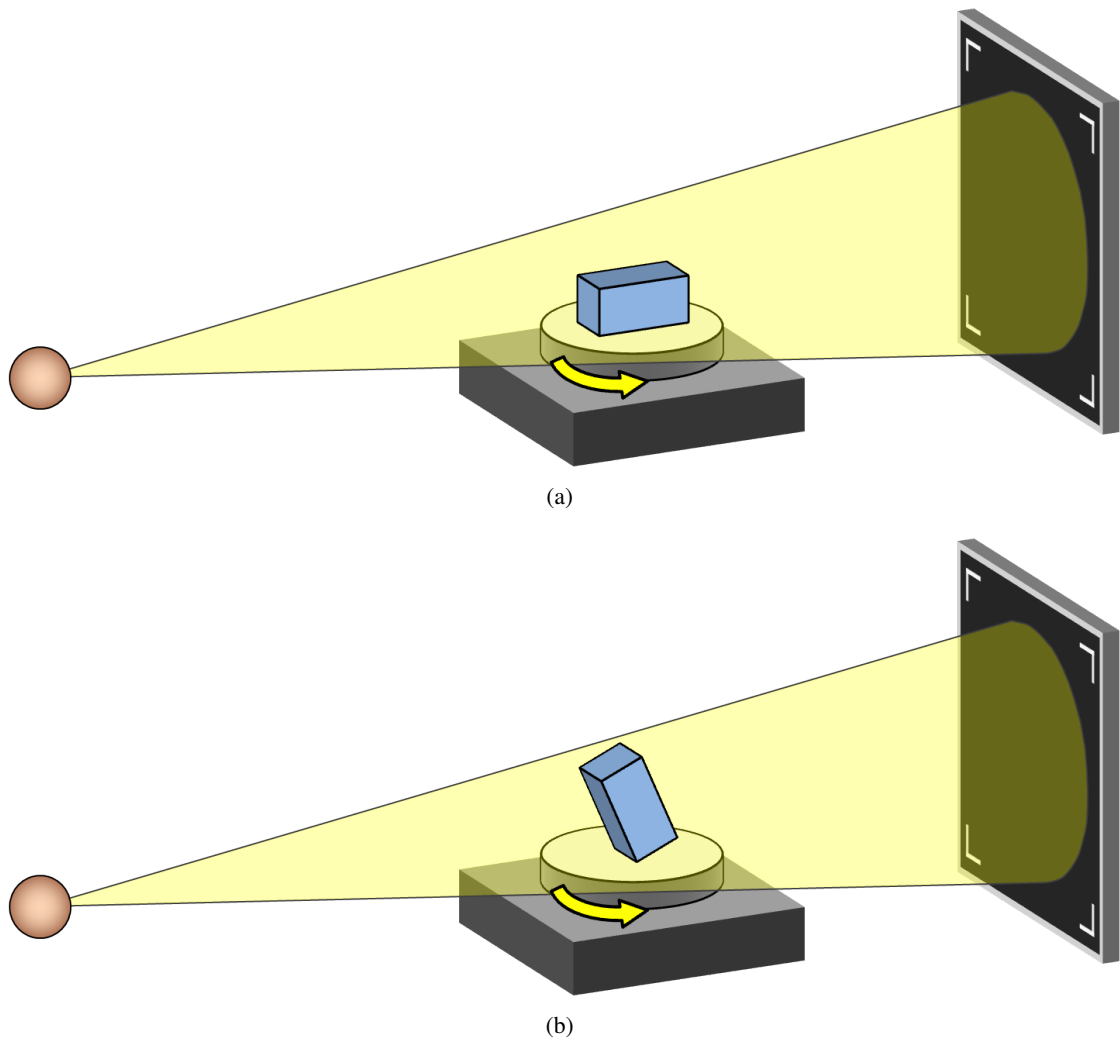


Figure 2.1: Example of a bad and a good placement of a specimen on a rotary plate. Placement (a) has high penetration lengths and top and bottom faces which will produce heavy artifacts. Placement (b) has shorter penetration lengths and good face orientations.

find the optimal placement is not an option due to the long overall machine occupation times and high costs. Another issue is the complexity of comparing the 3DXCT results.

In this situation, the technicians require a visual analysis tool to determine the optimal specimen placement. The proposed tool provides a simulation-based preview and it is able to estimate artifacts and deviations for every placement.

After consultations with industrial 3DXCT domain experts we identified three criteria for what is defined as a good specimen placement. The requirements for a good specimen placement are formulated as follows:

- short cone-beam penetration lengths
- no surface data lost during scanning
- the penetration lengths and lost surface data parameters are stable within a certain range of reliability (usually about 5 degrees of placement orientation)

In the following paragraphs we consider these conditions in greater detail.

The penetration length of a ray is defined as the distance which the ray passes inside the specimen. A large penetration length of an X-ray is prone to cause beam-hardening artifacts and may consequently reduce the accuracy of measurements. Therefore, the penetration length is a very important parameter which we want to minimize in order to decrease deviations and improve measurement accuracy.

When cone-beam scans are used, for some of the planar faces of the specimen an exact reconstruction is not possible due to the incompleteness of the acquisition geometry [74] [83]. For this reason these faces will appear blurred in the resulting reconstructed volume. Corresponding to Tuy-Smith [69] the sufficiency condition for a full reconstruction is the following: if every plane that intersects the object, at some point during the scanning rotation contains the X-ray source point, then one can fully reconstruct the object. For an accurate reconstruction of an arbitrary plane, it should intersect the circular trajectory of the source. Applying this to the faces of the specimen we get the following: a face can be accurately reconstructed if its plane has an intersection with the circular trajectory of the source. The Tuy-Smith data sufficiency condition [69] helps to identify blurred faces. These faces are nearly perpendicular to the rotation axis and have a big height offset from the X-ray source's position. An example of bad faces is given in Figure 2.2. As we can see from this example, we can get rid of the bad faces by choosing a proper placement of a specimen. Minimizing the total surface area of faces, which do not satisfy the Tuy-Smith data sufficiency condition, will result in better scan results.

The above mentioned parameters should remain stable within a certain range of placement variability, as the technicians are able to setup the orientation of a specimen only with a certain precision. Usually it lies within a range of 1-5 degrees. The stability of a placement determines how fast a parameter (e.g., maximum penetration length) changes when the orientation of the placement is modified. Small modifications in the orientation of a specimen may cause strong changes in the considered parameter and therefore in the scanning result. The less the placement's parameter changes with a modification of the orientation, the more stable the placement is. If the parameters of the placement are changing considerably, then the orientation is considered to be inappropriate because of its instability. Thus, the stability of a placement is another decisive factor for choosing an optimal placement.

In quality control of new products manufacturers test representative samples of each production charge for compliance with quality requirements and the presence of defects. Computer-aided design (CAD) models are used as reference. In other cases (e.g., reverse-engineering) a geometrical surface model may be obtained through CT or optical scans. The geometrical surface model of the specimen can therefore be used as input data for the simulation and evaluation of an optimal placement.

In this chapter we present a visual analysis tool that determines optimal placements of a specimen on a rotary plate using the following criteria:

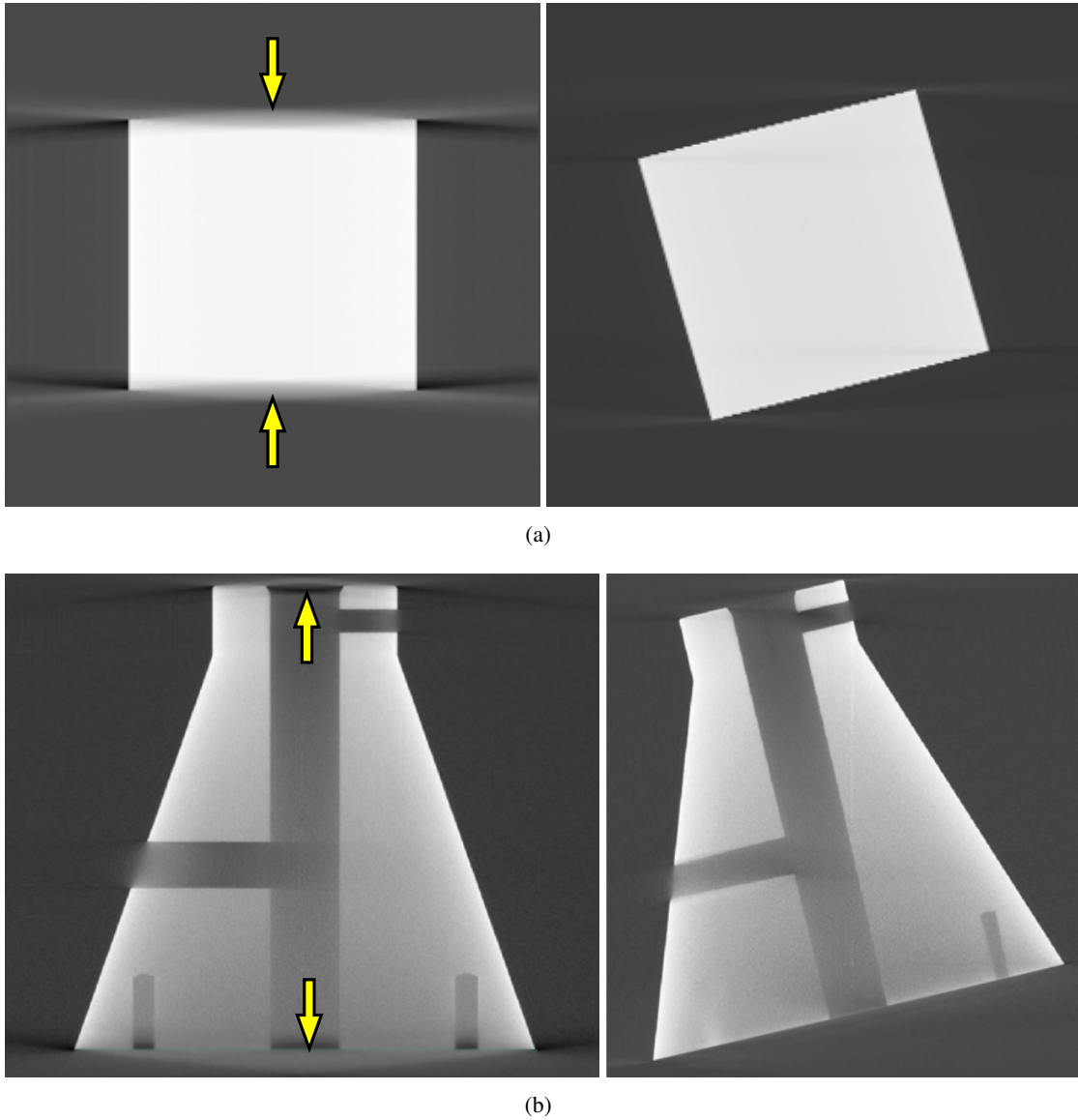


Figure 2.2: Example of bad faces for the cube specimen (a) and for the TP03 specimen (b). Artifacts are marked with yellow arrows. The placements to the left are worse than the placements to the right.

- Short cone-beam penetration lengths: based on a ray casting simulation (section 2.3)
- No surface data lost during scanning: based on a Radon-space analysis (section 2.4)
- The penetration lengths and lost surface data parameters are stable within a certain range of reliability: using a stability widget (section 2.5)

An overview of the workflow of the visual analysis tool is presented in Figure 2.3. Concerning placement, we consider only the orientation of a specimen on the rotary plate. The orientation is defined by two degrees of freedom, as the third degree of freedom corresponds to the rotation of the specimen on the rotary plate. The position of a specimen on the rotary plate is not considered because it would make the computational complexity of the simulation too high. Moreover, the position of the specimen has a small influence on the outcome of the simulation and insignificantly changes the optimal orientation value. The tool allows further visualization, exploration and visual analysis of the obtained data (section 2.6). The main contributions of this work are the application of easy to understand visualization methods for the penetration-length data and the Radon-space analysis data; visual analysis of the parameter variability using a stability widget; ray visualizations and Radon-space analysis.

2.2 Related Work

Multi-image views are used by Malik et al. [44] for a visual exploration and comparison of a dataset series generated by scanning a specimen with different parameters on an industrial CT device. Common CT simulation approaches as Monte-Carlo simulations [29] [42], hybrid approaches [17] [70] and discrete simulations [60] of CT are used to predict the results of real measurements by computing the interaction of virtual X-rays with matter. Such a prediction helps the technicians in measurement technology to minimize artifacts by using optimal measurement parameters. Monte Carlo and related simulation methods are more complex and computationally expensive. We focus on penetration lengths and do not address a detailed simulation of the X-ray attenuation and interaction with matter.

Camera control and viewpoint selection for polygonal and volumetric data are well investigated research areas. Vázquez et al. [75] worked on the problem of defining a ‘good’ view. They use viewpoint entropy to evaluate the quality of a viewpoint. Bordoloi and Shen [10] use viewpoint entropy in volume rendering to determine a minimal set of representative views for a given scene. The importance of single voxels and the similarity between viewpoints are taken into account for their viewpoint-selection process. A feature-driven approach to select a good viewpoint is proposed by Takahashi et al. [71]. They propose to decompose an entire volume into a set of feature components, and then find a globally optimal viewpoint by taking a compromise between locally optimal viewpoints. Viola et al. [77] introduced another automatic viewpoint-selection approach for features in a volume dataset. The focus feature is defined by the user and their system automatically determines the most expressive view on this feature. Mühler et al. [48] presented an approach for viewpoint selection in medical surface visualizations. They describe a viewpoint-selection technique guided by weighted parameters like size of unoccluded surface, importance of occluding objects, preferred region and viewpoint stability. Viewpoint stability is used to avoid viewpoints where the object of interest is occluded by small changes of the camera.

There are various approaches implemented to select a region of interest (ROI) in the inspected object. When a ROI is specified for volume data this region is also called volume of interest (VOI). Tory and Swindells [73] presented ExoVis for detail and context direct volume

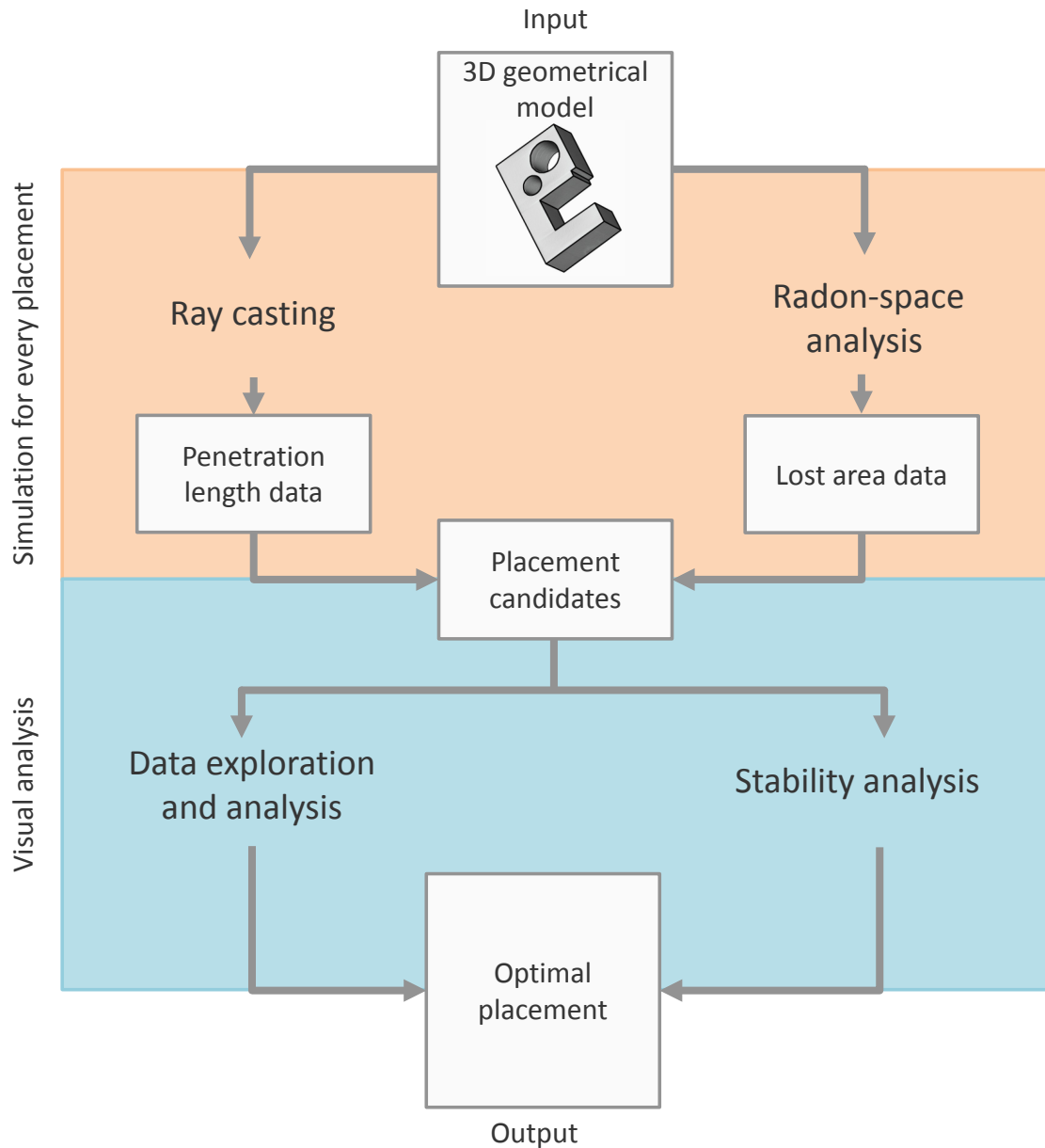


Figure 2.3: Workflow of determining an optimal specimen placement.

rendering. They define a VOI by specifying a box within the volume. Different transfer functions can be used for the picked region. Owada et al. [51] presented a technique to specify a ROI within unsegmented volume data. The user specifies the 2D contour of the interesting structure and the system performs a constrained segmentation based on statistical region merging.

The main purpose of a viewpoint selection is to provide an expressive view of the data. We focus on finding the specimen placement with optimal parameters for the 3DXCT scanning. The placement stability is defined by the behavior of these parameters when the orientation of the specimen is changed.

Missing Radon-space data during CB scanning is a well studied phenomenon. Zhu et al. [83] analyze the CB projections in Radon space and apply implicit interpolation/extrapolation to the missing data in order to reduce beam-hardening artefacts. We are not aware of any existing related work which makes a Radon-space analysis of triangles using the Tuy-Smith data-sufficiency condition.

2.3 Penetration-Length Analysis

Concerning penetration-length analysis there are two important factors which determine the overall optimality of a placement: how long are penetrations and how many rays have high penetration lengths. In this respect, we use two parameters to characterize a placement: the maximum penetration length and the average penetration length. The maximum penetration length is the longest distance that an X-ray beam has to travel inside the specimen. The average penetration length is the average distance which the radiation has to go through the specimen in order to reach the detector.

We employ ray casting to calculate the penetration lengths. Basically we could calculate penetration lengths through rasterization, i.e., surface rendering on the GPU. We have decided to use ray casting, even if it is more costly. The main reason is the flexibility and extendibility which ray casting offers. This concerns the calculation of additional parameters that the simulation might require (e.g., the scattered radiation contribution to the results). Another possible approach is a purely analytical computation of maximum and average penetration lengths. The decisive disadvantage of this approach is the high complexity of the calculations. For instance, in order to calculate the average penetration length of one projection, we need to calculate the volume from the surface mesh and divide it by the surface area of this mesh projected on the detector plane. Computing the maximum penetration length is also a nontrivial task when using a purely analytical approach. On the other hand, ray casting provides a good approximation to the average and maximum penetration lengths.

The ray-casting geometry in our approach reflects the real-world scanning-device setup. The source of the X-ray radiation corresponds to the ray origin. We cast a ray for every X-ray cell on the flat-panel detector and the result is stored in a single pixel. We substitute the specimen with its 3D geometrical model represented by a list of triangles. We further use data about the setup of the scanning device to configure the ray casting geometry.

The simulation is computed for a discrete set of possible placements. Every placement is determined by its orientation. The position of the specimen on the rotary plate is fixed. The orientation is determined by two Euler angles α and β . We obtain the successive placement in a set by changing one of the Euler angles by a certain step-angle. The user-defined number of angle samples and angle range determine the step-angle. For every placement in a set we perform ray casting and calculate the penetration lengths.

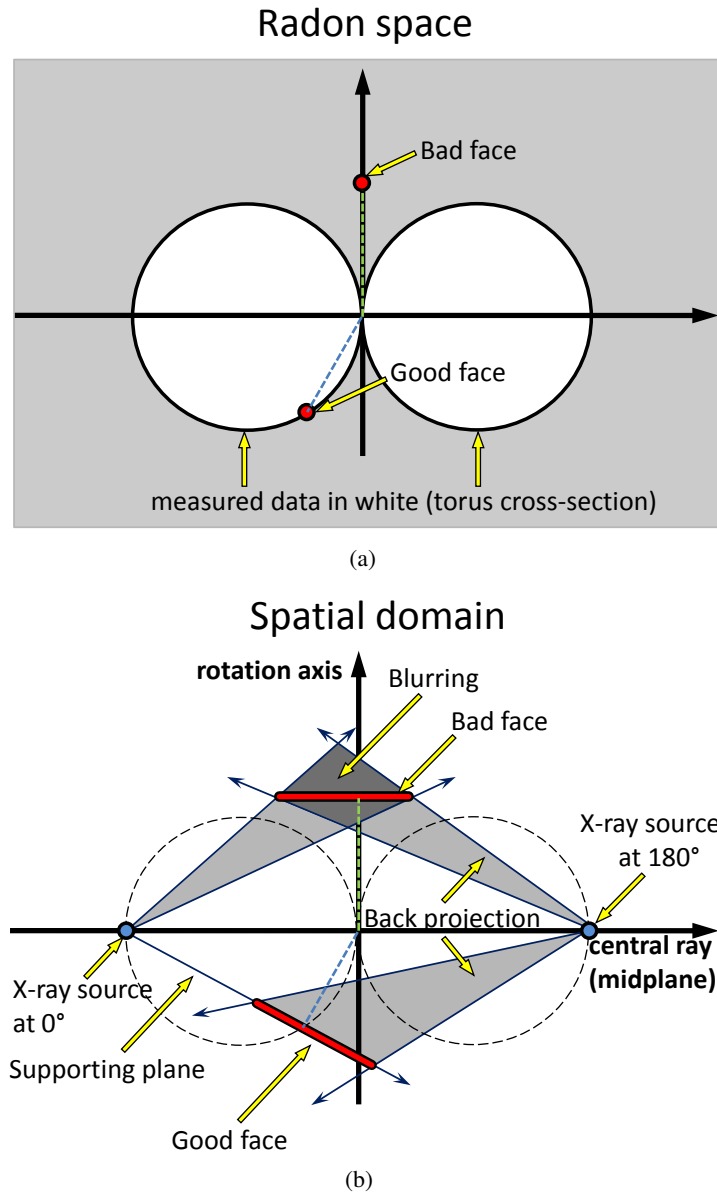


Figure 2.4: Cross-section through Radon space (a) and the spatial domain (b). The two white circles in (a) correspond to a cross-section through the torus that contains data captured during the scan. The rest is the shadow zone. Examples of good and bad faces are given.

The data that we get from the ray casting is represented in three layers: rays, projections, and placements. A placement consists of a sequence of projections. The projections of a placement are obtained rotating the specimen around a vertical rotation axis. Every projection in its turn is obtained by casting a set of rays.

The penetration lengths are calculated for all casted rays of a placement. We calculate the penetration length of a ray as the sum of distances which the ray passes inside the specimen. The average penetration length of a projection is calculated as average of the penetration lengths from the corresponding rays. Finally the average penetration length of a placement is calculated as average of the penetration lengths from the corresponding projections. In addition for every projection and placement the maximum penetration lengths are determined. The maximum penetration length of a projection is the maximum from all the corresponding rays. Finally the maximum penetration length of a placement is the maximum from all corresponding projections.

In order to speed up the ray-casting step we implemented parallelized CPU and GPU (CUDA coded) versions. We use a k -dimensional tree (kd -tree) as a space-partitioning data structure. A stack-based algorithm for traversing the kd -tree is employed.

2.4 Radon-Space Analysis

Cone-beam CT devices using the Feldkamp algorithm (FDK) reconstruction algorithm suffer from a specific kind of artifact: inaccurate reconstruction of some planar faces of the object which are not in the midplane. The midplane is the plane that contains all the points of the source trajectory. For the circular cone-beam scanning this is a plane perpendicular to the rotation axis. This artifact leads to a blurring of the reconstructed volume and, therefore, reduces the measurement accuracy. The presence of artifacts strongly depends on the specimen placement. We want to find the placement which has no bad faces or which has the fewest number of such faces.

2.4.1 Background and Theory

Reconstruction from projections as done in 3DXCT is closely related to the Radon transform. Let a 3D function f be defined on the domain D . The continuous 3D Radon transform maps a function in \mathbb{R}^3 into the set of its plane integrals in \mathbb{R}^3 . The Radon transform \check{f} of function f , which is specified by a vector \vec{n} , is given by:

$$\check{f}(\vec{n}) = \int_{\vec{r} \in P(\vec{n})} f(\vec{r}) d\vec{r} \quad (2.1)$$

where P is a 2D plane, with a normal vector collinear to \vec{n} and a displacement $|\vec{n}|$ from the origin (i.e., the point on the rotation axis located on the same height as the X-ray source). The Radon transform maps every plane in the spatial domain to a point in Radon space. The mapping is done in a way that the position vector of this point has the same direction as a plane's normal. The length of the position vector is equal to the distance from the plane to the origin. This mapping was first studied in detail by Radon [58] in 1917. Radon showed that if \check{f} is continuous then there exists a unique and analytic inverse transform. The 3DXCT scanning samples the Radon transform \check{f} of the object. Reconstruction algorithms as filtered back-projection approximate the inversion.

With circular cone-beam (CB) scanning the cone-beam X-ray source is rotated around the object. The situation where a specimen is rotated on a rotary plate is considered as a circular

scan. The circular CB trajectory only partially satisfies the Tuy-Smith sufficiency condition. For some faces of the scanned object, there are no corresponding points of the circular CB source trajectory which lie on the supporting planes of these faces. This means that it is impossible to completely measure all information about these planes of the scanned object with the Radon transform. Only at the midplane (plane of the source trajectory) an exact reconstruction is possible. For one CB projection, the surface of a sphere is acquired in Radon space. The diameter of the sphere is equal to the distance from the X-ray source to the rotation center. As the rotary plate turns, the sphere rotates as well. With a full scan, a torus is measured in the Radon space (see Figure 2.4). The higher the number of projections, the better the Radon transform is sampled inside the torus. The part of information in Radon space which is not inside the torus forms a shadow zone. If the supporting plane of the face lies in the shadow zone then Tuy-Smith's sufficiency condition does not hold. If the supporting plane of the face is inside the torus in Radon space then Tuy-Smith's sufficiency condition is true for this face. All faces of the specimen that are perpendicular to the rotation axis (except those in the midplane) are in the shadow zone. Furthermore, all the faces whose supporting planes do not intersect the circular trajectory of the source are in the shadow zone as well. Faces of the specimen that lie in a shadow zone will produce back-projection artifacts. These artifacts appear in the direction of the back projection and blur object faces on the scanned projection images. An example of a bad face and a good face is given in Figure 2.4.

2.4.2 Radon-space Analysis

The goal of the Radon-space analysis is to minimize the total surface area of object triangles, whose supporting planes are outside the torus of measured data in Radon space. Therefore we calculate for every placement the Radon-space representation of all triangles of the specimen surface. Every triangle is represented as a point in Radon space. The position vector of this point has the same direction as the triangle's normal and the length is equal to the distance from the supporting plane of the triangle to the origin in the spatial domain. We check whether the point in Radon space is inside the torus of measured data or not. As a result we calculate the total surface area of triangles whose Radon information is not sufficiently captured during the scanning. The placement with the minimal lost surface area is considered to be the optimal one. We use the percentage of the lost surface area as another parameter in our visual analysis system. Triangles that are causing back-projection artifacts are color coded (see section 2.6.4).

The Radon-space investigation determines the areas which cause back-projection artifacts. As the method requires only angles between supporting planes of triangles and the rotation axis, we need to do calculations just once for a placement. We do not need to process the entire sequence of projections (as we have to do in the ray-casting simulation).

2.5 Placement-Stability Analysis

After the penetration-length analysis and the Radon-space analysis, the stability of the determined optimal placements is evaluated. Typically technicians are capable of placing the specimen on the rotary plate with a placement error between 1-5 degrees. This imposes the following limitation on the optimal placement: the results of the penetration-length analysis and the Radon-space analysis should remain stable within this range. In this respect, we require a tool for the visual analysis of the robustness of the placement's parameters in a considered range. The tool should allow a distinction between improvement and deterioration of the parameters along certain directions. Another desirable feature of the tool is the ability to show in which direction parameters vary the most. For this purpose we use a custom stability widget as visualization technique (see Figure 2.5). We pick a parameter and a placement in order to see how the parameter changes when we change the orientation of the specimen. Deviations for the selected parameter (e.g., maximum penetration length) are shown on the stability widget. The central cell on the widget represents the specimen's current placement. Neighboring cells correspond to the placements obtained by stepwise changing one of the two Euler angles. The horizontal axis of the color-coded map corresponds to the α Euler angle and the vertical axis corresponds to the β Euler angle. The deviation of the parameter from the central placement is color-coded. Green colors correspond to better placements and red to worse placements. The maximum deviations obtained by changing only one of the Euler angles, keeping the other Euler angle fixed, are coded as gray values on so called stability arrows. Stability arrows are applied for extracting information about the stability of a placement in a certain direction. For example, dark gray corresponds to a rather instable behavior on that axis, white corresponds to stable conditions.

Considering the stability widget in the example of Figure 2.5, the β direction is more stable than the α direction. If we change the orientation of the specimen along the β axis in the positive or the negative direction the parameter value will gradually improve. The worst case would be changing the α angle in the positive direction. Considering the fact that the parameter changes only gradually in all directions, this placement is robust and stable.

The main purposes of the stability widget are to visually explore the robustness of the placements, and the visual analysis and immediate recognition of patterns. However, a fully automated stability analysis could be implemented. For example, it is possible to automatically reject the placements with great instability. In this work we focus on the visual exploration and analysis of placements where an automatic categorization is not easily possible.

2.6 Data Visualization, Exploration and Visual Analysis

2.6.1 Visualization of Placement Parameters.

The parameters of every placement in a set are represented using color-coded maps and 3D plots. The 3D plot representation is used for a better visual representation of the data. The color-coded map depiction is used for navigation and user interactions. Every pixel of the color-coded map or vertex of the 3D plot is colored according to the value of a placement parameter. The horizontal axis of the color-coded map corresponds to the α Euler angle and the vertical axis corresponds to the β Euler angle. The user gets numerical labels of the parameters of a placement and its

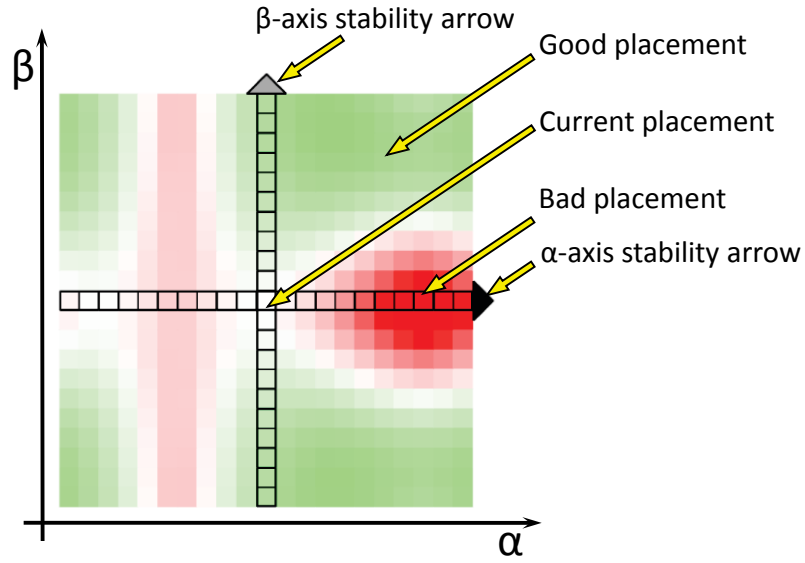


Figure 2.5: Widget representing the stability of the specimen's placement.

orientation by clicking in the color-coded map. The 3D view of the specimen is automatically updated so that the specimen is placed using the orientation of the picked placement. In addition the user can select through a slider a certain percentage of the placements with the best parameter values on the color-map. The discarded placements will be displayed in black.

2.6.2 Comparatative Visualisation of Placement Parameters

To visualize the different parameters we use linked views in a side-by-side visualization (see Figure 2.6). There is one map for every parameter. When the user is picking a placement in one map the others are updated as well, so that the picked placement is highlighted in all maps.

2.6.3 Feature Selection

In many cases technicians are interested in accurate scan results for certain critical features or areas of interest in the specimen. In this case they need a tool to select critical features (e.g., drill holes) and to calculate placements which are appropriate for these features only. We allow the user to select certain features of the specimen. We do the selection by specifying a set of axis-aligned bounding boxes (AABB) around the features of interest (see Figure 2.7). The user can add new boxes, select boxes by picking them in a list and delete boxes from the list. The extent of a box is changed using sliders. After the set of the bounding boxes is specified, all parameters are evaluated just for these boxes. Only rays that intersect one of the specified bounding boxes are processed during the ray-casting process. Only triangles which are fully inside one of the bounding boxes are used in the Radon-space investigation.

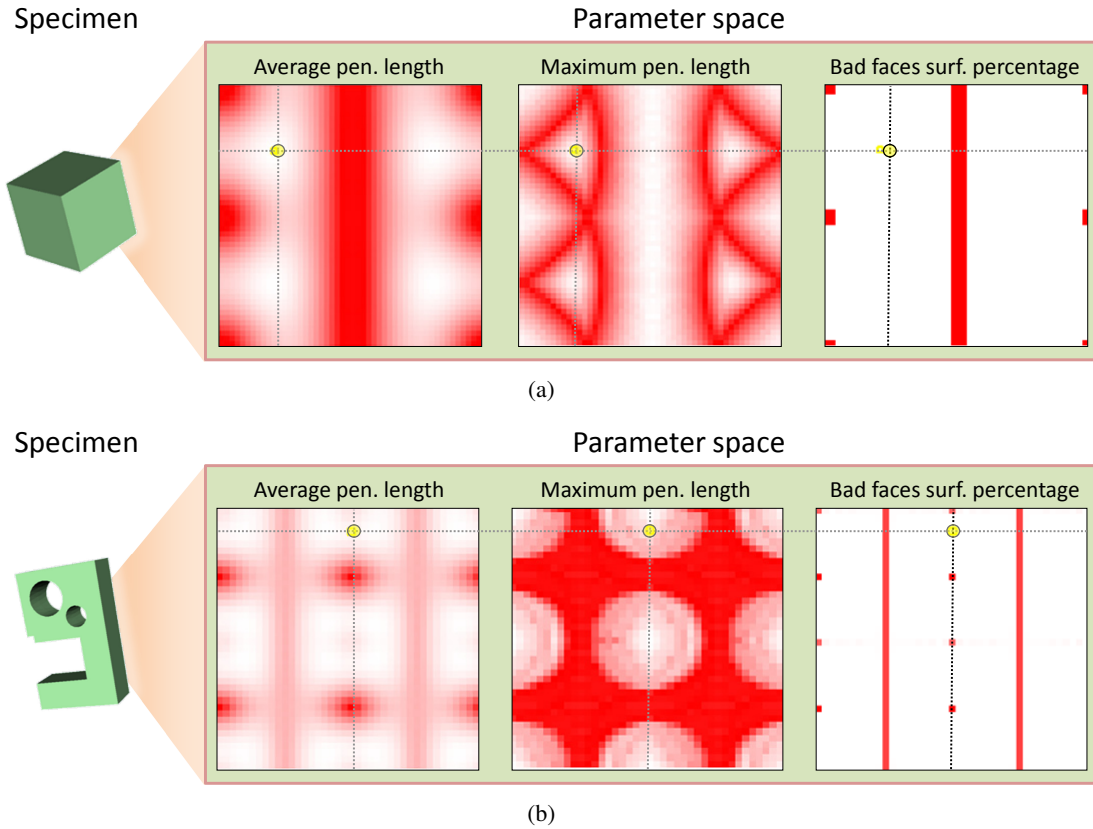


Figure 2.6: Linked views used for the comparative visualization of the cube specimen (a) and of the TP09 specimen (b). A good placement is highlighted.

2.6.4 Color-Coding Bad Areas

In order to visualize the results of the Radon-space investigation we color code the triangles which are outside of the torus of measured data in the Radon space. Color coding of bad surface areas on the 3D geometrical model of a regular aluminium test part (Kasperl [32]) is shown in Figure 2.8. This surface model was extracted by reengineering the corresponding 3DXCT dataset. We can clearly see the artifacts on this model: the artifacts between the two drill holes, the vertical stripes on the sides and the distorted top of the specimen.

2.6.5 Penetration-Length Histograms

Another helpful component is building histograms of the rays' penetration-length distributions (see Figure 2.9). To build a histogram the user specifies the placement he is interested in and picks the desired parameter. Such histograms are useful when we need to see how many rays have penetration lengths in a critical range. Histograms also allow to see how uniformly the rays

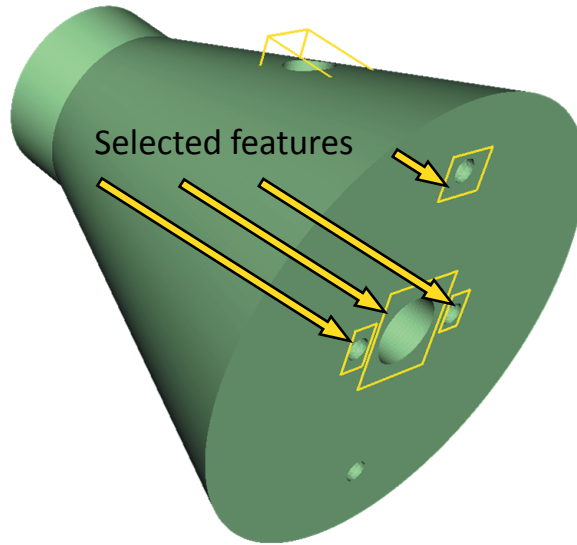


Figure 2.7: Selected features represented in the 3D view of the specimen's geometrical model.

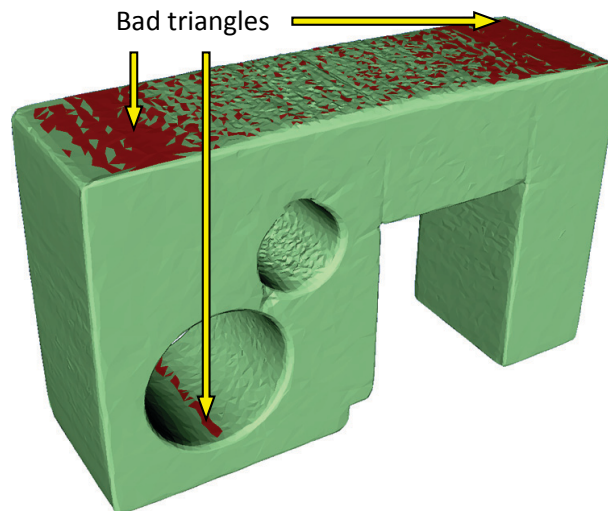


Figure 2.8: Color coding the results of the Radon-space investigation on the surface model of test part TP09. Triangles shown in red are outside the torus of the measured Radon data.

are distributed for the picked parameter. For example, if only a few of the rays have high penetration lengths or most of the penetration lengths are in some narrow range, then the placement can be considered as being good. On the other hand, if most of the rays have high penetration lengths or the range of the penetration lengths is large then the placement should not be used in the 3DXCT scanning. In addition, the user can build a histogram for a single projection of a placement.

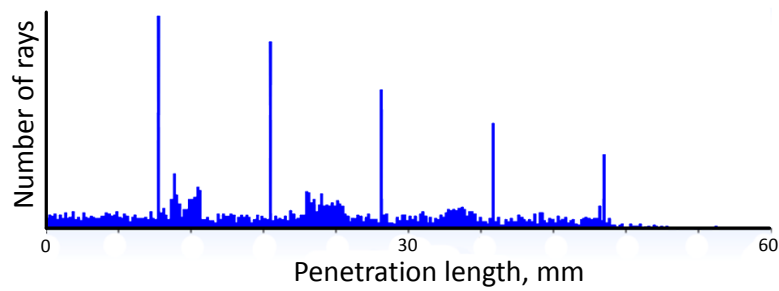


Figure 2.9: Example of penetration-length histogram.

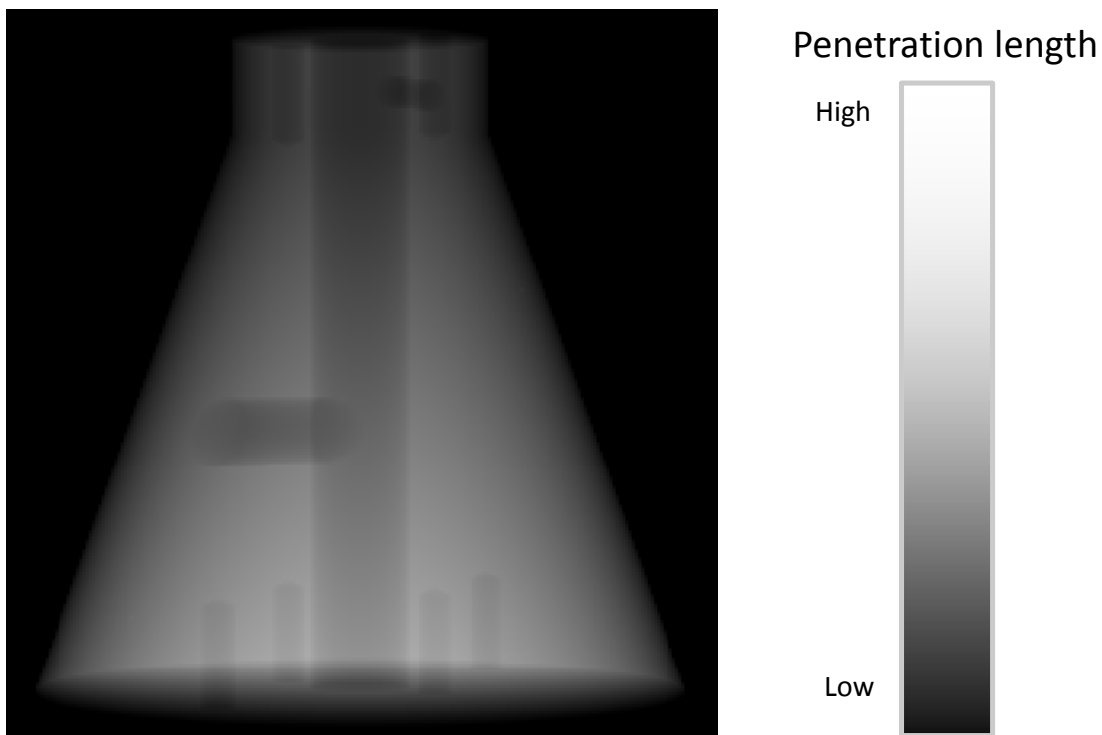


Figure 2.10: Visualizing the penetration lengths of a single projection in grayscale.

2.6.6 Visualization of Ray Subsets

Often the penetration-length histograms do not show all the information required to make a proper decision. In this case a visualization of the penetration lengths of a single projection is helpful. We show the direct output of the ray-casting simulation using grayscale images (see Figure 2.10). The greater the penetration lengths of rays are, the brighter are the corresponding pixels.

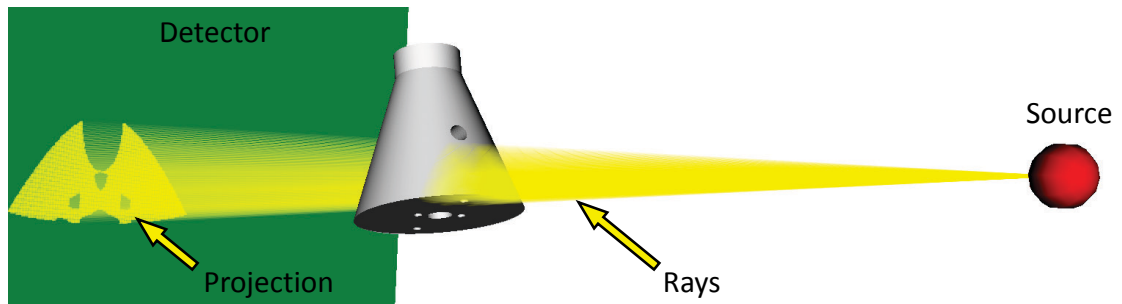


Figure 2.11: Visualizing rays with penetration length in a specified range. Rays are drawn as semi-transparent yellow lines. The green plane represents the detector. The red sphere is the X-ray source.

In order to determine problematic areas we visualize rays within a certain range of penetration lengths. The user specifies the projection and the penetration lengths he is interested in. The rays with corresponding penetration lengths are visualized using semi-transparent lines. The corresponding detector points are highlighted with point sprites (see Figure 2.11). This visualization represents geometrical information about areas of the specimen with high penetration lengths and shows the corresponding regions on the detector or resulting image.

2.7 Implementation and Performance

The prototype application was implemented in Visual C++. The interactive 3D view was implemented using VTK [64]. The GPU ray-casting implementation was coded using CUDA [49]. The GUI of the developed tool is shown in Figure 2.12.

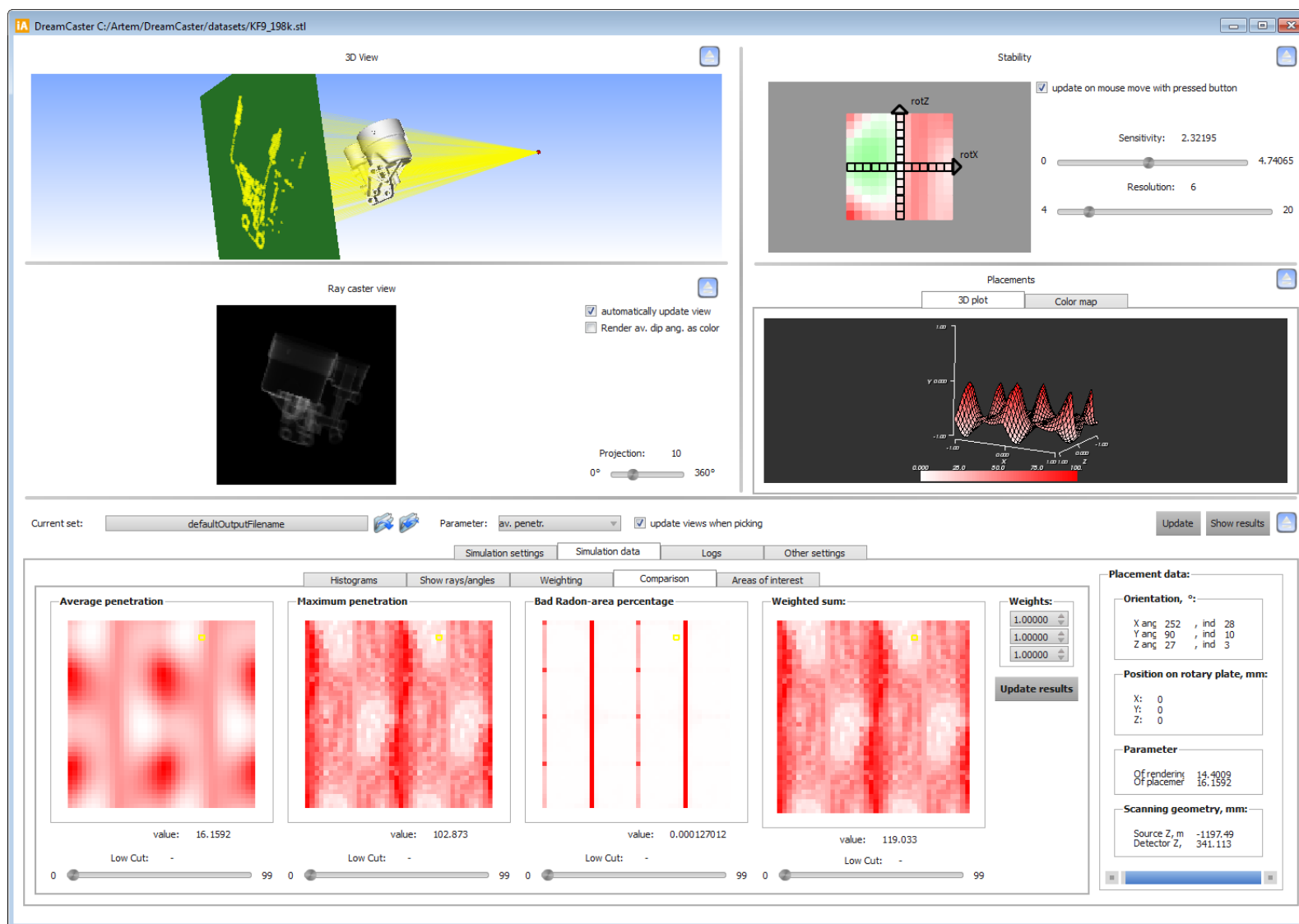


Figure 2.12: GUI of the tool for detecting optimal specimen placement.

2.7.1 Parallelization

The set of placements of the specimen that we need to process is known in advance. Calculations for rays are also independent from each other. Thus, there are two possible ways of parallelization: parallelization on the level of the projections and parallelization on the level of the rays.

In the CPU implementation the screen is split into tiles. Every tile is processed by a separate thread. The assignment of the threads to the processor's cores is done by the operating system. The GPU architecture on the other hand is highly parallel and can execute thousands of threads. Every ray is processed in a single thread.

If the resolution of a projection image is lower than the maximum number of threads that the GPU can handle, not all of the GPU capabilities are used. In the GPU implementation we therefore process several projections in one pass. Several projections are treated as a single image. For instance, the set of n projections with resolution $x \times x$ will be rendered as an image with a resolution of $x \times x \times n$ pixels. Rays corresponding to different projections have origin and direction vectors according to the projection's rotation angle. This strategy is called batch rendering as we process a batch of the projections in one call of the kernel function. Batch rendering uses most of the GPU capabilities because the number of threads processed with a single call of the kernel function increases.

2.7.2 Performance

Ray casting is a crucial part in the entire system performance. So, in this section we will concentrate only on the performance of the ray-casting step. The most important parameters for the GPU performance are the resolution and the complexity of the specimen's geometrical model. Table 2.1 shows a performance comparison of the CPU and GPU implementations. The GPU performance depends on the resolution, number of triangles in the model, and batch size. The GPU implementation is 1.1 to 6 times faster than the CPU implementation. The GPU implementation shows good results on small geometrical models and high resolutions. On the other hand, if the geometrical model is big, threads are computationally complex and have many conditional branches in the kd -tree traversing algorithm. The GPU implementation does not provide any significant improvement compared to the CPU implementation in this case.

Our implementation is relatively slow compared with existing GPU ray tracers (e.g., work by Popov et al. [54]). There are two main factors that influence the performance of our implementation. First, in our implementation we cannot use early ray termination as we need to find every ray-specimen intersection. Second, we have to do data streaming from the GPU memory back to the CPU memory in order to store the simulation results.

2.8 Results

2.8.1 Evaluation

The general workflow of using the system is as follows. First, the user selects the features of interest on the geometrical model. Then the system calculates the penetration-lengths data and

Triangles	Projection resolution	Projections	CPU time, s	GPU time, s		
				Batch size		
				10	30	50
12	256×256	1000	16.864	3.963	3.042	2.761
310	256×256	1000	18.127	7.411	6.271	6.037
25880	256×256	1000	27.612	25.038	23.749	23.400
25880	1024×1024	100	39.562	16.676	-	-
200000	256×256	1000	78.281	43.446	42.229	41.871

Table 2.1: Comparison of the CPU and GPU ray-casting times in seconds on the various triangulated models. CPU: Intel Core i7, 920 @ 2.67 GHz. GPU: NVIDIA GeForce GTX 260.

Feature	Sigma value, mm				
	0	10	45	70	90
A	0,040	0,041	0,079	0,110	0,134
B	0,015	0,013	0,023	0,167	0,102
C	0,014	0,013	0,020	0,030	0,132
D	0,019	0,006	0,013	0,013	0,017
E	0,032	0,037	0,063	0,086	0,137
F	0,084	0,038	0,068	0,080	0,021
G	0,172	0,064	0,010	0,023	0,022
H	0,080	0,044	0,025	0,023	0,041
I	0,066	0,038	0,026	0,033	0,215

Table 2.2: Sigma values of the features in the CT measurements for the TP03 specimen.

does the Radon-space investigation for the set of placements. Based on the obtained data, the system proposes a set of candidates for the optimal placement. Afterwards the user determines the optimal placement using the visual-analysis functionality provided by the tool. The user should pick a placement with the minimal maximum-penetration length and the shortest possible average penetration length. There should be only small surface areas affected by the Tuy-Smith data-insufficiency condition in Radon-space. Furthermore the above mentioned criteria should remain stable within the possible positioning accuracy of 1-5 degrees. This means that the picked placement should be stable. Finally, the user applies the determined placement for the specimen positioning on the rotary plate.

For the evaluation of the presented method a set of scans with different specimen placements was measured. A fixed set of measurement features for every placement is evaluated using the commercial CT metrology software ‘Calypso’ from Carl Zeiss IMT Corporation Germany. Calypso is a standard tool in the area of coordinate measuring machines and multidimensional

Feature	Average penetr. len., mm					Maximum penetr. len., mm				
	0	10	45	70	90	0	10	45	70	90
A	53	53	54	60	60	95	97	102	119	119
B	25	25	29	46	40	38	40	73	119	105
C	25	25	29	46	40	38	40	73	119	105
D	24	24	36	52	54	37	39	77	119	115
E	50	50	58	65	62	74	74	102	117	108
F	67	58	35	34	41	95	96	77	76	72
G	66	70	66	60	40	95	95	102	110	72
H	76	75	58	57	52	95	97	93	92	100
I	76	75	58	57	53	95	97	94	92	100

Table 2.3: Average and maximum penetration lengths of the TP03 specimen's features.

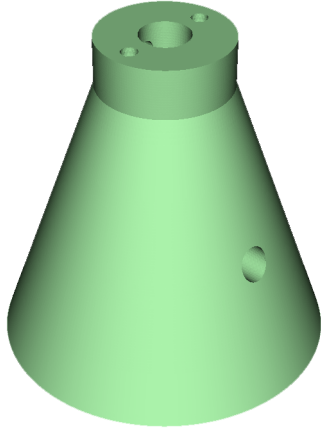
Feature	Sigma value, mm									
	0	10	20	30	40	50	60	70	80	90
O-C2	0,002	0,002	0,004	0,006	0,007	0,009	0,007	0,009	0,012	0,008
O-C3	0,002	0,003	0,005	0,006	0,006	0,008	0,007	0,008	0,008	0,008
O-C4	0,002	0,005	0,004	0,006	0,006	0,007	0,006	0,006	0,005	0,013
I-C1	0,004	0,004	0,005	0,005	0,006	0,011	0,006	0,017	0,018	0,019
I-C2	0,005	0,005	0,006	0,006	0,007	-	0,011	0,015	0,017	0,010
I-C3	0,009	0,008	0,009	0,010	-	-	0,014	0,012	0,013	0,011
I-C4	0,012	0,012	0,013	0,013	-	0,012	0,011	0,010	0,010	0,011

Table 2.4: Sigma values of the features in the CT measurements for the TP07 specimen. The features are named as follows: 'O' stands for the outer diameter, 'I' stands for the inner diameter, 'C' stands for the step-cylinders from top to bottom.

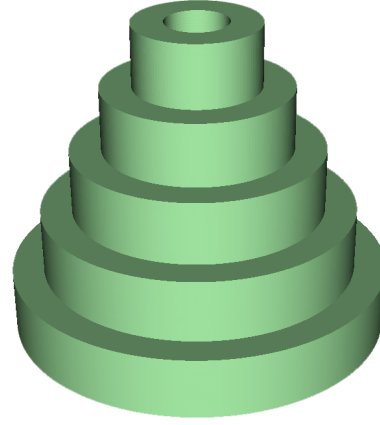
metrology. For every measurement feature (e.g., length, diameter, roundness, evenness etc.) this tool interpolates a predefined number of points along the corresponding geometric primitive (e.g., line, circle, cylinder, plane, etc.) in order to extract the dimension of interest. Instead of extracting the exact dimensions themselves, we calculate the sigma value for every feature measurement as this represents the underlying data quality. Sigma is thereby the standard deviation of the measurement points along the geometry of the primitive. A smaller sigma indicates a better scan and measurement quality. Using our tool we provide the average and the maximum penetration lengths and the percentage of the lost surface area for all of the selected features. To evaluate the simulation results, we compare the sigma values with results provided by our tool. We use two specimen for the evaluation. These specimen are shown in Figure 2.13. In the case of the TP03 specimen the scans were done for placements with α equal to 0, 10, 45, 70 and 90 degrees. As we can see from the comparison of the results, there is a significant correspondence

Feature	Average penetration length, mm											Maximum penetration length, mm										
	0	10	20	30	40	50	60	70	80	90	0	10	20	30	40	50	60	70	80	90		
C1	22	23	24	26	30	37	46	51	52	54	41	46	52	66	95	124	124	124	124	125		
C2	40	42	44	47	53	58	61	63	64	65	55	68	82	101	114	124	124	124	124	125		
C3	56	58	61	64	66	67	67	67	67	67	76	89	106	114	114	124	124	124	124	125		
C4	79	77	77	75	73	71	70	69	68	68	107	111	114	114	115	124	124	124	124	125		
C5	72	72	65	61	58	56	55	54	53	53	118	119	119	119	119	124	124	124	124	125		

Table 2.5: Average and maximum penetration lengths of the TP07 specimen's features. The features are named as follows: 'C' stands for the step-cylinders from top to bottom.



(a)



(b)

Figure 2.13: The specimens used for the evaluation: TP03, a cone with attached cylinder, a large central drillhole and several minor drillholes (a); a TP07 step-cylinder with a central drill hole (b).

between the percentage of the lost surface area and the accuracy of linear distance measurements. The penetration-length simulation predicts good placements for the drill-hole radius measurements. Tables 2.2 and 2.3 show the sigma values of the features in the CT measurements and penetration lengths of these features for all α values of the TP03 specimen. The optimal placement for every feature is given in bold font. We can see that the placement proposed according to the average penetration length is coincident with the optimal placement for features A, B, C, D and E. The average penetration length predicts optimal placements for 5 features out of 9. Maximum penetration length correctly proposes optimal placements for the features A, E, F, H and placements with sigma within the maximum error range (0,01 mm) for the features B, C and I. The maximum penetration length predicts 7 features out of 9. The G feature is not predicted

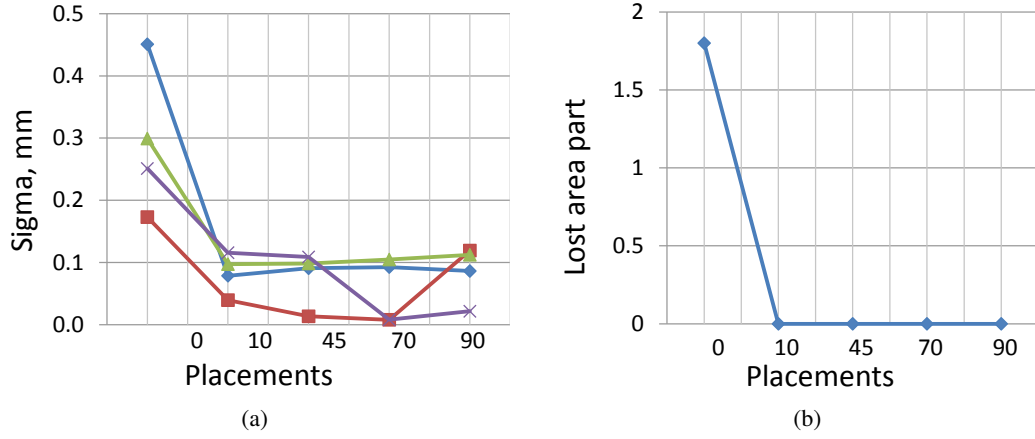


Figure 2.14: The plots of the sigma values of the linear distance features (a) and the percentage of the lost surface area (b) for the TP03 specimen.

by any of the parameters. The maximum penetration length correctly predicts more placements than the average penetration length, however, the D feature is correctly predicted only by the average penetration length.

The plots of the sigma values for the distance measurements and the percentage of the lost surface area for the TP03 specimen are given in Figure 2.14. We see that the placement with an α value of 0 degree has the highest lost surface percentage and the highest sigma values. We also compared the bad surface areas obtained by the Radon-space investigation with the reconstruction images (see Figure 2.15). We can see that there is a strong correspondence between the results of the Radon-space investigation and the real world data.

As second specimen, to evaluate the proposed method with, test part TP07 is used, a step-cylinder with a central drillhole. Different α values of the specimen have been analysed. The placements corresponding to α equal to 0, 10, 20, 30, 40, 50, 60, 70, 80 and 90 degrees were used. Diameters and heights of every cylinder step were measured. We use the percentage of the lost surface area to evaluate the heights (linear distance measurements), and penetration lengths to evaluate the drill-hole radius measurements. Tables 2.4 and 2.5 show sigma values of the features in the CT measurements, and penetration lengths of these features for every placement of the TP07 specimen. The placements proposed by the average penetration length are coincident with the optimal placement for features O-C2, O-C3, I-C1 and I-C2. The proposed placement is nearly optimal for the feature I-C4. The average penetration length predicts 5 features out of 7. The maximum penetration length proposes optimal placements for the features O-C2, O-C3, O-C4, I-C1 and I-C2. The proposed placement is nearly optimal for the feature I-C3. The maximum penetration length thus predicts 6 features out of 7. The same as in the previous case, the maximum penetration length correctly predicts more placements than the average penetration length. However, the I-C4 feature is better predicted by the average penetration length.

The sigma values of the linear distance features and the percentage of the lost surface area for the step-cylinder are given in Figure 2.16. An α of 0 degree has the highest lost surface

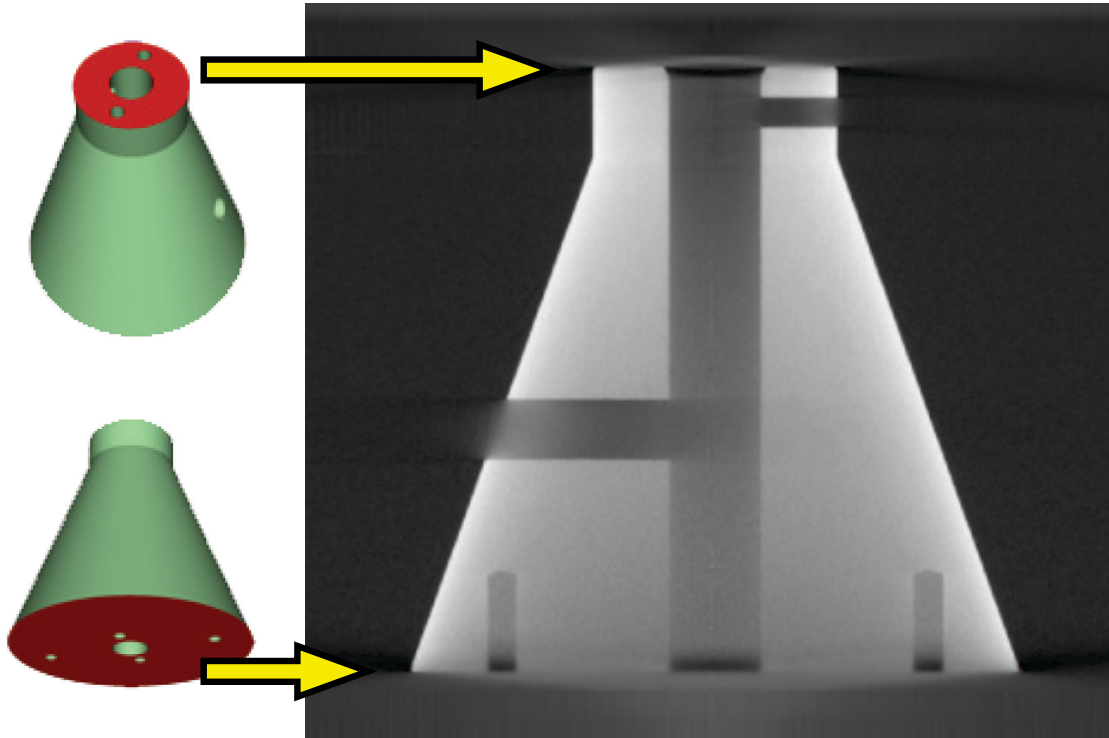


Figure 2.15: Comparison of the bad surface areas obtained by the Radon-space investigation with the reconstruction images for the TP03 test specimen. Surface areas causing back projection artifacts are outside of the torus of measured Radon data and shown in red.

percentage and high sigma values. The high sigma values at 50 degree cannot be explained by the simulation data and are considered to be outliers due to irregularities in the measurement. An unstable positioning of the specimen could be a reason for high sigma values at this placement. For example, if the specimen is slightly tilted during the scanning, this results in blurring and low measurement accuracy. As the neighboring placements have lower sigma values we assume that this placement is an outlier.

The optimal placements for most of the features of both test specimens are predicted by the average and the maximum penetration lengths. For both test specimens the maximum penetration length predicts more optimal placements than the average penetration length. The evaluation shows that prediction can be improved by combining these two parameters. To solve this task the penetration-length distribution of the placement might be used.

Additionally we perform a variance comparison for the specimen shown in Figure 2.17a. For this evaluation we do the following. First, using our tool we have suggest one optimal (good) and one suboptimal (bad) placements. Then we have perform two real 3DXCT scans using suggested placements. Subsequently, we extract surface models from the resulting 3D volumes. Finally, we perform evaluate deviations of obtained surface models from the reference

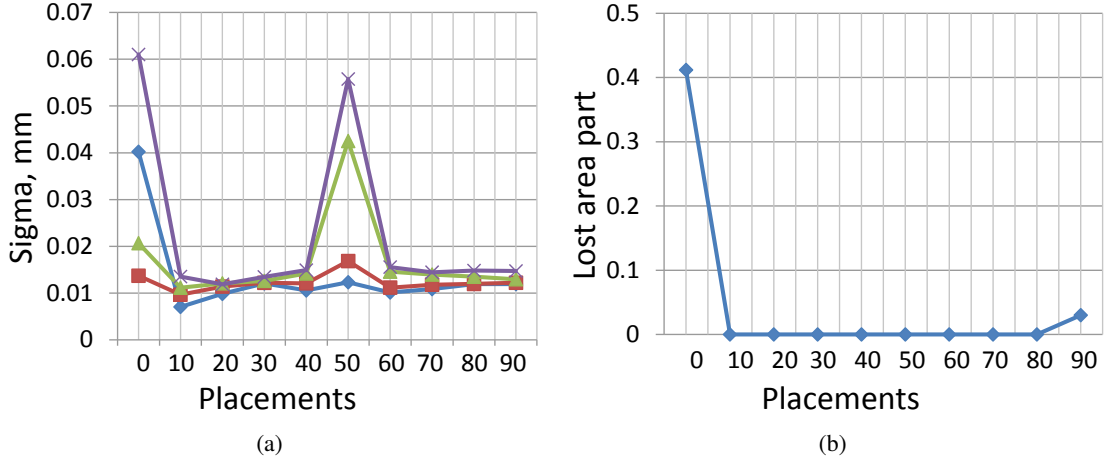


Figure 2.16: The plots of the sigma values of the linear distance features (a) and the percentage of the lost surface area (b) for the TP07 step-cylinder specimen.

CAD model. We show results for the bad placement (Figure 2.17b) and the good placement (see Figure 2.17c). The deviations are color coded on the CAD model. Green corresponds to low deviations, dark red corresponds to strong positive deviations, and dark blue corresponds to strong negative deviations. Gray areas depict regions where no surface was present for the comparison. The optimal (good) placement of the specimen has a better overall distribution of deviations and in several areas shows significantly lower deviations than the suboptimal (bad) placement.

2.9 Conclusion

We have presented a tool for a visual optimality and stability analysis of 3DXCT scan placements. We use a novel 3DXCT simulation approach including penetration-length calculation, Radon-space analysis and placement-stability analysis using a stability widget. The tool can be used for determining the optimal specimen placement based on a given geometrical model. Additionally, the tool enables the domain experts to study the correspondence of the penetration lengths and the Radon-space representation of the specimen concerning artifacts and measurement accuracy. We use programmable GPUs and task parallelization to achieve a better performance. The applicability of the obtained results has been discussed using two real-world specimens.

Our approach has several limitations. One disadvantage is that we do not consider the position of the specimen on the rotary plate. Picking a good position will also affect the outcome. Adding the position of the specimen to the simulation strongly increases the computation time and complicates the visualization and the analysis of the results. In our future work we intend to determine the optimal orientation and the optimal position in sequence. Another limitation of our approach is that it requires a certain amount of user interactions. Our system cannot

propose the optimal placement fully automatically based on the collected parameters. Furthermore, in our future work we intend to develop a parameter that combines average penetration length, maximum penetration length and percentage of lost surface area. This should increase the accuracy of determining optimal placements.



(a) Specimen

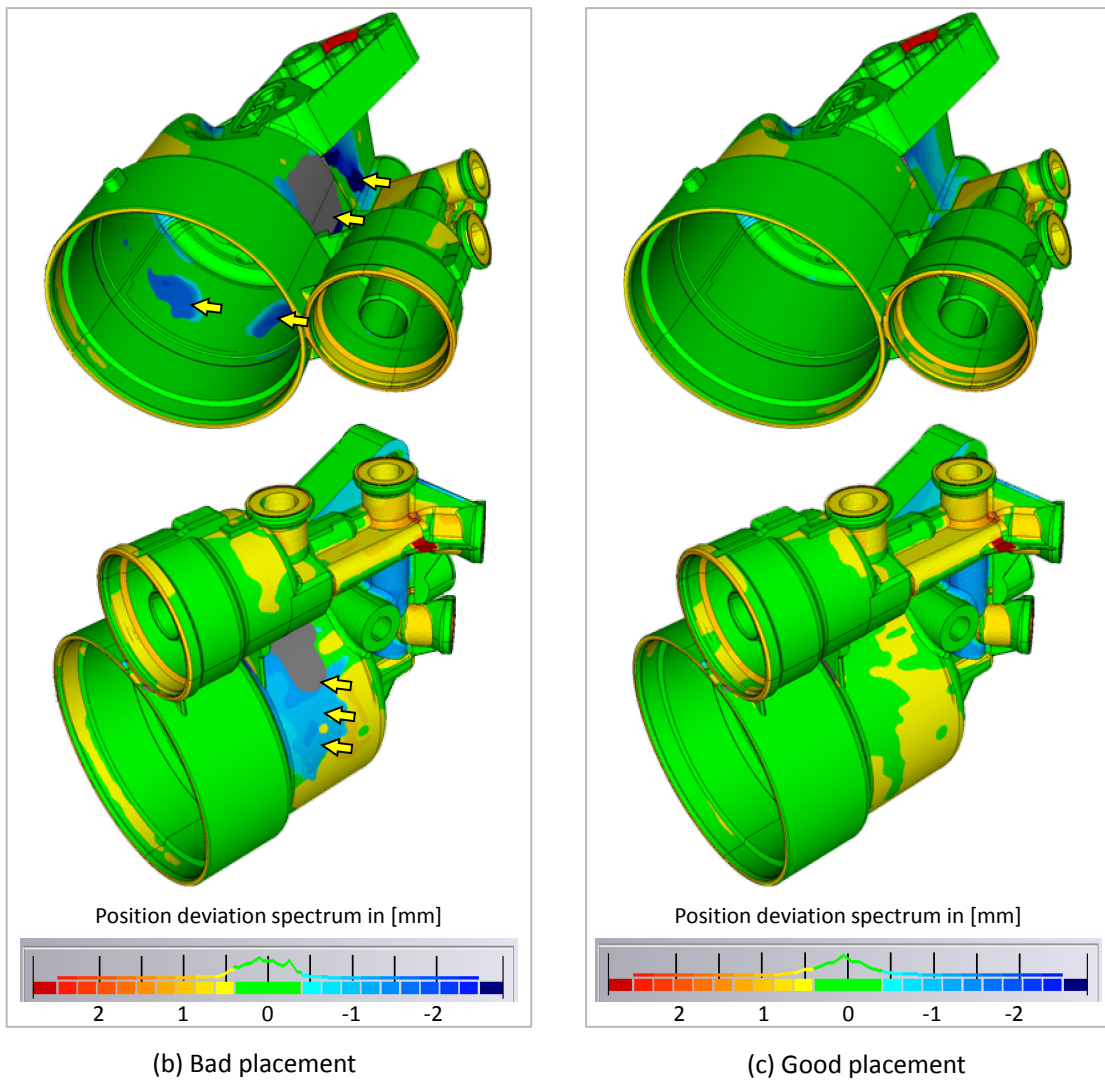


Figure 2.17: Surface deviation evaluation. The specimen (a) and the corresponding color coded surface deviation for a bad (b) and a good (c) placements. Areas where deviations are decreased using a better placement are marked with arrows.

Projection-Based Metal-Artifact Reduction for 3DXCT

Multi-material components, which contain metal parts surrounded by plastic materials, are highly interesting for inspection using industrial 3D X-ray computed tomography (3DXCT). Examples of this application scenario are connectors or housings with metal inlays in the electronic or automotive industry. A major problem of this type of components is the presence of metal, which causes streaking artifacts and distorts the surrounding media in the reconstructed volume. Streaking artifacts and dark-band artifacts around metal components significantly influence the material characterization (especially for the plastic components). In specific cases these artifacts even prevent a further analysis. Due to the nature and the different characteristics of artifacts, the development of an efficient artifact-reduction technique in reconstruction-space is rather complicated. In this chapter we address a projection-space pipeline for metal-artifacts reduction. The proposed technique first segments the metal in the spatial domain of the reconstructed volume in order to separate it from the other materials. Then metal parts are forward-projected on the set of projections in a way that metal-projection regions are treated as voids. Subsequently the voids, which are left by the removed metal, are interpolated in the 2D projections. Finally, the metal is inserted back into the reconstructed 3D volume during the fusion stage. We present a visual analysis tool, allowing for interactive parameter estimation of the metal segmentation. The results of the proposed artifact-reduction technique are demonstrated on a test part as well as on real-world components (see Figure 3.1). For these specimens we achieve a significant reduction of metal artifacts, allowing an enhanced material characterization [2] [3].

3.1 Introduction

3DXCT highly convenient for the inspection of *multi-material components* (MMCs). However the high density range of materials used in MMCs often results in streaking artifacts. They appear when the low-absorbing material of a specimen contains metal inclusions such as pins,

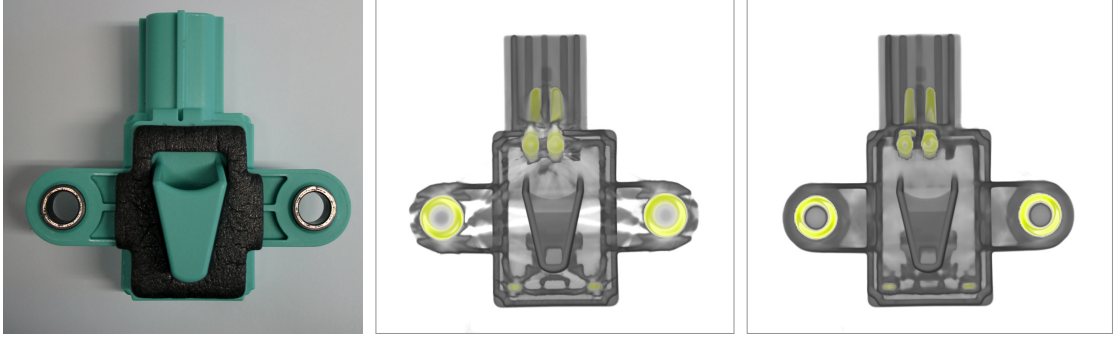


Figure 3.1: The plug specimen photo (left) and volume renderings before (center) and after (right) metal-artifact reduction.

screws or nails. Streaking artifacts are most common when MMCs containing metal are investigated using 3DXCT and are often called *metal artifacts*. Metal artifacts appear as massive bright or dark bands between the highly absorbing components. They also appear as high frequency streak-noise originating at the boundary of metal inclusions. An example of metal artifacts causing distortions of the media between the metal pins and high frequency streak noise is given in Figure 3.2. Due to these artifacts material characterization and dimensional measurement is hindered and in several cases is not possible.

The problem of metal artifacts in MMCs is of high importance and prevalent in industrial *X-ray computed tomography* (XCT). MMCs are very common as most modern industrial parts have multi-material components, at least after assembly. There is a big variety of materials and the range of attenuation coefficients is in many cases very high as compared to medical XCT. Using high energies in industrial XCT scanning typically introduces blurring of low-absorbing materials and, therefore, does not allow one to efficiently capture high-frequency details.

In this chapter we adopt a projection-based workflow for *metal-artifacts reduction* (MAR) for industrial XCT. We apply this pipeline to MMCs containing three materials: air, plastic and metal. The motivation behind this workflow is as follows: metal artifacts result from those areas in the projections where metal is represented. So, if we find the areas representing metal and substitute the data with some reasonable approximations, we will be able to reduce artifacts in the resulting reconstructed volume. Since the metal parts are removed we will get an artifact-reduced dataset but still without the metal components. Subsequently, we then insert metal data back into the resulting volume dataset. An overview of the metal-artifact reduction-workflow is presented in Figure 3.3. The detailed description of the workflow is given in Section 3.3.

The given workflow is semi-automatic. Most of the steps (e.g., reconstruction, forward-projection and interpolation) can be done automatically. On the other hand, the material separation requires setting an attenuation threshold by the user.

We present a visual tool integrating all steps of the workflow. It provides the user with a setup-wizard like interface, guiding him through the steps and allowing the specification of all necessary parameters (see Figure 3.4). User goes through every step by selecting corresponding

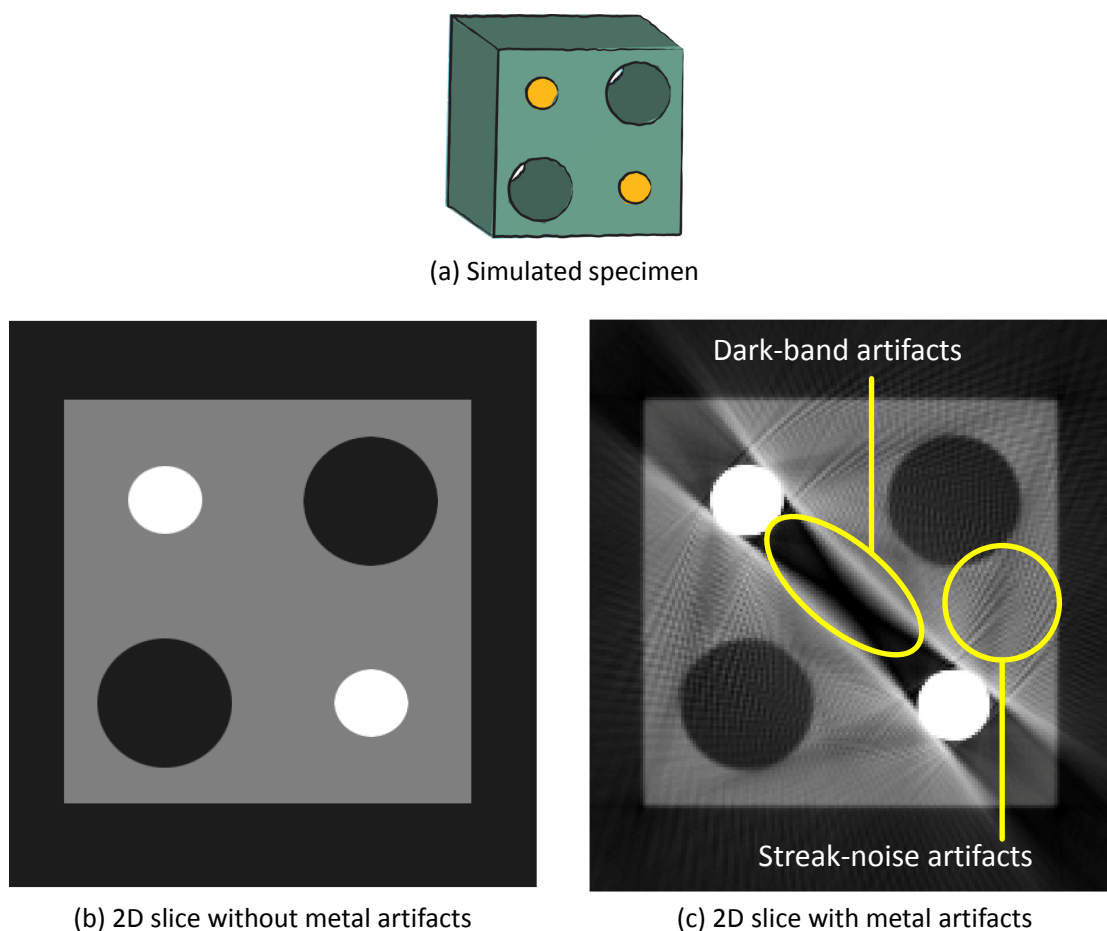


Figure 3.2: Example of metal artifacts using the simulated specimen (plastic cube with metal pins). Dark-band and streak-noise artifacts are marked.

button on the left side of the window. And all user interactions happen in the working area on the right. After all the parameters are estimated, the workflow is executed for the specified datasets and the result of MAR is shown to the user. Comparative visualisation is provided to compare the volume before and after MAR, and explore the introduced differences. The parameter specification is guided using a set of visual analysis techniques. They allow to estimate the impact of the parameters on the MAR result and provide various visualizations for decision support. Basic concepts and the visual analysis functionality of the tool are described in Section 3.4.

The main contributions of this chapter are:

- Adaptation of a projection-based MAR workflow for 3DXCT (and in particular for industrial 3DXCT)

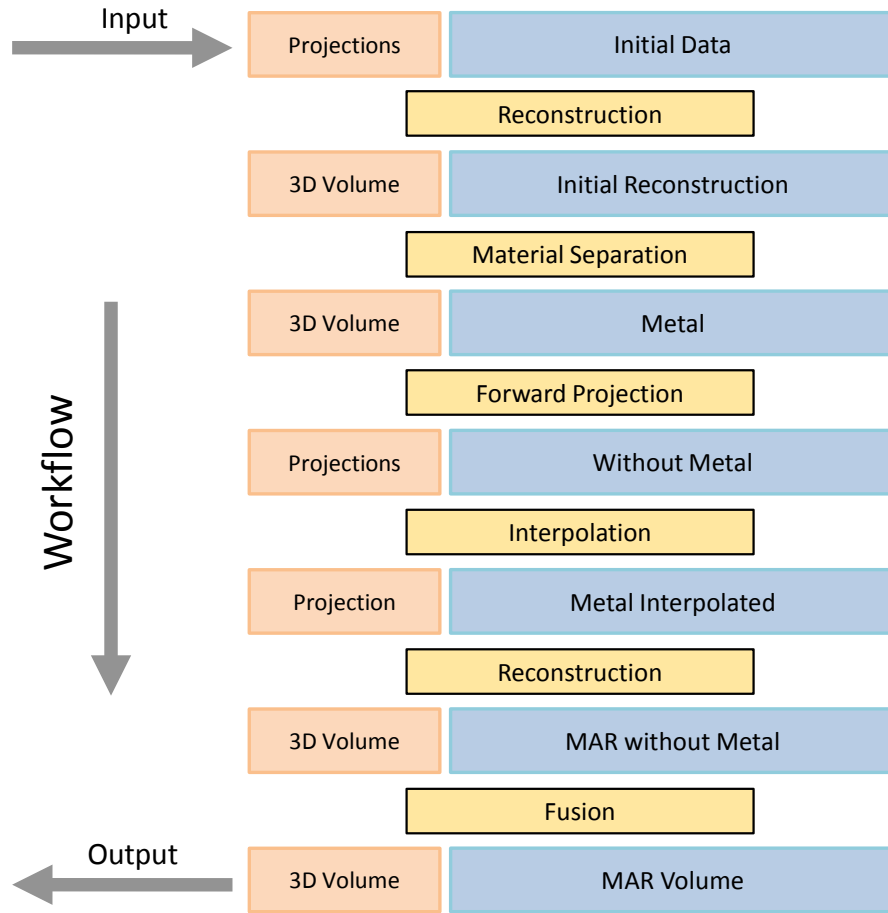


Figure 3.3: Projection-based metal-artifact reduction workflow.

- Integration of the workflow within one tool. It visually guides the user through the workflow pipeline and provides the visual-analysis functionality for an interactive visual parameter estimation.

3.2 Related Work

The problem of beam hardening in general and metal artifacts in particular is important and prevalent for both medical and industrial computed tomography. There are several groups of approaches which deal with this problem.

The reduction of metal artifacts *in the spatial domain* of the reconstructed volume is a highly challenging task. Due to the physical causes of metal artifacts, there is no explicit criterion which would allow the detection of the most artifact-affected areas in order to perform the necessary corrections. One possibility is to use *dual-energy approaches*. Two scans of the MMC specimen are done with different energies. The low-energy scan achieves a better resolution due

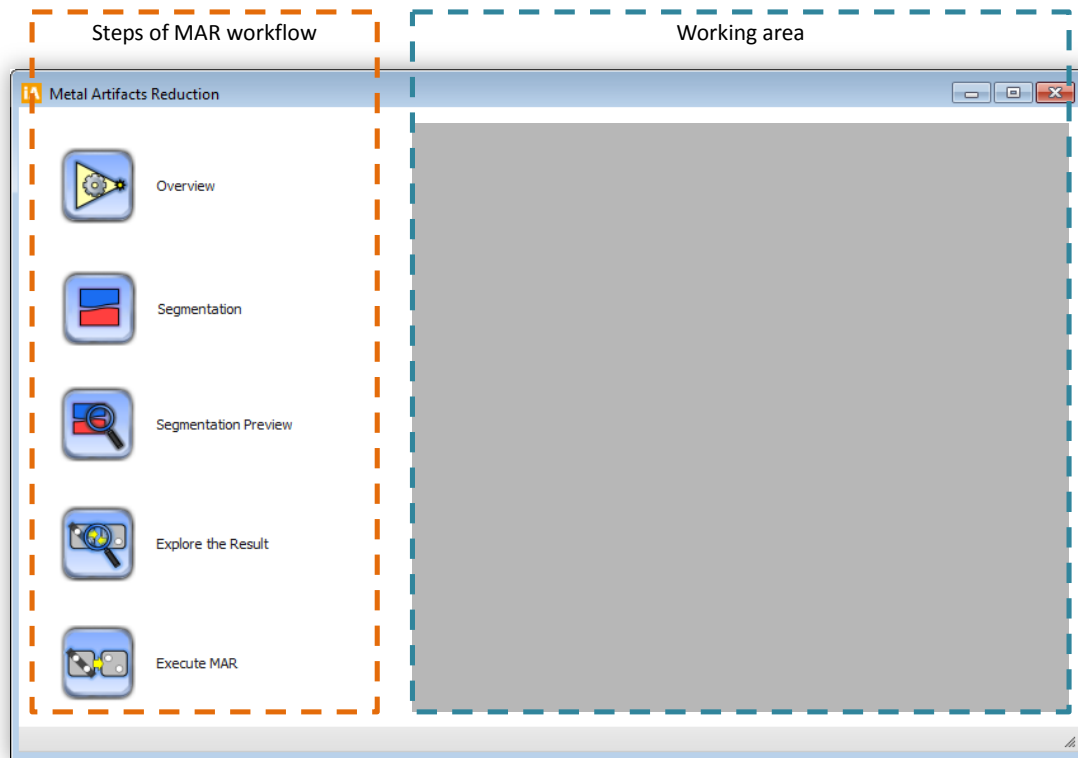


Figure 3.4: Tool's GUI.

to a smaller focal spot of the X-ray source, capturing more high-frequency details but strongly suffering from the metal artifacts. The high-energy scan on the other hand is far less affected by metal artifacts but has a lower resolution due to a bigger focal spot size. By fusing two volumes obtained from the low-energy and high-energy scan one can get a better representation which has both a good resolution and less metal artifacts. Heinzl et al. [22] propose a custom multi-scan fusion scheme which locally fuses the complete datasets of scans using different energies. Additionally there are dual-energy CT (DECT) approaches which calculate the real density and the effective atomic number out of the greyvalues of both datasets [59].

Another way to deal with metal artifacts is to use *projection-based techniques*. In this case metal artifacts are reduced by improving 2D projection images obtained directly from the scanning device. Projections are processed in a way to reduce metal artifacts in the resulting 3D volume. The reconstruction algorithm is then applied to the corrected projections resulting in a 3D volume with reduced metal artifacts. Various metal-artifact reduction techniques using the projection (raw) data are deployed in the area of industrial 3DXCT.

For *single material components* there are several methods to compensate for artifacts applying a linearization technique for the greyvalues. The Iterative Artifact Reduction (IAR) method

by Kasperl [32] is an iterative multistage process. The IAR is based on the linearization technique of Herman [24]. It applies a nonlinear characteristic correction curve on the projection data. The curve is extracted from the volume at every step of the reconstruction. In each iteration the curve is enhanced and the artifacts in the dataset are reduced. Hopkins et al. [25] introduced a related method. The corrections are based on the calculation of the attenuation and scattering processes characteristic of an object composed of a single material. The beam-hardening corrections are applied directly to the projection data prior to reconstruction. The corrections are derived using object geometry extracted from the initial reconstruction. The main disadvantage of the IAR method is based on the assumption that the specimen consists of one specific material or material mixture. MAR methods for single material objects are not suitable in the case when MMCs are used. Nevertheless a big portion of industrial components are MMCs, at least after assembly. In this application area of industrial 3DXCT the most severe artifacts are introduced. This prevents reliable dimensional measurements and material exploration (e.g., determining the porosity of the plastic). Currently, to avoid artifacts due to MMCs, a disassembly into single material components and subsequent separate scans are carried out. This requires the modification and in many cases the destruction of the scanned object. Furthermore, scanning time and memory consumption are increased proportionally to the number of materials in the MMC.

A *multi-material correction* method by Krumm et al. [37] expands the IAR method for MMCs. Materials are segmented in the reconstructed CT image. Then mono-energetic and poly-energetic reprojections are calculated using ray casting. The difference between both re-projections is used as the amount of correction for the initial projections. The whole correction process is iterative. One important limitation of the iterative MAR methods is a high computational cost which results in long processing times. In many cases such a performance is not suitable for 3DXCT where high-resolution 3D data are used. Xue et al. [81] do metal segmentation through a custom region growing directly in the sinogram of the 2D DECT data. However, segmentation in the sinogram does not depend on the actual material density and works well only for a limited list of cases.

Several approaches are used in *medical CT* for removing artifacts caused by metal implants such as tooth implants and dental fillings, prosthetic devices, surgical clips and electrodes. The artifacts arising in the medical 3DXCT images affect diagnosis and treatment planning and therefore seriously limit the clinical value of the XCT scan. One of the first works on metal artifact reduction in medical 3DXCT was by Kalender et al. [31]. It proposed the segmentation of the metal implant in the reconstructed 2D slice image. A semi-automatic segmentation is considered. First the operator approximately delineates the metal, then an exact determination of the metal boundaries is done. Forward projection is used to find the metal areas in the projections. Subsequently linear interpolation is used to substitute the data in those regions where metal projects to. Finally, a filtered back-projection creates an image with reduced artifacts. Subsequent work by Yu et al. [82] does the metal segmentation directly in the projections. Veldkamp et al. [76] applies a complex segmentation strategy in projection space. Three interpolation methods are investigated. Only subtle differences between interpolation methods were found. Oehler and Buzug [50] find a directional interpolation scheme following the flow of the projection data to be superior to linear and polynomial interpolation methods. Additionally, an iterative reconstruction algorithm is used for better artifact reduction. Different methods are used in order to

reduce metal artifacts through image inpainting instead of interpolation. Duan et al. [15] achieve a good approximation using TV-inpainting [66]. Other image inpainting techniques can be used as well for this purpose [12, 65]. Again, high computational costs and memory requirements of image inpainting algorithms make them less applicable to large 3DXCT data.

In the area of medical XCT, metal implants by themselves are of lower clinical interest as opposed to the surrounding tissues. We are not aware of any works which apply similar metal-artifact reductions in medical cases if metal parts are of interest (e.g., dental fillings, projectiles etc.). In the presented works metal parts are excluded from the final scan image or are only approximately denoted. On the contrary, in industrial 3DXCT metal parts of the MMCs are of high interest as they have to be explored and measured along with other materials. The workflow presented in this chapter allows the insertion of the metal parts back into the volume with reduced artifacts. In this way the resulting volume contains all the materials of the MMC specimen which makes it possible to explore the metal parts and their interface with other materials.

All mentioned related work in medical 3DXCT works with 2D slice images but not 3D volumes. In this work we propose a technique which is capable of reducing metal artifacts for 3D volumes resulting from a 3DXCT scan. This imposes certain restrictions on the performance of every individual step of the workflow but allows processing the MAR for the dataset on the order of several minutes. At the end of the related work section we mention works from adjacent research areas which are closely related to the presented method.

Common *simulation* approaches such as Monte-Carlo simulations [29, 42], hybrid approaches [17, 70] and discrete simulations [60] of XCT are used to predict the results of real measurements by computing the interaction of virtual X-rays with a digital model. Fast 3DXCT reconstruction using the GPU is used in order to achieve an improved performance compared to the CPU [79]. Using modern graphics hardware Xu and Mueller achieve real-time 3DXCT reconstruction [80].

Visualization of industrial 3DXCT data is an important area of scientific visualization. Hadwiger et al. [19] explore volume data for detection and classification of features such as pores based on certain parameters (e.g., size, time, density). Huang et al. [27] explore various visualization techniques for nondestructive testing applications.

3.3 Projection-Based Metal-Artifact Reduction

As input data, our pipeline uses 2D projections of the specimen obtained from the scanning device. A 3D volume is generated from the projection images using the filtered back-projection algorithm by Feldkamp et al. [16] (Section 3.3.1). In the material separation stage, the metal is segmented in the reconstructed volume and separated from the other materials (Section 3.3.2). In this stage we find the voxels which contain the metal. The resulting intermediate volume dataset consists only of metal parts. Next, we map the metal-containing voxels from the reconstructed volume to the initial set of projection images using forward-projection (Section 3.3.3). The areas of metal are blanked out. The next step of the workflow is the interpolation of the voids left by the metal components in the set of 2D projections (Section 3.3.4). As a result of this stage we have a set of projections containing plastic and voids filled with the interpolated data. Then, the reconstruction algorithm is applied to the set of projections containing plastic and interpolated data. This produces a 3D volume with plastic which is almost free from metal artifacts. Finally,

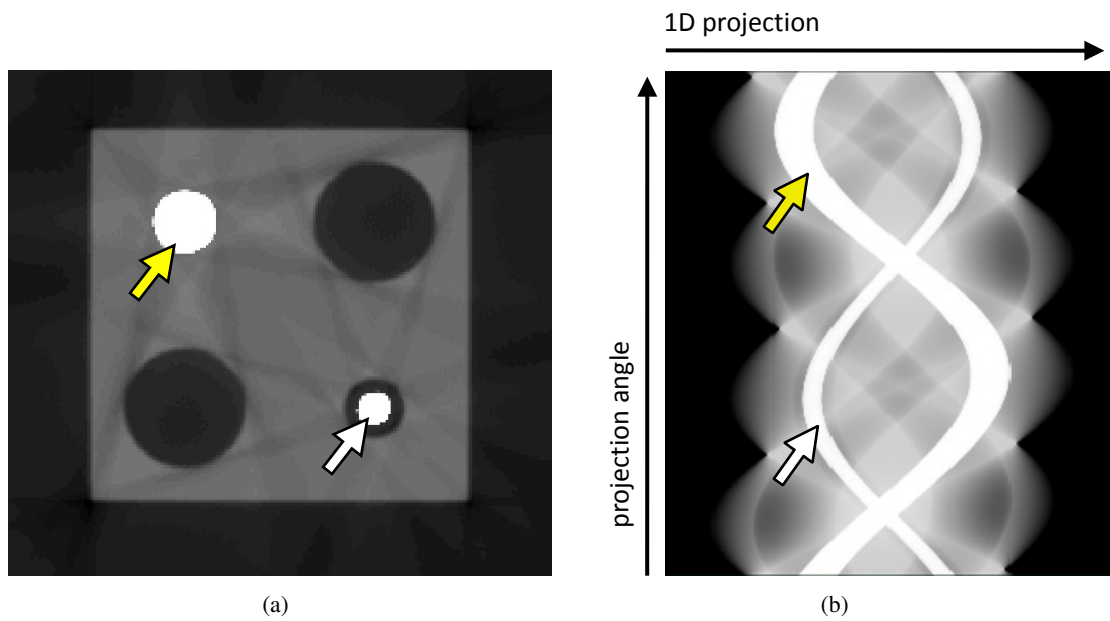


Figure 3.5: Example of a 2D sinogram: a scanned object (here in 2D) (a); a sinogram of 720 1D projections of this image (b). The arrows in (a) indicate the cross-section of two metal pins (bright white areas). The arrows in (b) indicate the trajectories of the metal pin projections (bright white sinusoidal tracks).

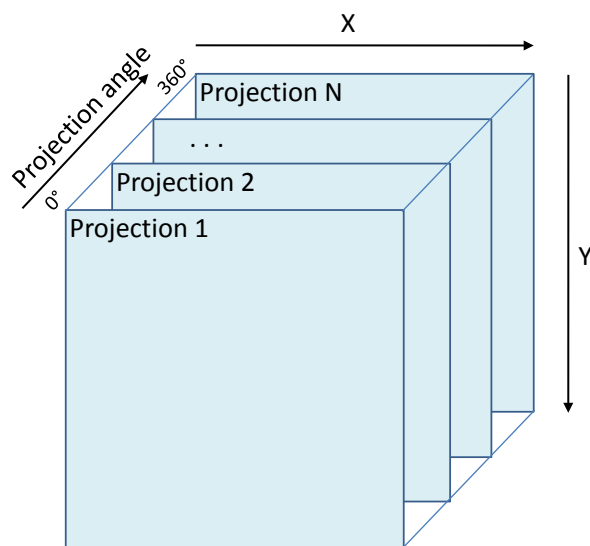


Figure 3.6: 3D sinogram data representation.

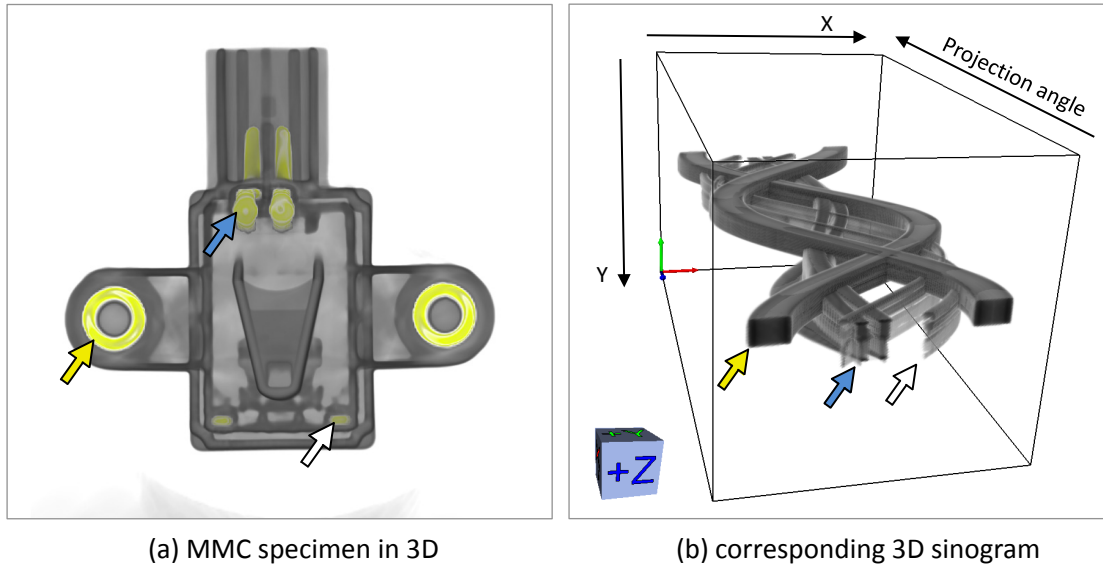


Figure 3.7: MMC (a) and 3D sinogram with trajectories of the metal parts of the specimen (b).

data fusion is done in order to combine the two intermediate volumes: the volume containing only metal parts and the volume containing metal-artifacts free plastic (Section 3.3.5). The metal is inserted back into the volume reconstructed from the interpolated projections during the fusion stage.

Our workflow processes 2D projection images. The projection images are obtained either from scanning or from a corresponding simulation. Every projection is stored in a 2D image. It represents the attenuated X-rays which are partially absorbed by the scanned specimen and recorded by the detector. The projection direction is given by a projection angle. A complete set of projection images is obtained by rotating the specimen stepwise on a rotary plate. This corresponds to a 360° stepwise variation of the projection direction around the specimen. In 2DXCT, the projection data is often represented as a sinogram. This is simply the 2D array of data containing the complete set of ordered 1D projections obtained using line scanners. In this way the projection angle is treated as the second dimension in the sinogram, besides the detector pixels of the line scanner. The resulting sinogram representation reflects inter-projection connections. For example, all projections of a point in the spatial domain will appear as a sinusoid in the sinogram. An example of a 2D sinogram of 1D projections is given in Figure 3.5. For 3DXCT we treat the set of 2D projections as a 3D sinogram, which is a 3D volume containing the stack of all 2D projections (see Figure 3.6). An example of a 3D sinogram is given in Figure 3.7. In Figure 3.6a the specimen is shown in the spatial domain and in Figure 3.6b the 3D sinogram is depicted. Three corresponding metal elements are marked with colored arrows. The areas where no metal is projected to are removed from the sinogram for illustration purposes.

The vertical amplitude of the trajectory in sinogram is zero if the point has no offset from the X-ray source along the rotation axis and increases with a greater offset. Due to the vertical

component of the trajectory, the decomposition of a 3D sinogram into a set of 2D sinograms representing data slices perpendicular to the rotation axis is not possible for cone-beam CT. This is in contrast to parallel-beam CT. With a cone-beam CT only the mid-plane can be represented as a 2D sinogram. All steps of the workflow that operate on projection images use 3D sinogram data representation.

In order to get the final artifact-reduced 3D volume, the user has to go through all the steps of the workflow. Every step takes either a set of 2D projection images or a 3D volume as input and likewise produces such data as output. The user is visually guided through the workflow. It is possible to go back to previous steps of the workflow in order to change parameters and then proceed with the new result.

3.3.1 Reconstruction

We apply filtered back projection to reconstruct a 3D volume from the set of 2D projections. The filtered back projection by Feldkamp et al. (FDK) [16] is the reconstruction method which is widely used for cone-beam 3DXCT. The algorithm consists of two steps. First, a high-pass filter is applied to the projection images in order to eliminate blurring. The most commonly used high-pass filters are the ramp filter and the Shepp-Logan filter [67]. We use Shepp-Logan filtering in the reconstruction algorithm. Second, back projection is used to reconstruct the volume from the set of projection images. The basic idea of back projection is to sweep the projection images back through the 3D volume, accumulating intensity values at the voxels in 3D space. The back projection using unfiltered projection images would produce severely blurred images. The blurring effect appears because the frequency spectra of the projection images overlap in the low frequency regions. Therefore, the prior high-pass filtering step is essential for reconstruction. The FDK reconstruction is comparatively fast and accurate which makes it most suitable for 3DXCT. However, it introduces some additional high-frequency noise to the volume due to the high-pass pre-filtering. It also emphasizes metal streaking-artifacts when MMC specimens are reconstructed. As the FDK reconstruction performs an independent set of computations for every voxel, it is well suited for a GPU-based execution. In this work we use a filtered back projection implemented using the CUDA Toolkit [49]. The performance of the reconstruction benefits from the massive parallelization and computational power provided by the GPU.

3.3.2 Material Separation

A reliable material separation is crucial for the final metal-artifact reduction. The segmentation of the metal components should include all the metal-affected areas of the projections. Furthermore, the segmentation should be accurate in order to avoid segmenting plastic or air parts where there is no presence of metal. MMCs containing small or thin metallic features (e.g., wires, thin pins, metal contacts or rivets) are the most difficult cases for material separation. It is not easy to distinguish such metal features from areas with thicker layers of plastic. Two material-separation approaches can be applied for the segmentation. The first approach is to perform the segmentation by directly operating on the set of 2D projections. Another approach is to compute the segmentation in the reconstructed 3D volume and then to perform a mapping of the resulting segmentation back to the 2D projections. Projection-based segmentation seems

to be a better choice since the additional forward-projection step is not needed, but it has some major drawbacks. It is impossible to segment small metal elements as they produce the same attenuation of the X-rays as thick plastic components. Due to this, it is hard to properly segment the pixels partially affected by the metal. We have encountered these problems during an attempt to develop an efficient projection-based segmentation technique. We have overcome the problem of segmenting partial-volume pixels by using a region-growing algorithm based on an initial segmentation. This gives a proper metal-artifact reduction on the simulated dataset with large metal pins. However this technique has failed on the real-world dataset with small metal elements. Therefore in this work we use the 3D volume segmentation with a subsequent forward-projection step.

We segment metal using straightforward attenuation-coefficient thresholding in the reconstructed 3D volume. The threshold should be selected in a way to segment as much metal as possible, without touching any other materials. Subsequently, we forward-project the metal parts from the 3D volume to the 2D projections. This approach is helpful in difficult situations, if segmenting the metal in the projections is not immediately possible. Disadvantages of this approach are higher computational costs and accuracy errors. The first type of accuracy error is introduced by the reconstruction algorithm. During the discretization of the back-projected image the reconstructed data is sampled into a regular volume grid. This leads to an information loss and prevents an exact inverse mapping using the forward projection. Another source of precision error is the imperfection of the forward-projection algorithm.

3.3.3 Forward Projection

The goal of the forward-projection step is to project the segmented metal voxels from the reconstructed 3D volume back to the 2D projection images. The input to this workflow stage are the volume with segmented metal and the set of projection images. The areas of the projection images where metal is mapped to are filled with a void value. The output of the algorithm is a modified set of projection images. The forward projection is closely related to the reconstruction algorithm and uses the same transformations and scanning geometry.

An ideal forward projection would require solving a density integral for each projection pixel, where integration is done over the volume of the pyramid with apex at the X-ray source position and base at the detector cell. As exact forward projection is complex and computationally expensive, we use an approximate forward-projection algorithm.

The forward-projection works as follows:

- for every segmented voxel find the corresponding pixels on every projection image
- fill the corresponding pixels with the void value.

The forward-projection technique has to take into account partially covered pixels. Otherwise sampling artifacts may occur at the border of the projected metal. We include all the partially covered pixels to be part of the projected metal area. For this purpose we calculate the length of the voxel diagonal mapped on the projection plane. This is the coverage diameter. Then we map the center of the voxel to the projection plane and find the corresponding pixel index. This is the center pixel. We consider all those pixels as covered which intersect with the

axis-aligned square positioned at the projected voxel center and with side length equal to the coverage diameter. This leads to an overestimation of the projected metal area. The overestimation should not be a serious problem because the non-metal density is later interpolated across the covered pixels. It would be more serious to miss removing any metal.

As forward-projection performs an independent sequence of computations for every voxel, it is well suited for a GPU-based execution. We used CUDA for the implementation. The parallelization is done in a way that every voxel is forward projected in a separate thread. The pseudocode of the forward-projection is listed in Algorithm 1.

Algorithm 1 FORWARD-PROJECTION

The function `VoxelToProjection(voxel, proj)` returns the coordinates of the voxel *voxel* in the projection *proj*.

The function `GetCoverageRadius(voxel, proj)` returns the coverage radius *covRad* of the voxel *voxel* in the projection *proj*.

x and *y* are integer values indicating indices of pixels in the projection.

The function `integer(val)` returns the integer part of the floating point variable *val*. The value `VOID_VALUE` designates void pixels.

```

1: for all voxel  $\in$  Volume do
2:   if voxel.isMetal == true then
3:     for all proj  $\in$  Projections do
4:       covRad = GetCoverageRadius(voxel, proj)
5:       cPix = VoxelToProjection(voxel, proj)
6:       x1 = integer(cPix.x - covRad)
7:       x2 = integer(cPix.x + covRad)
8:       y1 = integer(cPix.y - covRad)
9:       y2 = integer(cPix.y + covRad)
10:      for x = x1 to x2 do
11:        for y = y1 to y2 do
12:          proj.pixels[x][y] = VOID_VALUE
13:        end for
14:      end for
15:    end for
16:  end if
17: end for

```

3.3.4 Interpolation

The interpolation step of the workflow takes projections with voids as input and produces projections with filled voids as output. As voids are left in metal areas of the projections, we use interpolation to fill these empty regions. As approximation we use the information from the surrounding pixels. There are various ways to do the void interpolation. The interpolation can be done in 2D (taking into account only the data of a single projection image) or in 3D (taking

into account the data of neighboring projections). Additionally, various interpolation techniques can be used. Examples are linear, bilinear, bicubic [35] or B-spline [72] interpolation.

Filling the voids is an image inpainting problem. Modern image inpainting methods mainly work with 2D images and are computationally expensive when applied to large 3D data. Therefore we consider a conventional interpolation strategy which is effective in processing large 3D volumes and which can be easily performed in parallel on the GPU. We use a 2D row-wise interpolation for regenerating the data in the voids. The interpolation works as follows:

- Interpolation is done for every row of every projection image
- Every pixel in the row is serially checked against the void value; the first and the last pixel of the void are detected
- When the last pixel of the void is reached, all pixels of the void are filled with interpolated values and the algorithm continues with the next pixel
- The row interpolation finishes when the last pixel of the row is reached.

In this work we do the interpolation only row-wise as it is the optimal interpolation direction in many cases. However considering another interpolation direction based on the void geometry could improve the interpolation quality. The GPU implementation for the interpolation is written in CUDA. Every row is interpolated in parallel within a separate thread. The pseudocode of the interpolation algorithm is listed in Algorithm 2.

Algorithm 2 INTERPOLATION

The constants `OUTSIDE_VOID` and `INSIDE_VOID` indicate the state of the algorithm.

```

1: state = OUTSIDE_VOID
2: for all pixel ∈ Row do
3:   if state == OUTSIDE_VOID then
4:     if pixel.value == VOID_VALUE then
5:       start = pixel.x − 1
6:       state = INSIDE_VOID
7:     end if
8:   else if state == INSIDE_VOID then
9:     if pixel.value != VOID_VALUE then
10:      end = pixel.x − 1
11:       $\Delta = \frac{\text{Row}[\text{end}] - \text{Row}[\text{start}]}{\text{end} - \text{start}}$ 
12:      interpolatedValue = Row[start].value
13:      for x = start + 1 to end do
14:        interpolatedValue +=  $\Delta$ 
15:        Row[x].value = interpolatedValue
16:      end for
17:    end if
18:  end if
19: end for

```

3.3.5 Fusion

The fusion step of the workflow inserts the metal voxels from the volume containing segmented metal to the volume containing plastic with reduced metal artifacts. This is the 3D volume reconstructed from the projections containing plastic with interpolated voids. The result is a volume with reduced metal artifacts containing all the materials. We use the attenuation-coefficient threshold from the material-separation stage as a decision factor during the fusion.

To achieve a smooth appearance at the borders of the metal elements we apply interpolation to the greyvalues within a certain range around the threshold. This range is controlled by the blend radius. We blend the voxel values which are within the blend radius from the threshold using linear interpolation. If the voxel value in the metal volume is higher than the threshold plus the blend radius, we use the voxel value of the metal volume. If the voxel value in the metal volume is lower than the threshold minus the blend radius, we use the voxel value of the MAR volume. The pseudocode of the Fusion algorithm is listed in Algorithm 3.

Algorithm 3 FUSION

initialVolume is the initially reconstructed 3D volume, *MARVolume* is the MAR 3D volume and *fusedVolume* is the resulting fused 3D volume.

```
1: threshLow = threshold − blendRadius
2: threshHi = threshold + blendRadius
3: threshRange = threshHi − threshLow
4: for all voxelInd ∈ VolumeDimensions do
5:   recoVoxel = initialVolume[voxelInd]
6:   marVoxel = MARVolume[voxelInd]
7:   if recoVoxel < threshLow then
8:     fusedVolume[voxelInd] = marVoxel
9:   else if recoVoxel > threshHi then
10:    fusedVolume[voxelInd] = recoVoxel
11:   else
12:      $\text{blendCoef} = \frac{\text{recoVoxel} - \text{threshLow}}{\text{threshRange}}$ 
13:     diff = recoVoxel − marVoxel
14:     fusedVolume[voxelInd] = marVoxel + diff * blendCoef
15:   end if
16: end for
```

3.4 Visual-Analysis Tool for Metal-Artifact Reduction

We integrate all steps of the workflow in a visual-analysis tool. The basic idea is to provide the user with a convenient interface for executing the proposed MAR workflow on the various datasets. This is done by visually guiding the user through the steps of the workflow which require user input. User decisions are assisted with a set of visual-analysis techniques.

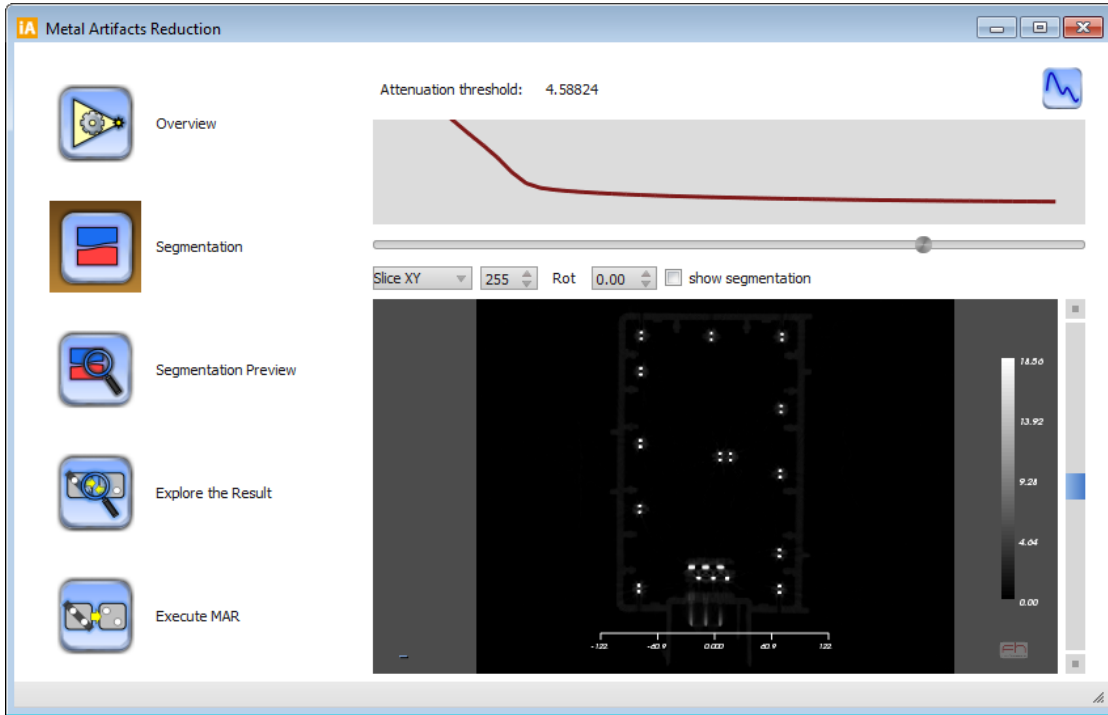


Figure 3.8: Tool’s GUI for the material separation.

The main parts of the tool contain functionality concerning visual parameter estimation for the material separation (Section 3.4.1) and concerning the visual result exploration (Section 3.4.2).

After the initial parameters are specified, the MAR workflow is executed for the selected projections by clicking the corresponding button. After the MAR workflow for the specified projections is successfully finished, the result will be displayed in a separate child window of the main application. This child window can be further used for various operations such as saving, exploring the data, volume rendering, or applying different filters.

3.4.1 Visual Parameter Estimation for Material Separation

The material-separation step of the workflow requires a threshold parameter to be specified by the user. The material-separation part of the tool helps the user to visually estimate the threshold, which is controlled using a slider (see Figure 3.8). We provide the user with several visual tools allowing the estimation of the threshold. First, a *threshold-preview plot* can be constructed and shown above the slider. This widget plots the total volume of the segmented metal for the set of threshold values. This plot is visually linked with the slider so that the plot value gives the segmented metal volume for the threshold corresponding to this slider position. Using this plot the user can locate a threshold where the metal volume stops falling rapidly and reaches a stable

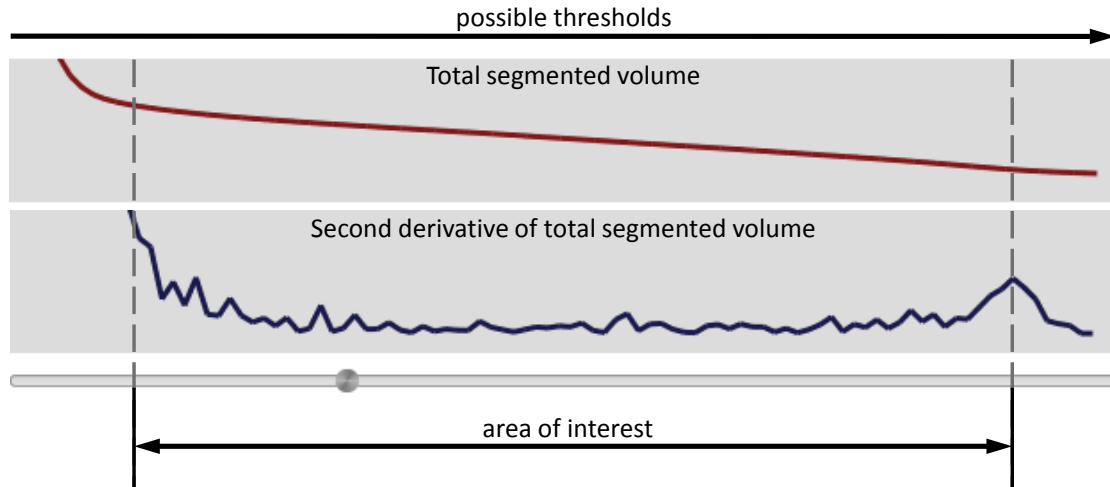


Figure 3.9: The threshold-preview plot example for the cube specimen.

size. This means that plastic is not included in the segmentation and no metal is false-negatively segmented. Instead of displaying the segmented metal volume, the absolute value of the second derivative thereof can be shown alternatively. An example of a threshold-preview plot is shown in Figure 3.9. The volume of the segmented metal is shown at the top and the second derivative of this function is depicted at the bottom of the image. The area where thresholding could provide good results is denoted.

Below the slider the *slice view* is located. A slice view is shown in Figure 3.10. This view shows a slice through the reconstructed volume. The slice direction, rotation and number can be specified using the corresponding GUI controls. The area showing the slice itself is fully interactive and allows zooming and shifting. Two additional widgets for the color map and the physical dimensions are shown on this view. When a voxel is covered by the mouse cursor, its index, position and data value are shown in the overlay box. The user can switch between the reconstructed 3D volume and the segmented 3D volume in the slice view. This allows an easy visual estimation of the parts in the reconstructed volume which are segmented for the given threshold value. Another helpful feature for the threshold estimation is the *MAR-result preview*. First, the user has to specify the range of the threshold to explore. Then the whole MAR workflow is executed for the thresholds in the given range. When the previews are calculated, the results are shown in the slice view. This conveys to the user how different thresholds directly affect the final result and allows selection of the threshold which provides the best MAR result. The user can switch the slice view between the resulting 3D volume and the difference between the resulting and the initially reconstructed 3D volume. This information gives a good visual estimation of how the MAR workflow changed the initial volume.



Figure 3.10: A slice view showing the XY-slice of the CUBE specimen. Brightness settings of the image were enhanced for illustration purposes.

3.4.2 Visual Result Exploration

After all the parameters for the MAR workflow are set, the user can explore the difference between the initial reconstructed 3D volume and the MAR volume. He/she can smoothly move from the initial reconstruction to the MAR volume. The amount of blending is controlled by a slider. The GUI for this step is shown in Figure 3.11. For the blending we use linear interpolation. The result is immediately shown in the slice view. Two transition steps from the initially reconstructed volume to the MAR volume are shown in Figure 3.12. Instant switching back and forth between the two images is available using the before/after buttons. It is clearly visible how metal artifacts represented by dark bands and streaking-noise are removed from the 3D volume. The tool is useful for the visual exploration of the artifact-reduction effect on the dataset. Changes in the dataset due to artifact reduction and the blurring introduced by the MAR workflow are visible using this interactive visual exploration tool.

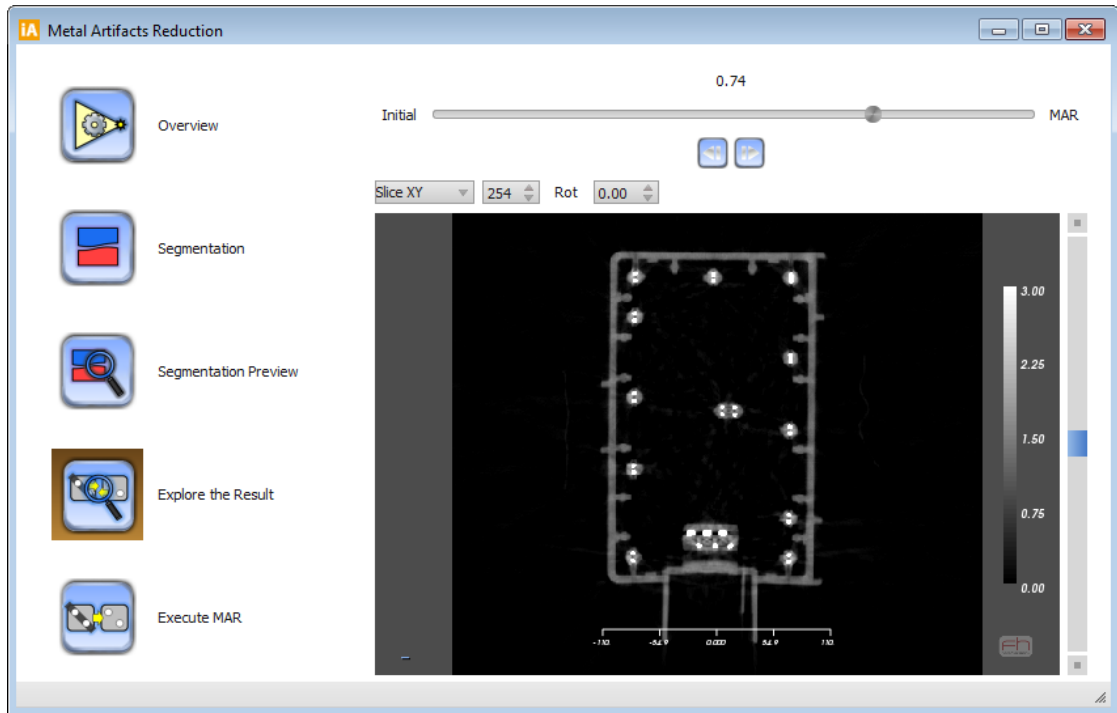


Figure 3.11: Tool's GUI for the visual result exploration.

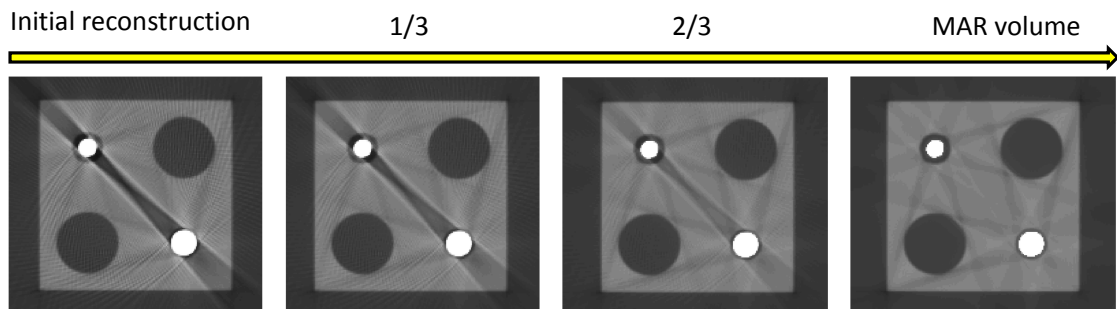


Figure 3.12: Exploration of the MAR result. Smooth transition between the initial reconstruction and the MAR result is shown. The numbers on the top show the blending between the initial reconstruction and the MAR volume. Brightness and contrast settings of the images were enhanced for illustrative purposes.

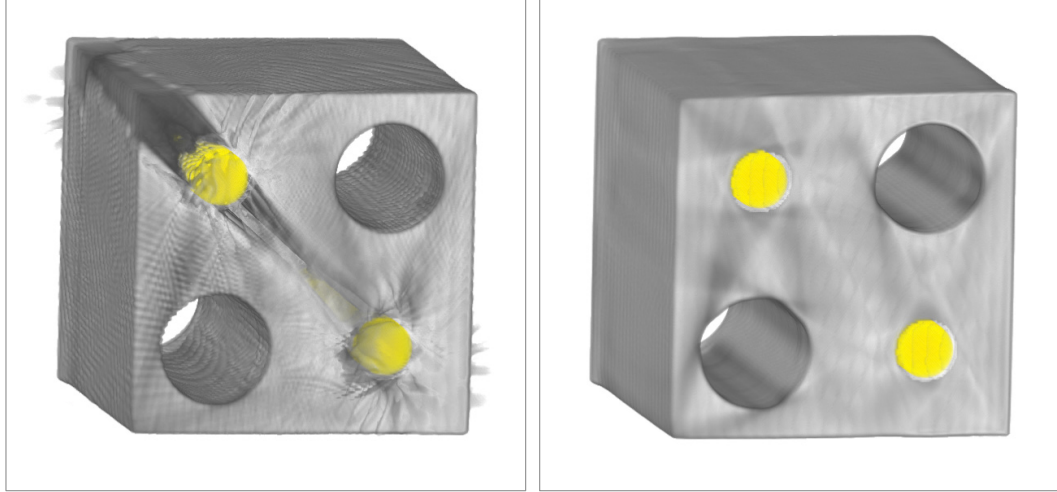
3.5 Implementation

The prototype application was implemented in C++. The slice view was implemented using VTK [64]. The GPU-based reconstruction, forward projection and interpolation were implemented using CUDA [49]. The data structures of ITK [28] were used for efficient handling of the 3D volume and the sinogram data. In addition, all the steps of the MAR workflow were implemented as ITK filters. This provides an abstraction from the voxel data type of the 3D volume and the pixel data type of the projection images. The ITK filter interface provides a flexible way of creating the filter pipelines by attaching the output of one filter to the input of another one.

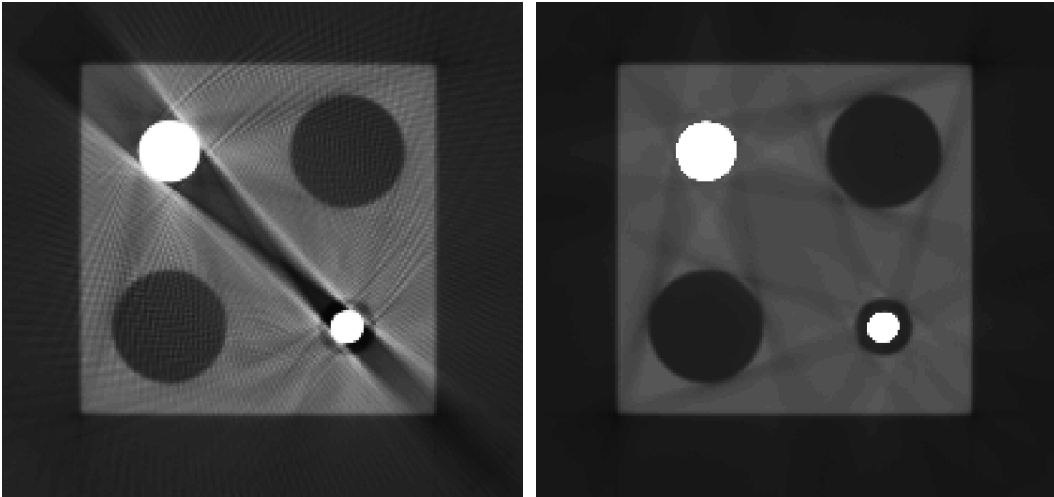
3.6 Results

For the evaluation of the MAR workflow we use several specimens. The first test part was obtained using a simulation of a 3DXCT scan. For simulation we used the GPU-based 3DXCT simulation tool by Reiter et al. [60]. The simulated test part is a plastic cube with four drill holes: two larger ones and two smaller ones with steel pin insertions. We will further refer to this specimen as CUBE. The steel pins of the CUBE test part occupy a relatively big region in the dataset. Therefore, this specimen is well suited for testing the robustness of the workflow concerning the maximum size of metal features. Other testparts are real-world multi-material components, obtained from a 3DXCT scan by using a Phoenix X-ray Nanotom 180 scanning device. The first real-world specimen is a plug made of plastic with two big metal rivets on the sides and smaller metal contacts. We will further refer to this test part as PLUG1. Another real-world specimen is a plug as well. The carrier made of plastic contains several small metal contacts. In addition to the 19 contact elements, this specimen has three larger-scale rivets located on the sides. We will further refer to this test part as PLUG2. The scanning presets used for the PLUG1 test part are: voltage = 170 kV, current = 400 μ A. The scanning modalities for the PLUG2 specimen are: voltage = 175 kV, current = 400 μ A. For both test parts 900 projections were taken with an integration time of 1000 ms per projection. The projection images were downsampled from 1024 \times 1024 to 256 \times 256 pixels using a bicubic interpolation method. The data resolution does not limit our method. However high memory costs should be considered when hi-res data are used. Due to the small size of the metal contacts, the PLUG1 and the PLUG2 specimens are well suited for testing the robustness of the workflow with respect to the large number of small metal features. All datasets used in the MAR evaluation have severe metal artifacts distorting the plastic and air regions and making a reliable material characterization impossible.

The results of applying the proposed workflow to the CUBE, PLUG1, and PLUG2 test parts are given in Figures 3.13, 3.14, and 3.15, respectively. The images on the left side show the original reconstructed 3D volumes, while the images on the right side depict the corrected 3D volumes. In all cases the improvement in volume and slice quality is clearly visible. By applying the proposed MAR workflow we managed to significantly improve the result for all specimens. The material interfaces got sharper and the amount of incorrectly classified plastic was significantly reduced. This allows us to achieve a higher quality material characterization and perform the material analysis in areas where it was not possible before. On the other hand,

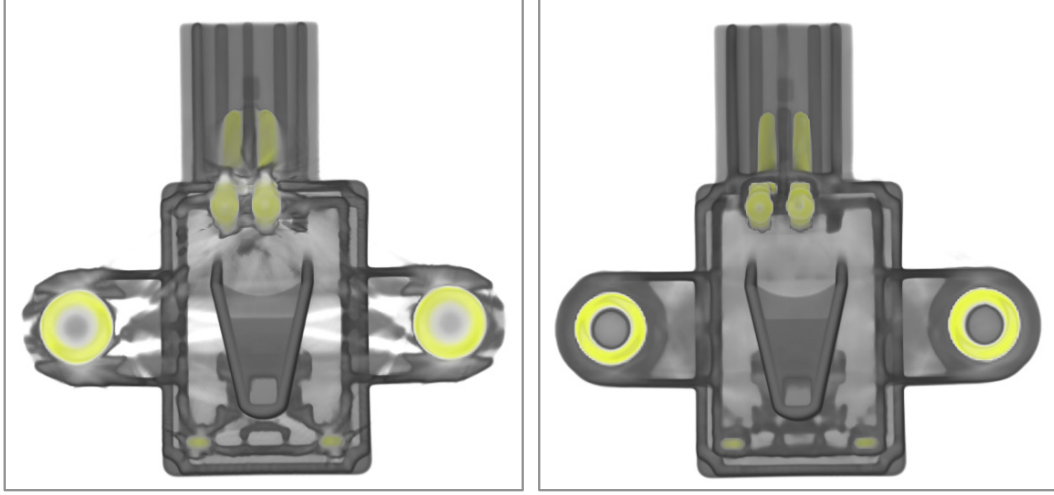


(a)

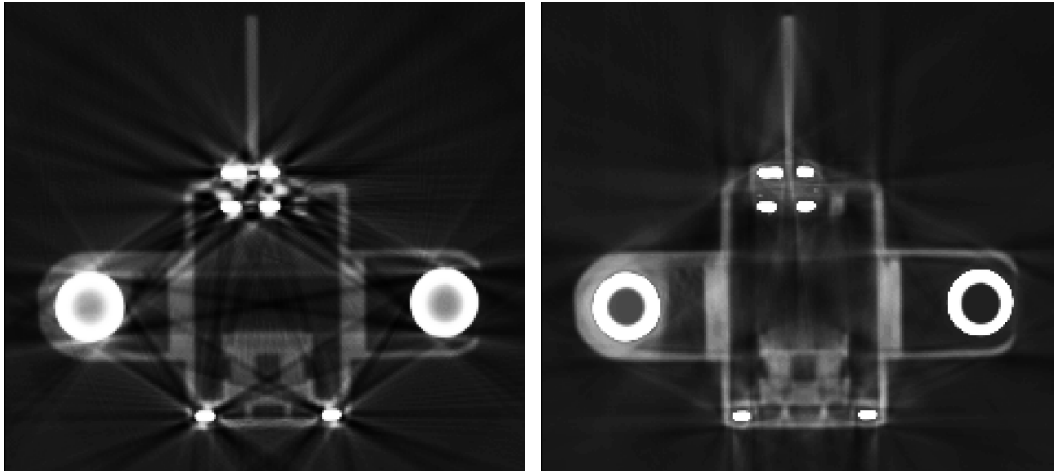


(b)

Figure 3.13: The results of the metal-artifact-reduction workflow for the simulated CUBE specimen. On the left the initial dataset is shown, on the right the same dataset after the metal-artifact-reduction workflow is given. Volumetric rendering (a) and XY-slice image (b) comparisons are given.

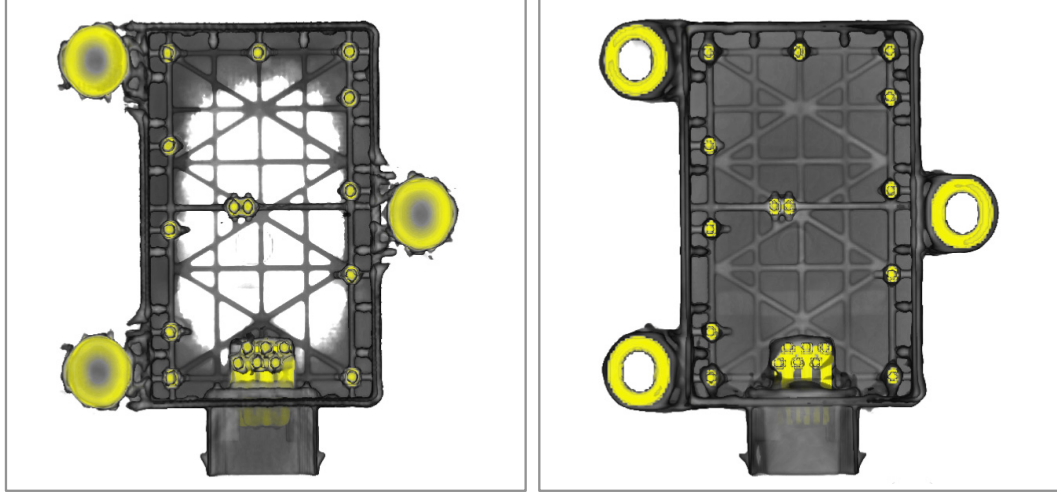


(a)

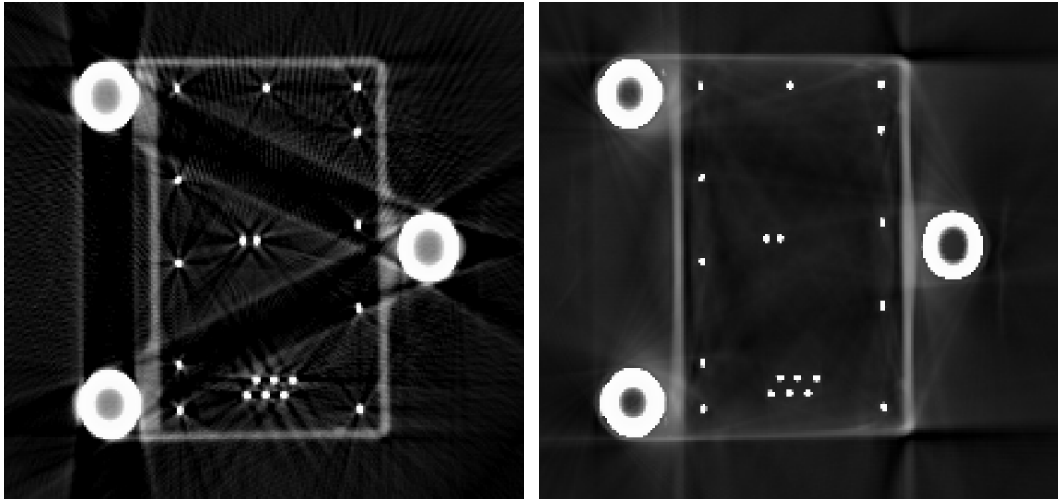


(b)

Figure 3.14: The results of the metal-artifact-reduction workflow for the real-world PLUG1 specimen. On the left the initial dataset is shown, on the right the same dataset after the metal-artifact-reduction workflow is given. Volumetric rendering (a) and XY-slice image (b) comparisons are given.



(a)



(b)

Figure 3.15: The results of the metal-artifact-reduction workflow for the real-world PLUG2 specimen. On the left the initial dataset is shown, on the right the same dataset after the metal-artifact-reduction workflow is given. Volumetric rendering (a) and XY-slice image (b) comparisons are given.

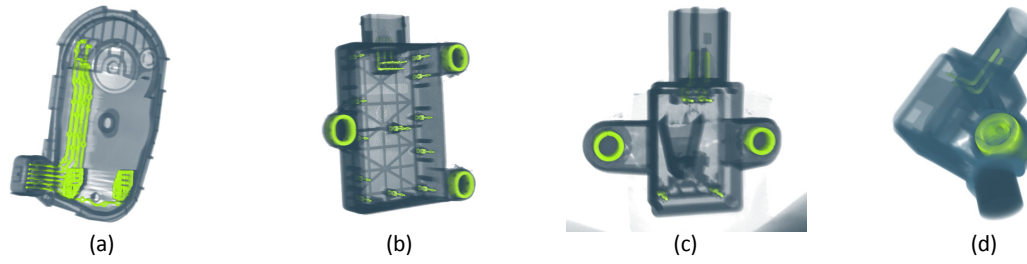


Figure 3.16: Specimens used for the profile-line evaluation: DVE5-2 (a), FCI-1 (b), FCI-2 (c), and UFS (d).

the metal appearance is preserved. The greyvalues of the metal correspond to the values in the original reconstructed volume. Sometimes the MAR method introduces blurring of the plastic edges due to interpolation. The amount of this blurring depends on the geometry of the specimen characterized by the size and the location of the metal parts.

Our approach does not treat beam-hardening artifacts introduced by the plastic. Only metal artifacts are corrected. Suppression of the streaking artifacts results in a lower noise-level in the dataset. This leads to a more evident appearance of the plastic beam-hardening artifacts. These artifacts are present in the original data as well and MAR does not amplify them. This may be one of the reasons for the star-shaped artifacts surrounding the metal parts of the CUBE specimen. The residual artifacts may as well arise from metal parts (due to under segmentation), or from other effects not considered.

Additionally, we perform side-by-side comparison of profile-line plots for four real-world specimens: electric plugs (see Figure 3.16). Figure 3.17 shows profile-line plots for the evaluated specimens. We have selected locations for the profile lines which contain metal, plastic and air regions and are strongly affected by dark bands. One representative profile-line plot is given for every specimen before (left) and after (right) MAR. Before MAR strong dark-band artifacts in form of concavities with lower attenuation coefficients can be seen in the profile plots. These artifacts are especially strong for the DVE5-2 (Figure 3.17a) and UFS (Figure 3.17d) specimens. For the FCI-1 specimen, metal artifacts result in concavities with low attenuation coefficients at the center of the plot (Figure 3.17b). Also for the FCI-2 specimen artifacts are present in the center and in the neighborhood of metal rivets. These artifacts are marked with arrows. After the MAR is applied, the line-profile plots show a significantly reduced amount of metal artifacts.

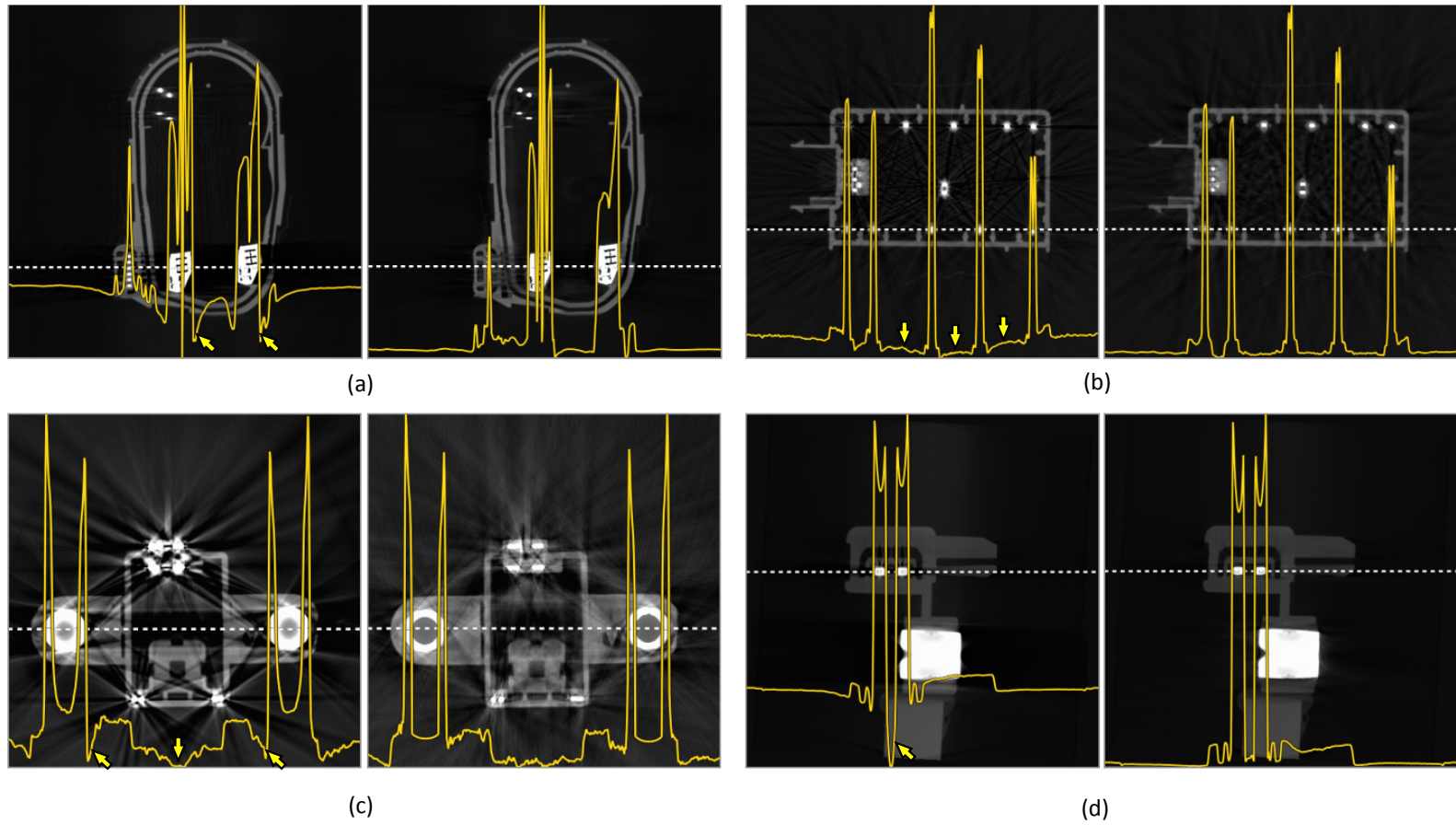


Figure 3.17: Profile line evaluations for the specimens: DVE5-2 (a), FCI-1 (b), FCI-2 (c), and UFS (d).

3.7 Conclusion

In this chapter we present an adaptation of a projection-based metal-artifact reduction (MAR) workflow for 3DXCT and in particular for industrial 3DXCT. We discuss a visual tool integrating all steps of the described MAR workflow. The tool guides the user through the sequence of steps. It provides visual-analysis functionality allowing interactive parameter estimation for the material separation stage. Additionally, the visual exploration of the MAR result and of the workflow impact on the volume is available. We have evaluated the presented workflow on both simulated and real-world MMC specimens with metal substructures of various sizes. Metal-artifact reduction was achieved for all tested MMCs. The visual evaluation shows a significant reduction of the metal artifacts. The artifact reduction enables a reliable dimensional measurement and material exploration in areas where this was not possible without scans of the disassembled specimen. This helps industrial 3DXCT experts to save scanning time and resources.

The 3D sinogram allows taking into account neighboring projections. Therefore additional information can be used in the material-separation and the void-interpolation stages of the MAR workflow. In the presented algorithm we do not make use of such additional information. Using interpolation schemes that operate in 3D space and improving the segmentation in the reconstructed 3D volume by checking against the 3D sinogram are promising topics for further research. The quality of the metal segmentation is essential for achieving a good MAR result. Our material separation requires the user to define a threshold parameter. One important assumption of this segmentation technique is that the scanned data allows metal separation by thresholding. This requires that the density difference of the metal and other materials of the object is large enough to enable a proper distinction. In problematic cases (e.g., industrial MMCs composed of many materials with similar densities) more sophisticated segmentation techniques may be applied. Another limitation is that the error estimation of the MAR workflow is difficult, as in most cases the ground truth is not available. In future work an error estimation could be performed by comparing the MAR results with artifact-free simulations or scans of the disassembled specimen. Additionally, applying the workflow to dual-energy 3DXCT could improve the quality of metal-artifact reduction. Despite the mentioned limitations, the presented MAR algorithm shows a significant metal-artifact reduction for industrial MMCs containing metal and plastic. This is quite advantageous for further material characterization and exploration.

Fuzzy CT Metrology: Dimensional Measurements on Uncertain Data

Metrology through geometric dimensioning and tolerancing is an important instrument applied for industrial manufacturing and quality control. When 3DXCT is applied for metrology the location of the specimen surface is estimated based on the scanned attenuation coefficients. As opposed to mechanical measurement techniques, the surface is not explicit and implies a certain positional uncertainty depending on the artifacts and noise in the scan data as well as the surface-extraction algorithm. Conventional 3DXCT measurement software does not consider the uncertainty in the data. In this chapter we present techniques which account for uncertainty arising in the XCT metrology workflow. Our technique provides the domain experts with uncertainty visualizations, which extend the 3DXCT metrology workflow on different levels. The developed techniques are integrated into a tool utilizing linked views, 3D labeling, and plotting functionalities. The presented system is capable of visualizing the uncertainty of measurements on various levels-of-detail. Common geometric tolerance labels are provided and enhanced with probability box plots. Additionally, the uncertainty information is mapped to the thickness of the employed reference shapes. Finally, we incorporate the uncertainty of the data as a context in commonly used measurement plots. The proposed techniques provide an augmented insight into the reliability of geometric tolerances while maintaining the daily workflow of domain specialists. They give the user additional information on the nature of areas with high uncertainty. We provide an evaluation of the presented methods based on feedback from domain experts in collaboration with our company partners. [5]

4.1 Introduction

Geometric tolerancing and dimensional measurements are well established methods in industrial quality control. They are the basis of assuring the manufacturing quality of industrial products. In most cases tactile measurements using coordinate measurement machines (CMMs) or optical

coordinate measurement techniques are the methods of choice. To achieve the geometric tolerancing and dimensional measurements of the features of interest, first a measurement plan has to be set up. The measurement plan incorporates measurement features as required for the quality control of the manufacturing processes. After the measurements are performed and all measurement features are evaluated, properties as line straightness, flatness or circularity are computed. These properties are analyzed and interpreted using visual representations, e.g., line profiles or polar plots.

Three-dimensional X-ray computed tomography (3DXCT) is a powerful technique for generating a digital 3D volumetric dataset of a specimen from 2D X-ray penetration images (projections). The set of 2D projections is acquired by radiating the scanned object with X-rays. For each angular position of the specimen a 2D projection image is obtained. A reconstruction algorithm is then applied to the projections to compute the corresponding digital 3D dataset of the scanned specimen. The ability to capture both internal and external structures of the scanned object makes 3DXCT a very attractive tool for metrology purposes. It allows performing measurements of parts not accessible by tactile or optical systems as well as of not-metrology-friendly objects, e.g., transparent, reflecting, soft, or deformable materials. With 3DXCT it is not necessary to disassemble a specimen. This technique is increasingly employed in industrial metrology as the spatial resolution and the mechanical precision of modern 3DXCT systems continuously improved and now is high enough to perform measurements at the required level of accuracy.

One important distinction of 3DXCT data from the real object is that the surface of the object is not explicitly defined. The data are represented as a 3D volume of attenuation coefficients which correspond to the scanned material and its density. When conventional metrology is performed using tactile or optical measurements, the actual surface of a specimen has to be accessible. A stylus or an optical scanner is used in these systems to evaluate measurement features on the surface of the specimen. In contrast, when industrial 3DXCT is used for metrology purposes, the surfaces between material and air or between two materials (so called *material interfaces*) have to be estimated in the volumetric 3DXCT dataset. Only then measurements may be performed. In this case surfaces and interfaces between the different materials have to be defined for each dimensional-measurement feature of the specimen. The surface-detection technique which is used to determine the interfaces between different materials is one of the most critical aspects regarding dimensional metrology. It strongly affects the final measurement result as different surface detection algorithms can result in different interfaces.

Furthermore, the quality of the surface may spatially vary considerably due to various artifacts and irregularities, which are present in the volume data acquired by the 3DXCT scan. There are several parameters and influencing factors which affect and propagate errors and uncertainty in every stage of the workflow. Firstly, during the *scanning stage* the resulting quality of the scan is impacted by several groups of factors, e.g., by scanning parameters, various physical phenomena, and artifacts. Secondly, when *reconstruction* is performed, artifacts may also be introduced as a consequence of physical phenomena or by the applied 3D reconstruction algorithm. These effects are for example: noise, streaking artifacts, ring artefacts, and scattered radiation [20]. Thirdly, the *surface-detection stage* might produce interfaces with sometimes considerable positional uncertainty.

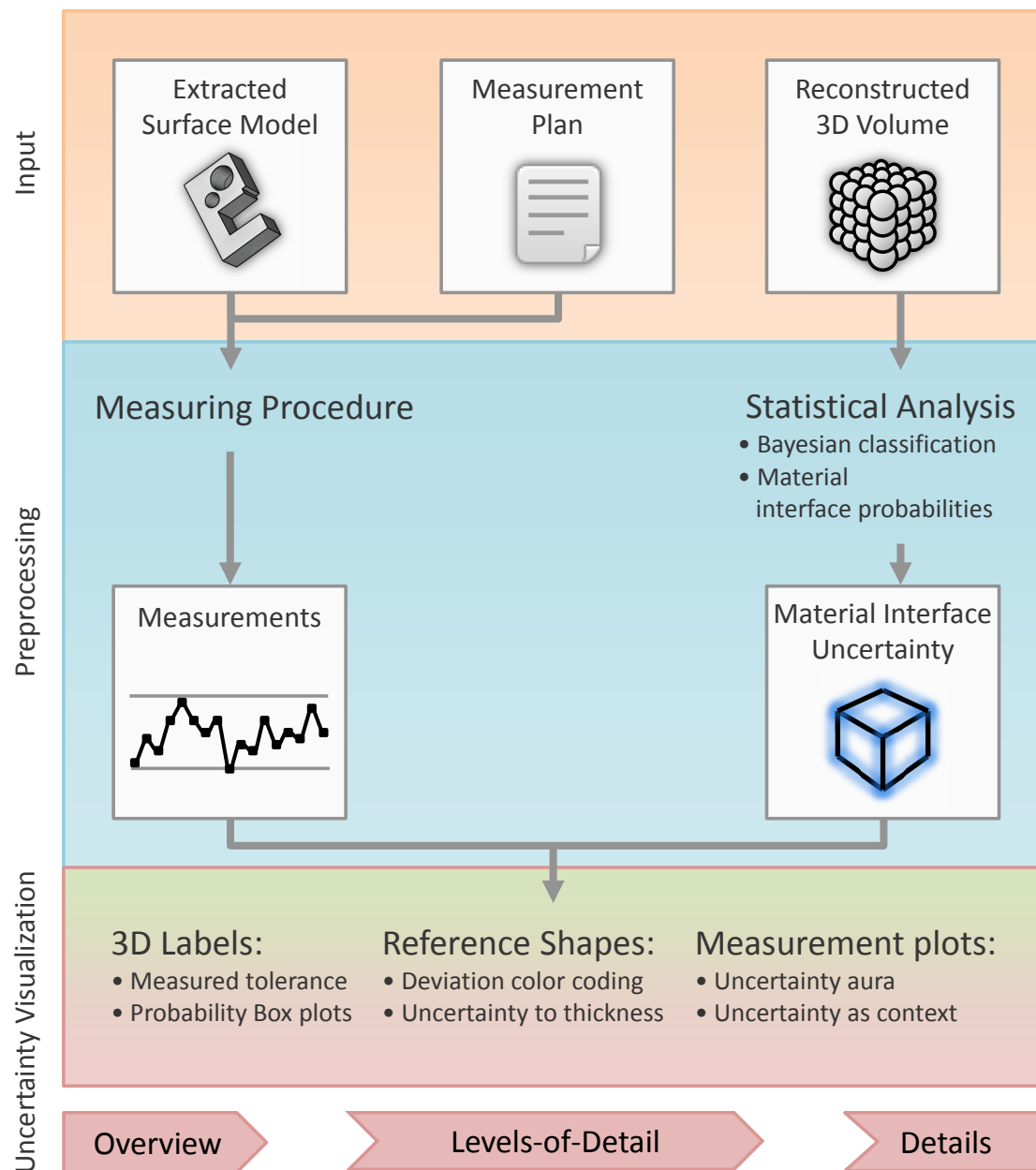


Figure 4.1: Workflow of our 3DXCT dimensional metrology system accounting for measurement uncertainties.

So far the estimated surface location is considered as the ground truth for measurements. The uncertainty of this surface is not taken into account during measurement analysis and evaluation. In this work we propose a technique which accounts for positional uncertainty in industrial 3DXCT metrology. We discuss common geometric tolerances and approaches concerning their visual evaluation in section 4.3. The general workflow is shown in Figure 4.1. We present a 3DXCT metrology system which accounts for measurement uncertainty. It incorporates two stages: the preprocessing stage and the uncertainty-visualization stage.

The preprocessing stage consists of two steps: probing of the measurement feature and statistical analysis. During the probing step (section 4.4) a list of measurements from a measurement plan is evaluated. Such measurements meter the deviations of the evaluated features from ideal shapes such as lines, planes, circles, or cylinders (section 4.3). The 3D surface model extracted from the reconstructed 3D volume is then used to perform measurements. For every measurement feature from the measurement plan a set of points is probed on the extracted surface. These data are then propagated further in the workflow to the uncertainty-visualization stage. As a second preprocessing step, we apply a statistical analysis (section 4.5) on the reconstructed 3D volume data in order to estimate the uncertainty of the material interfaces of the specimen.

During the uncertainty visualization stage of the workflow, we encode information about uncertainties in graphical representations commonly used for a measurement analysis and for an evaluation by metrology experts. The design of our uncertainty visualizations follows Shneiderman’s visual information seeking mantra [68]: “Overview first, zoom and filter, then details-on-demand”. The uncertainty of measurements is depicted on various levels-of-detail. First, an overview of the measurement uncertainties is provided using 3D labels (section 4.6) and reference shapes (section 4.7). Afterwards we provide the detailed uncertainty information by enhancing measurement plots. The visualization techniques to depict uncertainty through measurement plots are described in section 4.8. We propose two visualization approaches to depict the underlying uncertainty of the measurement: displaying the uncertainty of the probed positions using an uncertainty aura (section 4.8.1) and visualizing the uncertainty context (section 4.8.2).

Our approach does not modify the existing workflow of visual measurement evaluation. It extends the workflow with additional information about the underlying uncertainty of the measured positions in order to improve the process of decision making and measurement evaluation.

The main contributions of this chapter are:

- to statistically analyse the reconstructed 3D volume data in order to estimate probabilities of material interface locations
- to design uncertainty visualization techniques providing information about measurement uncertainty on various levels-of-detail. The visualizations proposed are: encoding uncertainty as thickness of the reference shapes, 3D labels extended with probability box plots, and an extension of common measurement plots with uncertainty information, where uncertainty is given as the context
- to present an integrated tool performing data preprocessing and utilizing linked interactive views (Figure 4.2) for supporting the exploration and visualization of the measurements’ uncertainty.

4.2 Related Work

Geometric tolerancing and metrology for quality control is defined in various standards: the ISO standards and American Standard ASME Y14.5M. Geometric tolerances are usually communicated using a symbolic language on engineering drawings. A description of the current state of the art regarding geometrical dimensioning and tolerancing can be found in the literature, e.g. in the book of Georg Henzold [23].

The uncertainty in 3DXCT scans is influenced by many factors. First, there is a large parameter space for the 3DXCT device itself [39]. These parameters have to be specified by a system technician before the scanning procedure. The X-ray source defines the characteristics of the emitted X-rays regarding intensity and quality of the beam [6]. This is the first major origin of uncertainty in an 3DXCT scan. The beam power is characterized by voltage and current of the electron beam shot at the target. The beam power exerts a direct influence on the beam intensity and hence the amount of radiation energy generated. The specification of the optimal current and voltage for a specific measurement task is difficult, and is an additional source of uncertainty. Furthermore, X-ray attenuation highly depends on the material composition of a specimen and each material's attenuation coefficient. The attenuation coefficients define the maximally possible penetration length through a specimen. The geometry of the specimen and its position and orientation in the X-ray beam may further influence the quality of an X-ray scan [4]. Additionally, various physical phenomena occurring during the 3DXCT scanning can affect the final result. One example of such phenomena are temperature drifts of the 3DXCT system's components (X-ray source, motors, drives, detector, electronics), as well as temperature changes in the specimen. These drifts and changes may be corrected using temperature compensation techniques [38]. Also the mechanical precision of the manipulators themselves has a significant impact on the resulting accuracy. Finally, 3DXCT scans may contain various artifact types. Artifacts are defined as artificial structures in the dataset which do not exist in the scanned specimen [20]. The most prominent example is beam hardening. Beam hardening denotes the effect of low-energy X-ray photons being attenuated stronger than high-energy photons. So after the polychromatic X-ray has travelled a certain distance through the material, low energy X-rays are extinguished, while only the high energy X-rays are passing through the specimen. This results in contrast deterioration and nonlinearities in the reconstructed 3D volume. The beam hardening effect may be overcome using linearization techniques [33, 34].

Uncertainty visualization is currently considered as one of the prime visualization research challenges [30]. During the last decade uncertainty visualization has found its use in various application areas ranging from medicine to meteorology. An overview of applications for uncertainty visualization is given in the survey by Zuk and Carpendale [84]. An early work of Rheingans and Joshi [61] is investigating the visualization of molecules with positional uncertainty. Various visualizations depicting the uncertainty of isosurfaces are explored by Rhodes et al. [62]. In the work by Berger et al. [8] uncertainty is visualized with regards to a potentially insufficient sampling density and inaccurate predictions for multi-dimensional parameter spaces. Coninx et al. [13] visualize uncertainty by adding animated Perlin noise to areas with high uncertainty. Various uncertainty visualization possibilities combined with volume rendering are explored by Djurcilov et al. [14]. Grigoryan and Rheingans [18] use a point cloud approach to

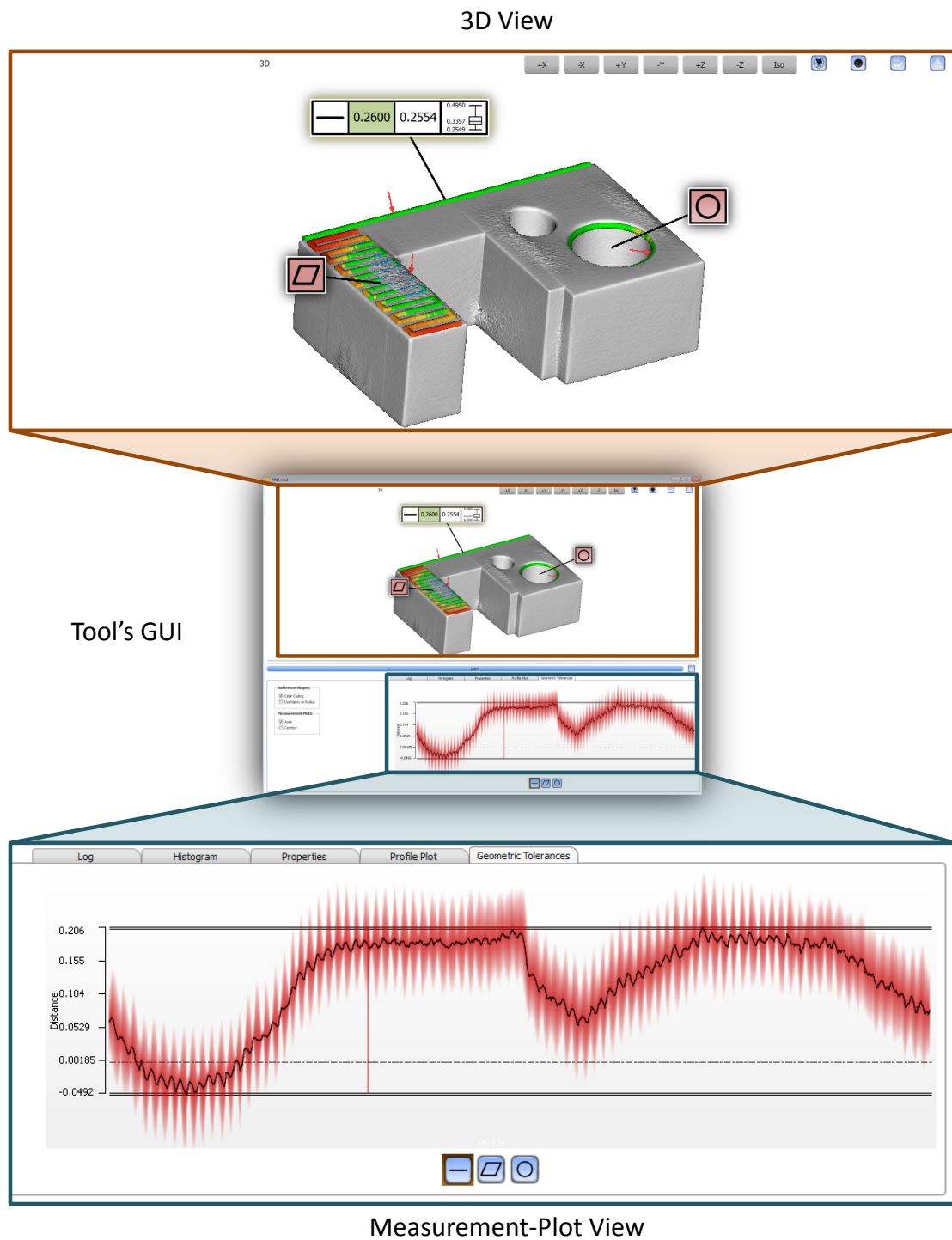


Figure 4.2: The tool's user interface. The 3D view is shown at the top and the measurement plot view is shown at the bottom.

depict spatial uncertainty in the data. Combined probabilistic classification results from multiple segmentations are visualized to allow risk estimation in the work by Kniss et al. [36]. Saad et al. [63] introduce an interactive analysis and visualization tool for probabilistic segmentation in medical imaging utilizing appearance prior information extracted from expert-segmented images. Prassni et al. [57] have presented a user-assisted segmentation tool. The tool improves the segmentation in an iterative feedback loop by minimizing segmentation uncertainty. Partial range histograms are introduced in the work by Lundström et al. [41] to enable an automatic statistical classification. In another paper Lundström et al. [40] explore uncertainty visualization in medical volume rendering using probabilistic animations for medical diagnosis. The work by MacEarchen et al. [43] explores possibilities for geospatial data uncertainty visualizations. Pauly et al. [52] construct likelihood and confidence maps for a surface from a set of sampled points. Various applications include adaptive re-sampling, an algorithm for reconstructing surfaces in the presence of noise, and robust merging of a set of scans into a single point-based representation. Pöthkow et al. [55] explore in their work the positional uncertainty of iso-contours. The presented visualizations are combining color-coded isosurfaces with the uncertainty information depicted using direct volume rendering. In the following year two interesting papers have elaborated on the positional uncertainty of isosurfaces: Pöthkow et al. [56] introduced a probabilistic marching cubes method taking into account statistical correlations between probabilities. In another work Pfaffelmoser et al. [53] take into account correlations between random functions. They introduce an incremental update scheme that allows to integrate the probability computation into front-to-back volume ray-casting. An application of uncertainty visualization in a flooding-simulation scenario is given by Waser et al. [78]. The presented system accounts for input uncertainties and explores how these uncertainties in the boundary conditions affect the confidence in the simulation outcome.

Many works exist on *labeling and label placement*. Matkovic et al. [45] use labels for visualization. Collisions of labels are avoided using a physically-based spring model. Focus plus context rendering and levels-of-detail are utilized giving the user the possibility to explore a particular view in detail without losing the context information. Profile flags are presented by Mlejnek et al. [46,47]. The Profile Flag is a 3D glyph, which can be moved along an orthopedic surface. It contains a flag showing the local information around the profile flag's placement position.

4.3 Geometric Tolerancing

Industrial workpieces should usually be manufactured as precisely as possible. However, in practice it is hardly possible to produce them without any deviation from the desired reference shapes. This obliges manufacturers to adhere to required tolerances for the assembly or other subsequent processes. The geometric tolerances are specified in order to keep the deviations within acceptable ranges. To check this, measurements are performed for every specified geometric tolerance. The performed measurements are further evaluated and compared with the given tolerances. Additional evaluations using visual representations like measurement plots are carried out in cases which are particularly interesting for the experts. The workpiece is reduced to a set of features or geometrical elements, such as edges, planes, cylinders, cones, spheres,

etc. Geometrical tolerances are specified for these features. Following the corresponding ISO Standard there exists a fixed set of geometric tolerances [23] which evaluate deviations of these features from the ideal shapes. These shapes are called *reference shapes*. They include line profiles, circles, planes, cylinders, etc.

In this chapter we focus on several commonly used types of geometric tolerances [23] such as straightness, circularity, and flatness tolerances (see Figure 4.3). However, the presented approaches are expandable to other dimensional-measurement features. *Straightness* is defined as a geometric tolerance which specifies how much a feature may deviate from a straight line. This means that the profile along a line on the specimen surface shall be contained between two parallel lines which denote the allowed tolerance. If the straightness of a feature is measured, a set of points is sampled on the specimen surface while a probing tool is moving along an ideal straight line. After the measurement is evaluated, the measured data may be explored using a straightness plot (Figure 4.3 top/right). *Circularity* is a geometric tolerance that checks by how much a feature may deviate from a perfect circle. Circularity means that in a cross-section of the specimen surface, the profile (circumference) shall be contained between two coplanar concentric circles with a radial distance equal to the tolerance value. If the circularity of a feature is measured, a set of points is sampled on the specimen surface while a probing tool is moving along the ideal circle. After the measurement is evaluated, the measured data can be explored using a circularity plot (Figure 4.3 middle/right). *Flatness* is a geometric tolerance that evaluates how much a feature can deviate from an ideal plane. The flatness tolerance means that all profile points should be contained in a zone between two parallel planes with a fixed distance apart. If the flatness of a feature is measured, a set of points is sampled on the specimen surface while a probing tool is moving along a specific curve within the ideal plane. The curve might be an arbitrary one or a plane-filling one. After the measurement is evaluated, the measured data may be explored using a straightness plot as well.

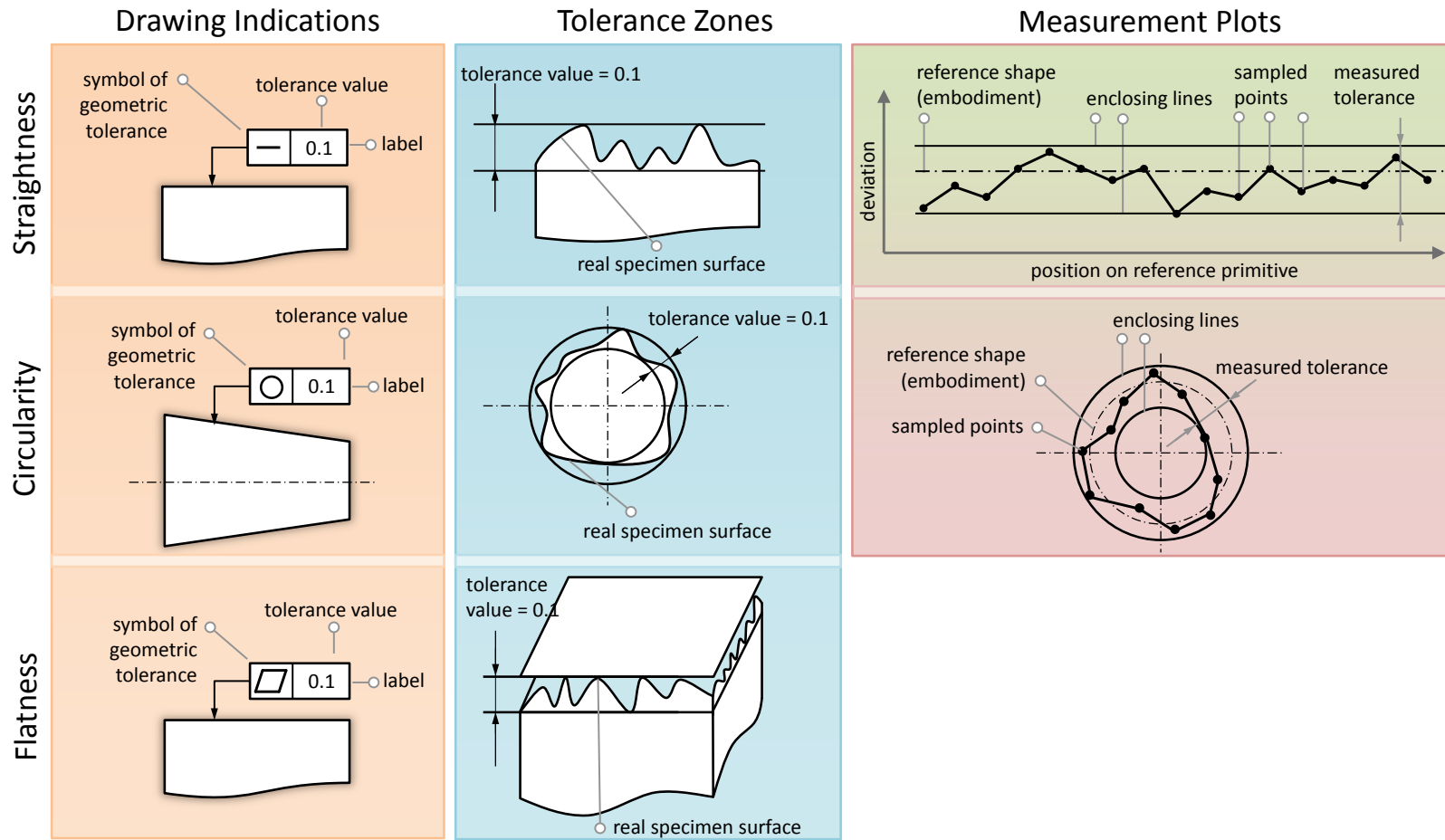


Figure 4.3: Geometric tolerances: straightness (top row), circularity (middle row), and flatness (bottom row) tolerance. The drawing indications for tolerances (left column) and the corresponding tolerance zones (middle column) are shown. Common measurement plots as the straightness plot (top/right) and circularity plot (middle/right) are given as well.

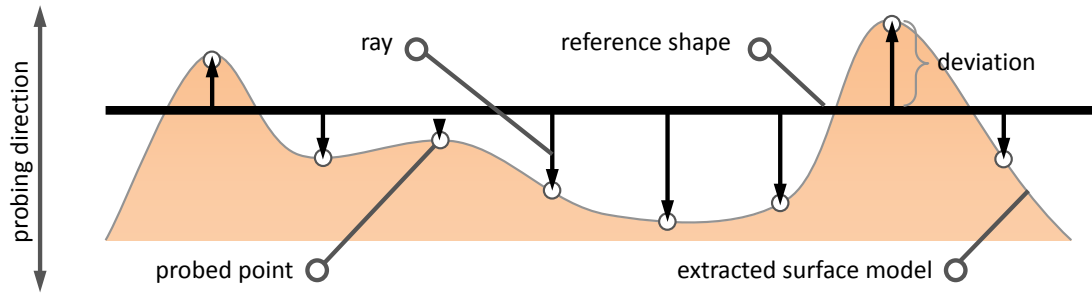


Figure 4.4: Measuring the straightness tolerance.

4.4 Measuring Procedure

The 3DXCT measuring procedure simulates a CMM probing process. In case of CMM probing a stylus is moving along the defined measurement trajectory. The deviations from the reference shape are calculated for a set of points probed on the specimen surface. In the case of 3DXCT the surface extracted from the reconstructed 3D volume is used to perform measurements. For every geometric tolerance in the measurement plan a set of points is probed on the extracted surface. Ray casting is used to determine the positions of the probed points on the surface. A measuring setup for the straightness tolerance is illustrated in Figure 4.4. In this example the reference shape is a line segment. It is uniformly sampled along the probing direction with a fixed sampling distance. A ray is cast from every point on the reference shape in the probing direction. The intersection of the ray with the surface closest to the reference shape is then calculated. The position of the corresponding probed point is given by the intersection point. The deviation at the probed point is set to the distance between the reference shape and the position of the intersection point.

Since the 3DXCT measuring procedure can operate on any provided surface, our system is not restricted to a particular surface extraction algorithm. The surface generated by any advanced surface extraction method may be provided as input for measurements.

4.5 Statistical Analysis

We use a statistical analysis to introduce information on uncertainty which characterizes materials of the specimen and corresponding material interfaces. We compute material interface probabilities for every voxel using two steps. First we apply an automatic statistical classification based on Bayes' decision theorem (section 4.5.1). This classification uses the reconstructed 3D volume as input data. The classification calculates posterior probabilities of belonging to each of the specimen's materials for every attenuation coefficient in the volume. The second statistical analysis step calculates material interface probabilities (section 4.5.2). This step takes the posterior probabilities as input and computes material interface probability for every voxel of the volume. These probabilities are stored in a material-interface probability-volume.

4.5.1 Bayesian Classification

The task of the classification is to determine for each voxel attenuation coefficient to which material it belongs. We assume C different material classes $\omega_1, \omega_2, \dots, \omega_C$. For example for a component made of plastic and metal: $\omega_1 \leftarrow$ air, $\omega_2 \leftarrow$ plastic, and $\omega_3 \leftarrow$ metal. Consider the attenuation value x . Lets denote $P(\omega_i|x)$ as the conditional probability which indicates that x belongs to the corresponding material class ω_i , $i = 1, \dots, C$. The classification assigns a probability vector $[P((\omega_1|x), P((\omega_2|x), \dots, P((\omega_C|x)]$ to every attenuation value x .

In this work we use an automatic Bayesian classification algorithm as described in the work by Heinzl et al. [22]. The classification is based on Bayes' decision theorem and consists of three major steps: feature selection, classifier selection, and estimation of the class conditional probability density function (PDF). For the first step, after the class is assigned to every material, attenuation coefficients of voxels are used to specify the feature vector. For the second step, a reliable material classifier is chosen. Several assumptions are made for the 3DXCT data. Homogeneous materials tend to generate constant attenuation coefficients. Due to various artifacts and irregularities introduced by the detector/X-ray source combination, attenuation coefficients are modified on the borders of a material. The normal (or Gaussian) distribution is often chosen in many applications to model such distributions. Consequently, a Gaussian distribution is assumed for the attenuation coefficients of each single material in the CT scan. During the last step, a custom automatic Gaussian curve fitting scheme is used to setup the PDF for every material (for details see [22]). Then normalization is applied to compute the final class conditional PDFs.

4.5.2 Material-Interface Probabilities

We introduce material-interface probabilities to represent uncertainty of material transitions in the specimen. During the statistical analysis stage, we estimate probabilities that a material interface is located at a certain position in space. The surface will be a material interface when it segregates points belonging to one material from points of another material. Therefore, we assume that the face between two voxels belongs to a material interface when it separates two different materials. This is true if the material of one voxel is different from the material of its neighbor. To illustrate this, consider two adjacent voxels A and B with corresponding attenuation values x_A and x_B . Lets denote a face between these voxels as $face_{A,B}$. Then the probability that the interface between any two materials is passing through this face can be calculated as follows:

$$P(face_{A,B} \text{ is interface}) = \sum_{i=1}^C \sum_{j=1, j \neq i}^C P((\omega_i|x_A) \cap (\omega_j|x_B)), \quad (4.1)$$

where $P((\omega_i|x_A) \cap (\omega_j|x_B))$ is the conditional probability that a voxel A and its neighbor B belong to different materials ω_i and ω_j for $i \neq j$. The computation of conditional probabilities requires the knowledge of correlations between the probabilities defined by the corresponding PDFs. The estimation of such correlations requires multiple realizations of the random variables. This could be done using multiple scans which is, however, not affordable in the 3DXCT metrology scenario. Additionally, in many cases physical effects which increase correlations (e.g., radiation scattering or partial-volume artifacts) are rather weak and can be neglected. Based on

these considerations, we assume that random variables defined by conditional PDFs are *stochastically mutually independent*. This means that if any particular voxel is known to belong to a certain material, it is neither more nor less likely that any other voxel belongs to this or some other material. It is known that two random events E_1 and E_2 are stochastically independent if and only if $P(E_1 \cap E_2) = P(E_1) * P(E_2)$. When taking this into account Eq.(4.1) will transform into:

$$P(\text{face}_{A,B} \text{ is interface}) = \sum_{i=1}^C \sum_{j=1, j \neq i}^C P((\omega_i|x_A) * (\omega_j|x_B)). \quad (4.2)$$

With Eq.(4.2) we can now compute the probability of a material interface for any face between two voxels. However, assigning the interface probability to faces has several disadvantages. For a 3D volume of resolution $X \times Y \times Z$ this requires storing $3 \times (X + 1) \times (Y + 1) \times (Z + 1)$ values. This results in a high memory consumption if high-resolution data are used. For example, the size of one of the datasets we investigate in the results section is about 1800 Mbyte. Storing interface probabilities for this dataset would require more than 5400 Mbyte. Therefore, we only store one value for every voxel in the volume. In this way we have to store just one value for each voxel. To achieve this we average for each voxel material interface probabilities of all its faces: The obtained probabilities are no longer represented by the PDFs since probabilities are not assigned to the attenuation coefficients but to the individual voxels. Every voxel can be considered as a separate random event which has two possible outcomes: the voxel contains an interface between two different materials or the voxel does not contain any interfaces. The probabilities of these two events sum to one for every voxel.

The interface probabilities of voxels are stored in the interface probability volume. After the statistical analysis we have an interface probability volume which estimates interface probabilities instead of a conventional surface estimation (e.g., isosurface).

4.6 3D Labels

Labels are commonly used in dimensional metrology for indicating geometric tolerances on 2D drawings (as seen in Figure 4.3). A label usually consists of the following elements: an arrow pointing at the tolerance feature, a symbol indicating tolerance type and allowed tolerance value. Based on this notion we introduce *3D labels*. The labels are drawn on the canvas of the 3D view and indicate measurement features on the extracted surface. The main intentions of the 3D labeling design are:

- to provide a high-level overview of the evaluated tolerances
- to give more details on demand
- to allow an easy navigation to the tolerance of interest for a further detailed evaluation.

An example of 3D labels attached to the measurement features in 3D is given in Figure 4.5. Each 3D label is represented as a rectangular billboard attached to a certain point in 3D (anchor). The billboard is always facing towards the viewer. The label is visually linked to the

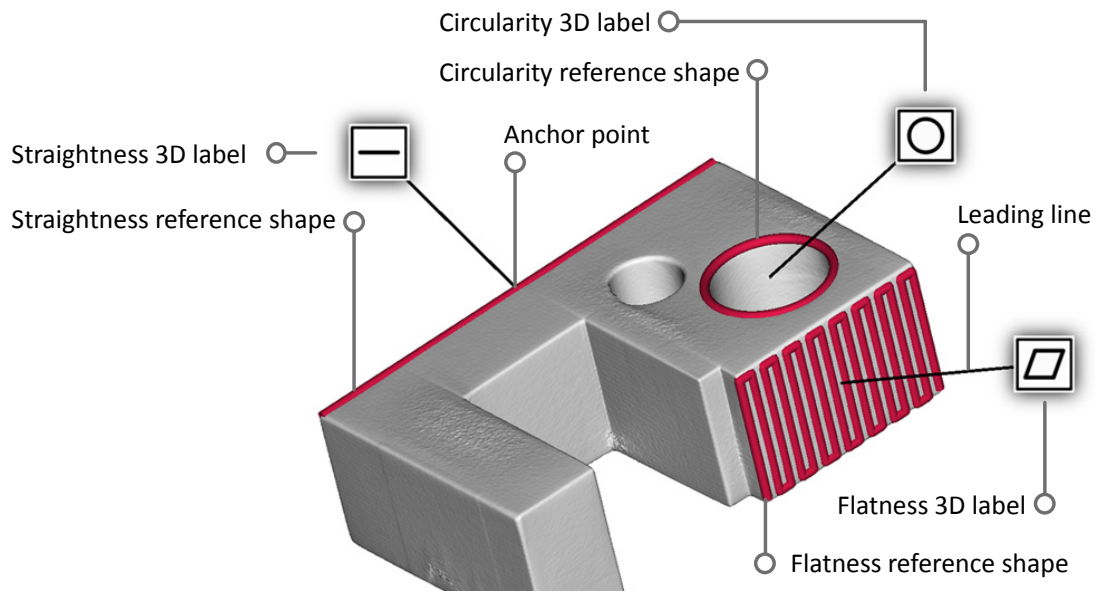


Figure 4.5: 3D labels and reference shapes for: straightness of the specimen's edge, circularity of the specimen's drill hole, and flatness of the specimen's face.

measurement-feature position on the extracted surface model using a leader line. The anchor on the extracted surface is calculated as the center of the corresponding reference shape. For example, in the case of the straightness tolerance it is the middle-point of a reference line. In the case of the circularity tolerance it is the center of the reference circle. The position of the label is calculated by adding a fixed-length offset to the anchor point. The offset is done in a direction facing away from the center of the specimen's 3D bounding box. This solves the label visibility problem for most of the cases. Additionally we always render 3D labels as an overlay on top of the 3D view. In this way labels are never occluded by the specimen's surface and only other labels can act as occluders if they are closer to the viewer. As typically only a few labels are involved in our visualizations, a more refined label-layout strategy was not considered to be necessary.

The 3D labels can provide information about a measured tolerance at two levels-of-detail. Each label can be visualized in one of two modes: the collapsed mode and the expanded mode. Individual labels can be collapsed or expanded via user interaction. All 3D labels in the 3D view can be expanded or collapsed simultaneously. To give a general overview of the performed measurements, labels are shown in the collapsed mode (Figure 4.5). Collapsed labels are used for a quick identification of the tolerance type as they only display symbols of the corresponding geometric tolerances (Figure 4.6a). If the user is interested in more details about some particular tolerance, expanded labels can be used (Figure 4.6b). If a label is expanded it shows the specified tolerance zone from the measurement plan. The background color is green if the measured deviation is within the allowed tolerance and is red otherwise. Optionally the measured tolerance and

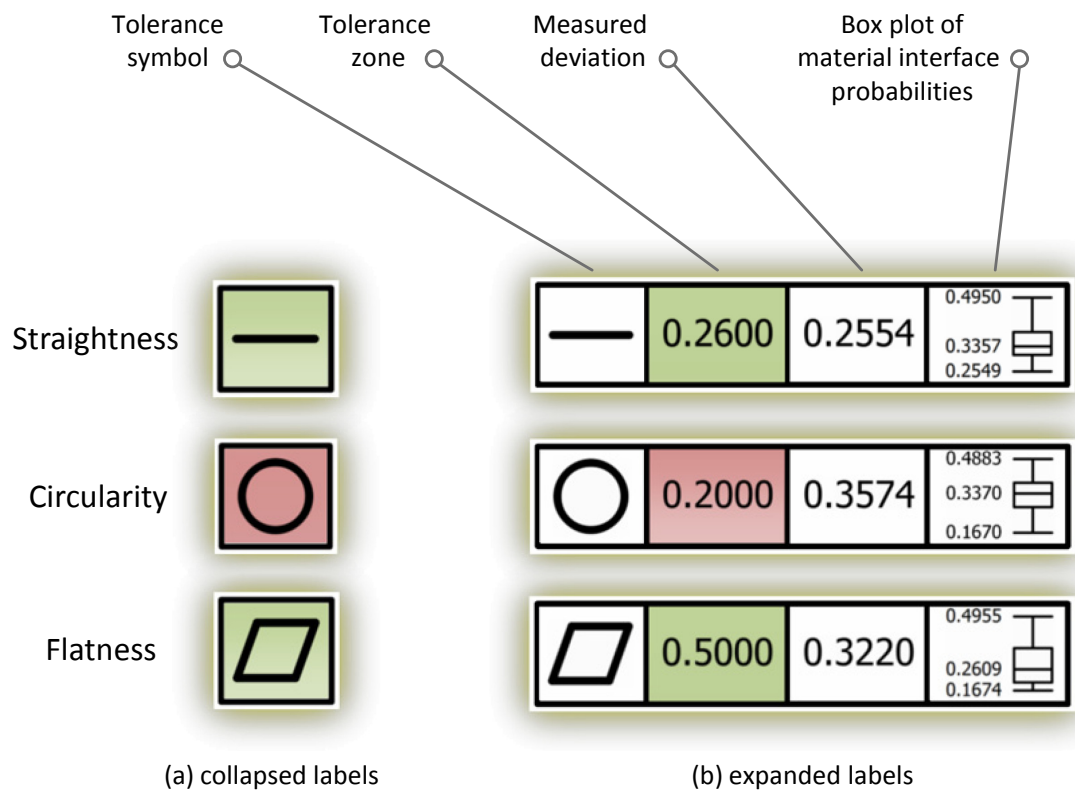


Figure 4.6: Collapsed (a) and expanded (b) 3D labels for the straightness, circularity, and flatness tolerances.

a box plot which encodes the distribution of material interface probabilities of the probed points can be shown on the label. Box plots are providing information on the uncertainty of the tolerance measurement. They depict such parameters of the probed points' interface probabilities as: the biggest and the smallest interface probability, the upper and the lower quartiles, and the median value. The numeric values on the expanded 3D labels provide a quantitative overview of the tolerance data. If the user is interested in even a more detailed investigation of the measurement, the label can be picked through user interaction. A corresponding measurement plot will be automatically displayed allowing a very detailed visual exploration.

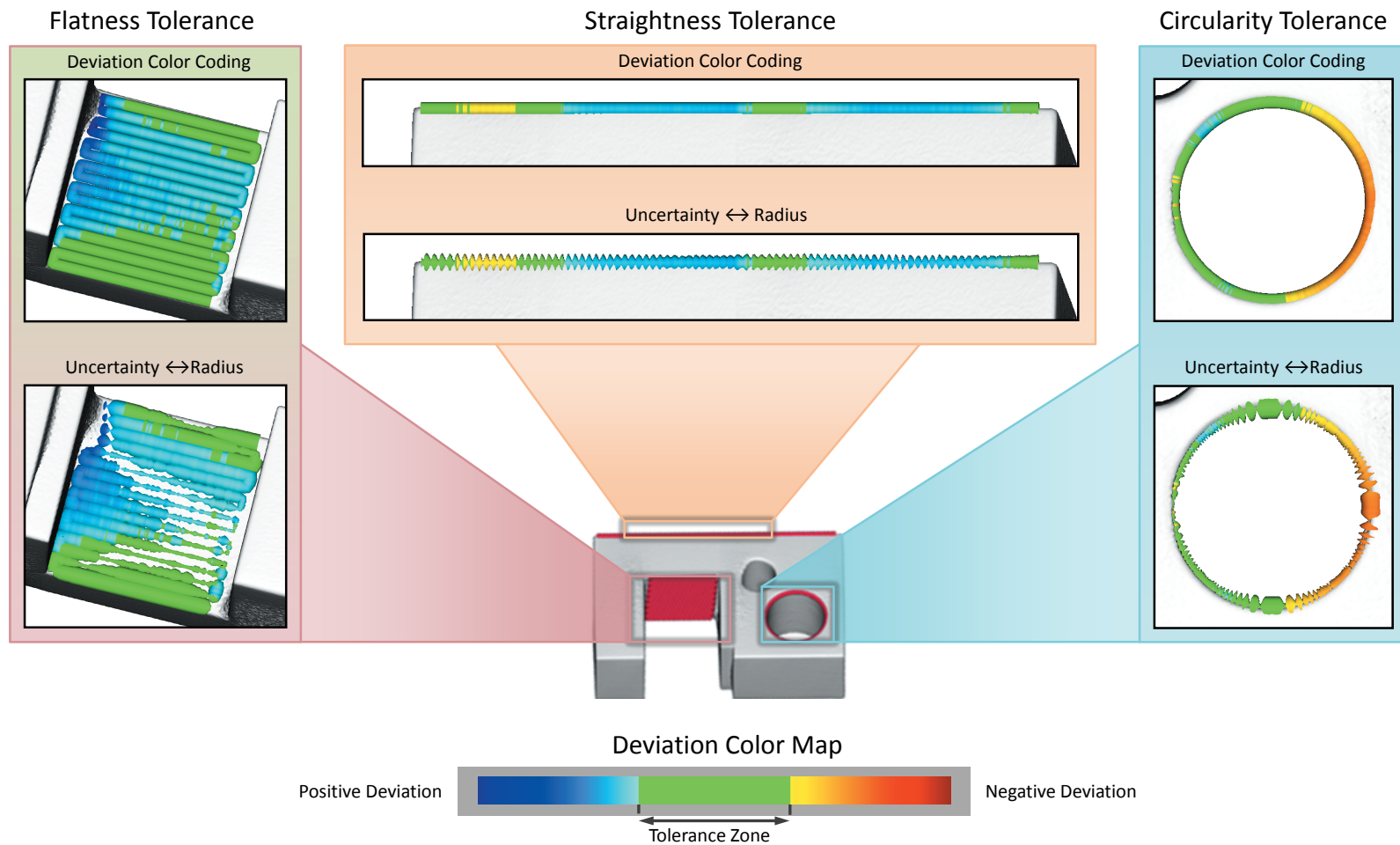


Figure 4.7: Reference shape visualizations for the straightness, circularity, and flatness tolerances. The deviation color map is shown on the right.

4.7 Reference Shapes

In geometric tolerancing the measured features are compared to the ideal shapes or *reference shapes*. These shapes include lines, circles, planes, cylinders, etc. Every measurement has its corresponding reference shape which is defined in the measurement plan. We visualize reference shapes in the 3D view combined with the extracted surface as context (see Figure 4.5). This allows the user to intuitively identify locations of measured features on the specimen surface. The shape of the reference provides an additional visual clue about the type of the geometric tolerance. For example, a line segment indicates the straightness tolerance, a circle indicates the circularity tolerance, and a space-filling line indicates the flatness tolerance.

We are using tubular structures to represent the reference shapes. We generate a tube for every reference primitive as follows. First, a poly-line is calculated for the reference shape. Points of the poly-line correspond to positions where the probing is done. The straightness tolerance, for example, is computed by uniformly probing n points along the reference line segment. Then, the resulting poly-line will look like a straight line and will consist of $n - 1$ line segments. On each of the line segments a cylinder is positioned to generate the entire tube of the reference shape.

Reference shapes allow the user to quickly identify the spatial position of each individual measurement. The default reference primitive is a red-colored tube with constant radius (Figures 4.5 and 4.7). On the next level-of-detail we present extensions to the visualization of the reference shapes. These visualizations provide an overview of the measurement parameters and can be used to estimate the overall quality of the measurement. To achieve this, we map measurement parameters to the visual properties of the reference shapes. Firstly, the deviation along the reference shape can be color coded on the tubes. An example of this deviation color coding is given in Figure 4.7. Our goal is to quickly allow the user to detect measurement areas which are outside the tolerance zone and to estimate the direction and the value of deviations. For this purpose we apply a deviation color map commonly used for the 3DXCT metrology applications (see Figure 4.7). This color map encodes deviation values within the tolerance zone in green. Strong positive deviations are colored in dark blue and strong negative deviations in dark red. This color scheme is familiar to the 3DXCT metrology specialists and permits a quick visual analysis of the deviations.

To provide an additional overview of the underlying measurement uncertainty, another visualization maps the measured points' interface probabilities to the thickness of the tube (see Figure 4.7). The points with maximum material interface probability are displayed with the minimum tube radius and the points with bigger probabilities are displayed with smaller tube radii. This results in the blob-like appearance of areas with high uncertainty.

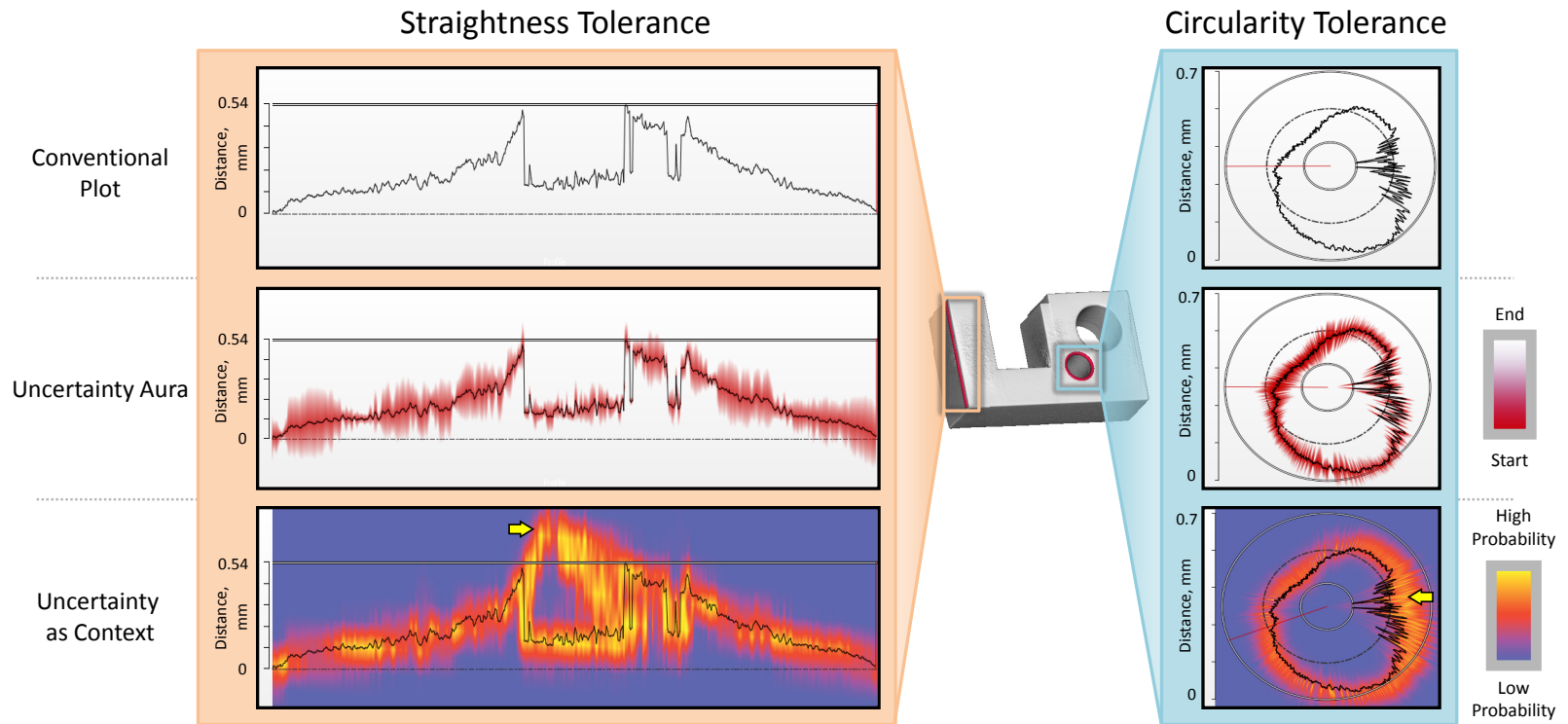


Figure 4.8: Visualizations of straightness and circularity measurement plots. Conventional, uncertainty aura, and uncertainty context visualizations are shown. The color map used for the uncertainty aura and for the uncertainty as context visualizations are shown on the right. A duct tape artifact is marked with an arrow in the straightness tolerance. A noisy measurement area is marked with an arrow in the circularity tolerance.

4.8 Measurement Plots

We propose several detailed visualization techniques in order to depict uncertainty information due to the statistical analysis. The goal of these visualizations is to provide domain experts with additional insight into the underlying uncertainty of the measurement. The proposed visual uncertainty representations are integrated into measurement plots which are commonly used for results display and evaluation (Figure 4.8). We enhance measurement plots with uncertainty information. We visualize the uncertainty of the measured points using an uncertainty aura (section 4.8.1). If a more detailed overview is needed, we visualize surrounding uncertainty as context (section 4.8.2). The measurement plots are interactive and allow to navigate to the points of interest. The straightness plot supports scaling and panning interactions. The circularity plot supports the scaling interaction only as the panning would not make sense here. The visual linking of the measurement plot and the 3D view is implemented using a *sliding pointer*. The sliding pointer highlights a selected probed point in both the 3D view and the measurement plot. An example of the sliding pointer can be seen in Figure 4.1. In the 3D view the pointer is represented as a red arrow indicating the selected point and aligned according to the probing direction. In the measurement plot the selected point is highlighted with a line. The position of the pointer is updated due to user interactions with the measurement plot.

4.8.1 Uncertainty Aura

Every measured point along the reference shape has its interface probability. This probability can be a good indication of the surface quality at the sampled point. Visualizing this probability provides the user with knowledge about how much this particular point of the measurement can be trusted. After the measurement has been performed and points were calculated, we sample the interface probability volume for every calculated point. Then we visualize this information around the plot profile line of a measurement plot. For this purpose we introduce the *uncertainty aura visualization*. This visualization conveys the fuzziness of the plot profile line by surrounding it with the aura-like interface probabilities. Examples of uncertainty aura visualization for the circular polar plot and the straightness plot are shown in Figure 4.8. The aura appears wider in the areas of the plot profile line with high uncertainty and narrower in the areas with smaller uncertainty. We vary the thickness of the aura in the probing direction. The thickness is in inverse proportion to the interface probability on the plot. The thicker the line is plotted, the lower is the interface probability, i.e., the higher is the uncertainty at this point. This way the plot profile line will have a very narrow aura if it has high interface probabilities. If interface probabilities are low the corresponding areas will be surrounded by a wide aura. For the straightness tolerance the thickness of the uncertainty aura is varied in the vertical direction which is perpendicular to the enclosing lines. For the circularity tolerance the thickness of the aura is varied in the direction to the center of the plot which is perpendicular to the enclosing circles. To achieve a smoother appearance and to reflect the fuzziness of the uncertainty information the transparency of the aura is increasing with increasing distance from the plot profile line.

4.8.2 Uncertainty as Context

Showing the interface probability of a measured point only can be insufficient in some cases. This visualization does not show how close the extracted surface is fitted to the areas with highest interface probabilities. Furthermore, in some cases showing the uncertainty distribution around the measurement profile can provide an expert with a better information on the reliability of the measurement and extracted surface. To achieve this we use the *uncertainty as context visualization*. Examples of uncertainty as context visualizations for the circular polar plot and the straightness plot are shown in Figure 4.8. First, we calculate an uncertainty context image and then use it as the background image for the measurement plot. To obtain the uncertainty context image we apply the following strategy of sampling the interface-probability volume. For every pixel of the measurement plot canvas we find the corresponding position in the 3D volume and sample the interface probability at this position. As the resolution of such a sampling can be significantly higher than the resolution of the interface probability volume, we use interpolation between 3D volume points to achieve a smooth appearance of the uncertainty context image. We map uncertainties to colors using a heat color map (Figure 4.8 right). The color mapping function window and level parameters can be interactively adjusted by the user in order to enhance the representation of areas with small interface probabilities. Representing the uncertainty context allows the user to visually estimate the uncertainty distribution around the measured points.

4.9 Implementation

Our visualizations were implemented as part of the iAnalyse framework. We use Qt [9] for custom measurement-plot widgets. We used the Visualization Toolkit (VTK) [64] for data visualization, surface extraction and probing the interface-probability volume. The statistical analysis steps were implemented as Image Processing Toolkit (ITK) [28] style filters.

4.10 Results

For the evaluation of the presented methods we used two specimens and a real world component. The first specimen is a multi-material component consisting of two materials: metal and plastic. This test part is a plastic cube with four drill holes: two larger ones and two smaller ones with steel pin insertions (Figure 4.9a). The data of this test part were obtained using a simulation of a 3DXCT scan. For the simulation we used the GPU-based 3DXCT simulation tool by Reiter et al. [42]. We will further refer to the first specimen as CUBE. We have downsampled the reconstructed 3D volume to a resolution of $256 \times 256 \times 256$ voxels to test our techniques on the low resolution noisy data. The second dataset was obtained from a real 3DXCT scan of an aluminium test part. Specimen two is a phantom used for evaluating beam hardening artifacts (Figure 4.9b). The resolution of this dataset is $984 \times 984 \times 884$ voxels. We will further refer to this specimen as TP09. The last specimen is a real-world industrial component with complex geometry. This test part is an aluminium oil filter housing (Figure 4.9c). The reconstructed

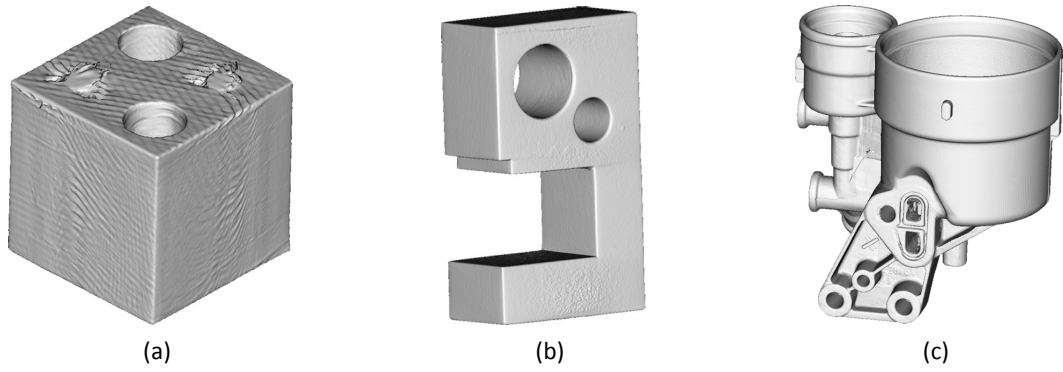


Figure 4.9: The CUBE (a), the TP09 (b), and the OFH (c) specimens.

volume has a resolution of $529 \times 771 \times 873$ voxels. We will further refer to this specimen as OFH.

The interface-probability volumes were computed and surface models were extracted for each dataset. For the surface extraction we used an isosurface-generation algorithm. The isovalues resulting in the best fitting to the actual surface position was manually selected. As stated any other more sophisticated surface extraction algorithm could be used as replacement. For the mentioned specimens we study a set of measurement features using the presented visualization techniques. In the following we evaluate the usefulness of our method and demonstrate potential use cases.

Reconstruction artifacts are present in all datasets. They appear as high frequency stripes all over the data (Figure 4.10a). The noise can be observed as periodic fluctuations of intensities on the surface of the specimen. Due to their very high frequencies and local presence only at the borders, reconstruction artifacts are hardly visible in the data. They require very careful window function adjustments to visually reveal their presence. However, these artifacts contribute significantly to the resulting measurement as additional periodic noise. A depiction of reconstruction artifacts for the straightness tolerance is shown in Figure 4.11. Periodic patterns in the uncertainty aura and uncertainty as context visualizations indicate the presence of reconstruction artifacts. In this case, the visualizations provide the user with additional insight into the data, which is not possible with default exploration techniques such as measurement plots and slice views.

Low contrast in the intensity values at the surface of the specimen appear in parts of the reconstructed volume due to 3DXCT artifacts like beam hardening. Artifacts-affected areas appear as *noisy regions* on the extracted isosurface. The noise will also appear in the plot profile line, hindering the evaluation of actual deviations. An example of such an area for the circularity tolerance is marked by an arrow in Figure 4.8 at on the right side of the circularity polar plot. In this case uncertainty as context visualization provides the user with information about where the actual surface of the noisy part is likely to be. In this example it can be seen that noise creates some outliers towards the center of the reference circle. The actual surface is more probably located at the outer side of the plot profile line.

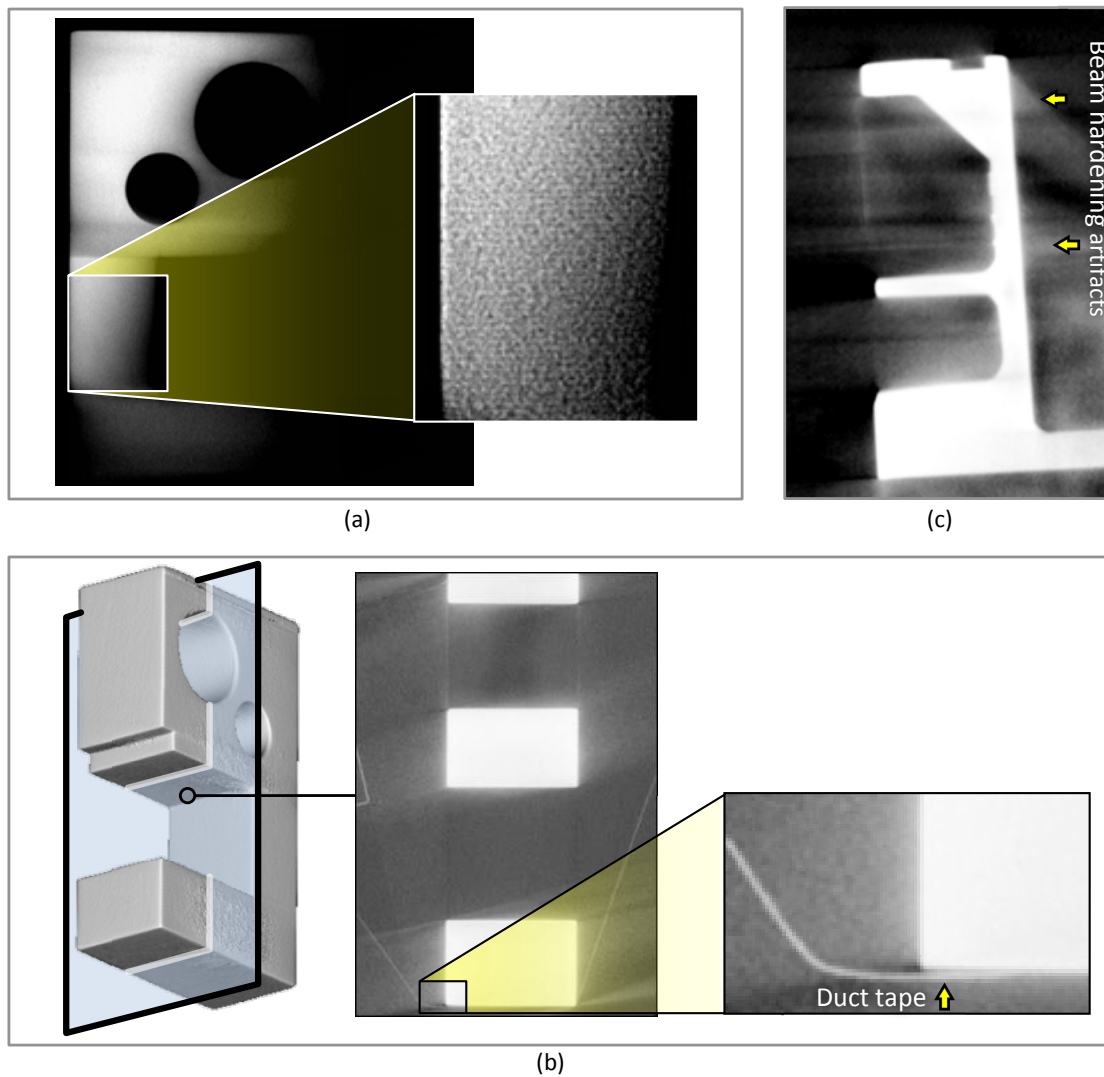


Figure 4.10: Various problems shown using slices through the original data. Reconstruction artifacts in the TP09 specimen (a), the duct tape in the TP09 specimen (b), and the beam-hardening artifacts in the OFH specimen (c). The contrast of the close-up image in (a) was enhanced for illustration purposes.

In some cases conventional measurement plots fail to provide the user with insight about the source of deviations. They only show the measurement plot profile line and do not provide any context information about surroundings of the profile. In Figure 4.8 on the straightness tolerance some abnormal variations in the middle section of the plot profile line are indicated by a yellow arrow. These variations are actually caused by a duct tape which was used by the technicians to fix the specimen on the rotary plate during scanning (Figure 4.10b). In the

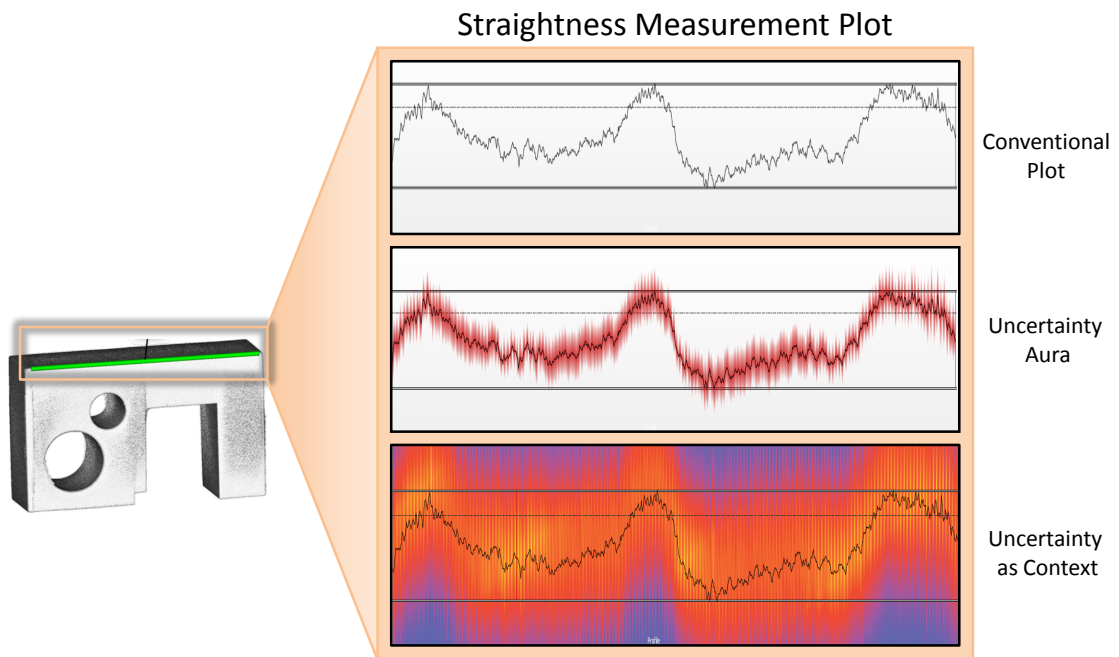


Figure 4.11: Depiction of reconstruction artifacts through different visualizations for the straightness tolerance. The TP09 specimen is used. Reconstruction artifacts are depicted as periodic noise.

middle of the measurement feature the duct tape closely approaches the actual surface of the specimen. This causes the extracted isosurface to change between the surface of the specimen and the surface of the duct tape. It can be seen in Figure 4.11 that this situation is reflected in the measurement plot with uncertainty as context visualization. In the uncertainty as context visualization for the straightness tolerance (Figure 4.8) two high probability zones appear. And the plot profile line significantly varies by jumping over from one probability zone to the other one. The provided visualization enables metrology experts to quickly identify the source of such abnormal behaviour and draw proper conclusions (e.g., changing the duct tape placement).

As the resulting reconstructed volume is affected by various types of artifacts, it is essential for the metrology experts to determine whether the measurement is affected by real defects of the industrial part or not. Additionally, excluding contributions to inhomogeneities caused by artifacts in the measurement result helps to provide more accurate metrology results. A manual collation with the original data is not appropriate as it is tedious and time consuming. The slice image illustrating beam-hardening artifacts in Figure 4.10c shows intensity inhomogeneities along the measurement. A straightness measurement performed in the region affected by beam-hardening artifacts in the OFH specimen is shown in Figure 4.12. The conventional measurement plot is not providing any information about *the reliability of different parts* of the measurement. In contrast, uncertainty as context visualization clearly depicts uncertain areas as blobs in the

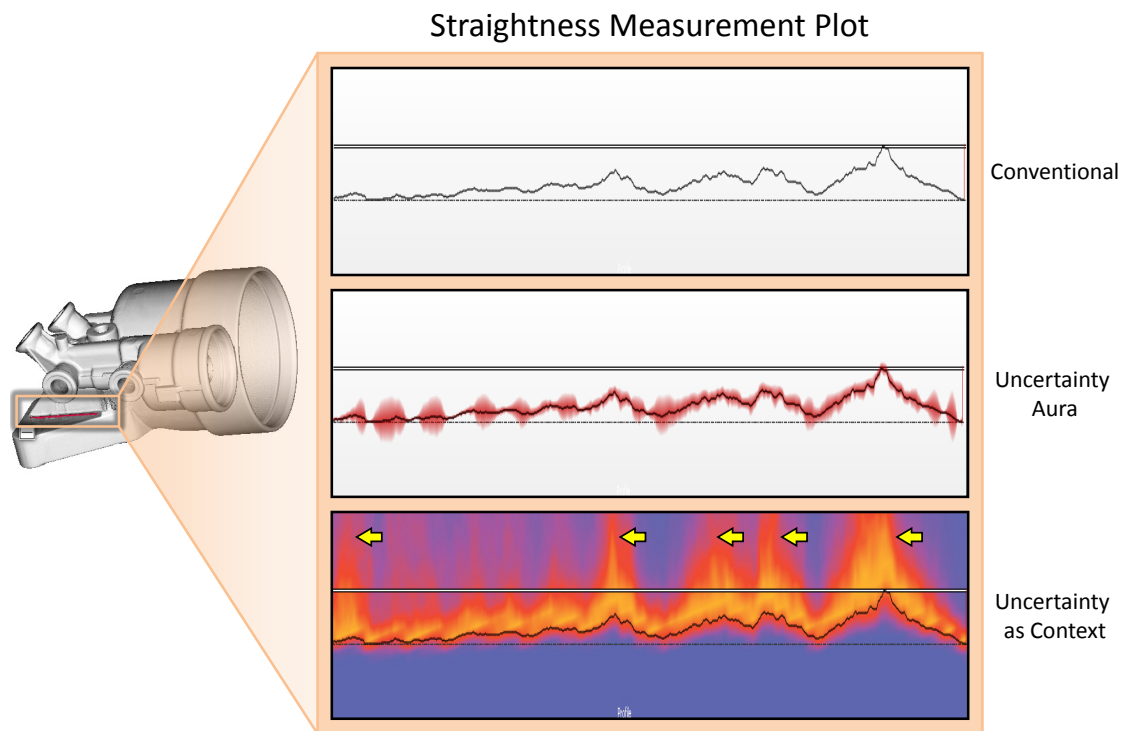


Figure 4.12: Depiction of reliable parts of the measurement by different visualizations for the straightness tolerance. The OHF specimen is used. Parts unreliable due to beam-hardening artifacts are marked with yellow arrows.

surrounding interface probabilities. Therefore, these areas can have high deviation values, and may be considered less reliable by the 3DXCT metrologists.

We collected *domain experts feedback* on the presented methods in collaboration with our company partner (Carl Zeiss Industrial Metrology, Oberkochen, Germany) and 3DXCT specialists of the computed tomography research group (Upper Austrian University of Applied Sciences, Wels, Austria) to evaluate the practical value of the proposed visualization techniques. Three experts from the company partner have participated. All of them are dealing with industrial 3DXCT metrology on a daily basis and have operational experiences for extended periods of time. Three experts from the CT research group have participated. Two of them are dealing with industrial 3DXCT metrology on a weekly basis and also have extended work experiences in the field. One 3DXCT expert was never involved in 3DXCT metrology tasks. The evaluation has assessed the following features:

- 3D labels enhanced with additional information
- reference shapes: deviation color coding and mapping uncertainty to thickness
- measurement plots: uncertainty aura and uncertainty as context visualizations

- interactivity of the measurement plots, e.g., scaling and panning
- visual linking of views using the picking of 3D labels and the sliding pointer.

The participants appreciated the idea of visualizing measurement information on the reference shapes. All the participants considered the deviation color coding on the reference shapes to be helpful or very helpful. The tubular representation of reference shapes themselves was perceived to be mostly neutral. The interactivity of the measurement plots was considered helpful by most participants. The scaling functionality of the circularity plot was considered especially important for the domain specialists. The scaling of the straightness plot was considered to be more useful than panning. All participants except one have felt that the idea of 3D labeling for providing an overview of measurements is very helpful. Two of three company experts have valued the visual linking of the measurement plot and 3D view employing the sliding pointer to be highly useful. Majority of experts have indicated that uncertainty visualizations for the measurement plots are only useful in certain cases. For example, in the case of low-resolution data, uncertainty representations were rated as unhelpful. One expert pointed out that uncertainty information is not useful in several cases due to the strong influence of reconstruction artifacts.

4.11 Conclusions

We have presented a 3DXCT metrology system which is reflecting the fuzziness of common geometric tolerances by accounting for the material interface probability of the industrial specimens. We use a novel statistical analysis approach for the reconstructed 3D volume data in order to estimate the probabilities of material-interface locations. The obtained uncertainty information is then incorporated into a set of visualizations which are extensions to techniques commonly used by the metrology domain experts. These visualizations provide the user with insight into measurement fuzziness and reliability while preserving the usual metrology workflow. The presented integrated visualizations provide information about the uncertainty of measurements on various levels of detail. Our system is implemented as an integrated tool performing data preprocessing and utilizing linked interactive views for support of exploration and visualization of the measurements' uncertainty. We test the presented methods using various specimens like simulated low-resolution datasets and high-resolution scanned datasets.

In this work we assume that probability distributions obtained from the Bayesian classification are independent. This is an approximation and can lead to the overestimation of the interface probabilities. Incorporating the estimation of correlations in the data is a promising topic for further research. In future work we want to include other geometric tolerances in our system. Additionally, there is a wide field for exploring various new 3D visualization techniques that reflect the fuzziness of tolerances such as flatness or cylindricity. Despite the mentioned limitations, the presented system shows promising results in providing domain metrology experts with insight into the uncertainty of the measurements which was not considered before. Taking this new information into account can help in improving 3DXCT geometric metrology and tolerancing and in achieving a more reliable quality control.

Summary

Taking advantage of expressive visualizations and computational methods enables faster and well-grounded 3DXCT scan data analysis and enhancement. Incorporating the tools addressed in the previous chapters during the different stages of the 3DXCT pipeline allows for an overall improvement of the final result and increases the confidence in its quality. In this work the following issues and parts of the 3DXCT workflow are targeted:

- scan parameters tuning
- material characterization of industrial MMCs
- minimization and reduction of 3DXCT artifacts
- performing measurements and geometric tolerancing using the data from 3DXCT scans

Three novel methods addressing these aspects of 3DXCT nondestructive testing and metrology were presented:

- **Optimal specimen placement for the 3DXCT scan.** The decision on the specimen position and orientation during the scanning process should be done prior to the scan. A good placement results in a significant improvement of the scan quality and reduces the amount of beam hardening artifacts and blurred planar faces. The tool discussed in Chapter 2 uses the 3D mesh model of the specimen to perform simulations. Ray casting and Radon-space analysis are employed for the simulation. The optimal placement is then derived from the resulting parameter space using parameter-exploration techniques. The introduced method allows fast finding of the optimal placement for specimens of any complexity and does not require any domain-specific knowledge from the user.
- **Metal-artifact reduction for multi-material components** is of high importance as many industrial components under inspection consist of multiple materials including metal and plastic. The presented technique uses 2D projections to reduce artifacts caused by metal

parts of the specimen. In Chapter 3 we address a pipeline utilizing 2D projections data and present preview-based visual analysis methods as well as methods to evaluate the artifact reduction effect. Applying this pipeline achieves a significant reduction of metal artifacts. It facilitates a higher quality of the subsequent material characterization and analysis.

- **Dimensional 3DXCT measurements** are often performed **on uncertain data**. During the 3DXCT pipeline there are many sources that contribute to the uncertainty of the data used for metrology and geometric tolerancing, e.g., artifacts, noise, and undersampling during the reconstruction. Moreover, the location of the surface is not explicitly available and is estimated from the 3D volumetric data using surface extraction algorithms. This implies positional uncertainty of the surface used for measurements. In Chapter 4 we present techniques which account for uncertainty arising in the 3DXCT metrology data flow. The proposed techniques provide expressive uncertainty visualizations and give an augmented insight into the reliability of geometric tolerances. The provided visualizations show metrology experts additional information on the local uncertainty of the measured features and enable interactive exploration and evaluation.

The techniques considered in this thesis resulted in three integrated systems for visual analysis and exploration of industrial 3DXCT scan data. These systems were implemented as parts of the iAnalyse basic framework, which is in-house developed software. The achieved results were evaluated with respect to metrology applications together with our company partners and domain experts of the computed tomography research group at the University of Applied Sciences – Upper Austria. The results were demonstrated and validated using test parts as well as real-world industrial components.

Concerning the detection of optimal specimen placements, at the moment there are no tools integrated into the 3DXCT workflow. An automation of the placement finding may enable faster scan preparation times along with a reduction of the estimated surface deviations and may enable improved measurement accuracies. To allow full automation additional research on finding the global function which optimizes placement is required. Furthermore the advancement of artifact reduction techniques is a promising way to permit previously impossible analysis of multi-material components containing both high and low X-ray absorbing materials. Making industrial 3DXCT applicable for nondestructive testing of such components is strongly increasing the versatility of the method and its acceptance by the NDT community. However, the uncertainty and errors introduced by artifact-reduction methods should be carefully evaluated and considered in the subsequent analysis. In the particular case of the 3DXCT workflow there is a wide range of computational methods and visualization techniques that can be applied to estimate data uncertainty and provide visual feedback. Applying tools of statistical analysis and expressive 2D and 3D uncertainty visualizations in order to enhance uncertainty awareness and to assure the reliability of measurements is a prominent and highly important field for future research.

There are still several open issues that are obstacles for a broader acceptance of industrial 3DXCT method in metrology and non destructive testing. Despite the increase in precision provided by modern 3DXCT metrology systems, in most cases it is still lower than the precision of common metrology tools. Furthermore, another important issue is the significant amount of

3DXCT artifacts, especially when multi-material components or highly absorbing materials are used. Finally, 3DXCT metrology strongly needs a standardization of its precision and underlying uncertainty of the measurements in order to generate an even broader acceptance in the industry.

Bibliography

- [1] Oxford Dictionaries. Oxford University Press. “quality”. <http://oxforddictionaries.com/definition/english/quality>. Accessed: 25/09/2012.
- [2] A. Amirkhanov, C. Heinzl, M. Reiter, J. Kastner, and E. Meister Gröller. Projection-Based Metal-Artifact Reduction for Industrial 3D X-ray Computed Tomography. *IEEE Transactions on Visualization and Computer Graphics*, 17(12):2193 – 2202, Dec. 2011.
- [3] A. Amirkhanov, C. Heinzl, M. Reiter, J. Kastner, and E. Meister Gröller. Evaluation of Projection-Based Metal-Artifact Reduction for Multi-Material Components. In *Conference on Industrial Computed Tomography (iCT 2012)*, pages 279 – 287, September 2012.
- [4] A. Amirkhanov, C. Heinzl, M. Reiter, and E. Meister Gröller. Visual Optimality and Stability Analysis of 3DCT Scan Positions. *IEEE Transactions on Visualization and Computer Graphics*, pages 1477 – 1487, Oct. 2010.
- [5] A. Amirkhanov, J. Kastner, E. Meister Gröller, and C. Heinzl. Fuzzy ct metrology: Dimensional measurements on uncertain data. Technical report, Institute of Computer Graphics and Algorithms, Vienna University of Technology, September 2012. Human contact: technical-report@cg.tuwien.ac.at.
- [6] J. Ball and A. Moore. *Essential Physics for Radiographers. 3rd ed.* Blackwell Science, Oxford, 1997.
- [7] J. F. Barrett and K. Nicholas. Artifacts in CT: Recognition and avoidance. *Radiographics ISSN 0271-5333*, vol. 24(6):1679 – 91, 11 2004.
- [8] W. Berger, H. Piringer, P. Filzmoser, and E. Gröller. Uncertainty-Aware Exploration of Continuous Parameter Spaces Using Multivariate Prediction. *Computer Graphics Forum*, 30(3):911 – 920, June 2011.
- [9] J. Blanchette and M. Summerfield. *C++ GUI Programming with Qt 4*. Prentice Hall Press, Upper Saddle River, NJ, USA, second edition, 2008.
- [10] U. D. Bordoloi and H.-W. Shen. View Selection for Volume Rendering. *Visualization Conference, IEEE*, 2005.

- [11] L. Cartz. *Nondestructive testing: radiography, ultrasonics, liquid penetrant, magnetic particle, eddy current*. ASM International, 1995.
- [12] T. F. Chan and J. Shen. Mathematical models for local nontexture inpaintings. *SIAM J. Appl. Math.*, 62:1019 – 1043, 2002.
- [13] A. Coninx, G. Bonneau, J. Droulez, and G. Thibault. Visualization of uncertain scalar data fields using color scales and perceptually adapted noise. *Applied Perception in Graphics and Visualization*, 2011.
- [14] S. Djurcilov, K. Kim, P. Lermusiaux, and A. Pang. Visualizing scalar volumetric data with uncertainty. *Computers & Graphics*, 26(2):239 – 248, Apr. 2002.
- [15] X. Duan, L. Zhang, Y. Xiao, J. Cheng, Z. Chen, and Y. Xing. Metal artifact reduction in CT images by sinogram TV inpainting. In *Nuclear Science Symposium Conference Record, 2008. NSS '08. IEEE*, pages 4175 – 4177, 10 2008.
- [16] L. A. Feldkamp, L. C. Davis, and J. W. Kress. Practical cone-beam algorithm. *J. Opt. Soc. Am. A*, 1(6):612 – 619, June 1984.
- [17] N. Freud, J.-M. Létang, and D. Babot. *A hybrid approach to simulate multiple photon scattering in X-ray imaging, Nuclear Instruments and Methods in Physics Research*. Elsevier, Amsterdam, PAYS-BAS (1984) (Revue), 2005.
- [18] G. Grigoryan and P. Rheingans. Point-based probabilistic surfaces to show surface uncertainty. *IEEE Transactions on Visualization and Computer Graphics*, 10(5):564 – 573, 2004.
- [19] M. Hadwiger, F. Laura, C. Rezk-Salama, T. Holtt, G. Geier, and T. Pabel. Interactive Volume Exploration for Feature Detection and Quantification in Industrial CT Data. *IEEE Transactions on Visualization and Computer Graphics*, 14(6):1507 – 1514, 11 – 12 2008.
- [20] C. Heinzl. *Analysis and Visualization of Industrial CT Data*. PhD thesis, Institute of Computer Graphics and Algorithms, Vienna University of Technology, 12 2009.
- [21] C. Heinzl, J. Kastner, A. Amirkhamov, E. Meister Gröller, and C. Gusenbauer. Optimal Specimen Placement in Cone Beam X-ray Computed Tomography. *NDT&E International*, 50(0):42 – 49, 2012.
- [22] C. Heinzl, J. Kastner, T. Möller, and M. E. Gröller. Statistical Analysis of Multi-Material Components using Dual Energy CT. In D. S. Oliver Deussen, Daniel Keim, editor, *VMV'08: Vision, Modeling and Visualization 2008*, pages 179 – 188, 10 2008.
- [23] G. Henzold. *Geometrical dimensioning and tolerancing for design, manufacturing and inspection: a handbook for geometrical product specifications using ISO and ASME standards*. Butterworth-Heinemann, 2006.

- [24] G. T. Herman. Correction for beam hardening in computed tomography. *Physics in Medicine and Biology*, 24(1):81, 1979.
- [25] F. Hopkins, Y. Du, B. Lasyuk, A. Abraham, and S. Basu. Analytical corrections for beam-hardening and object scatter in volumetric computed tomography systems. In *WCNDT*, volume 22, pages 462 – 468, 2004.
- [26] J. Hsieh. *Computed Tomography: Principles, Design, Artifacts and Recent Advances*. SPIE Press, 2 2003.
- [27] R. Huang, K.-L. Ma, P. McCormick, and W. Ward. Visualizing Industrial CT Volume Data for Nondestructive Testing Applications. *Visualization Conference, IEEE*, page 72, 2003.
- [28] L. Ibanez, W. Schroeder, L. Ng, and J. Cates. *The ITK Software Guide*. Kitware, Inc. ISBN 1-930934-15-7, <http://www.itk.org/ItkSoftwareGuide.pdf>, second edition, 2005.
- [29] G.-R. Jaenisch, C. Bellon, U. Samadurau, M. Zhukovskiy, and S. Podoliako. A Monte Carlo Model Coupled to CAD for Radiation Techniques. *European Conference for NDT 2006*, 2006.
- [30] C. Johnson. Top scientific visualization research problems. *Computer Graphics and Applications, IEEE*, 24(4):13 – 17, 7-8 2004.
- [31] W. A. Kalender, R. Hebel, and J. Ebersberger. Reduction of CT artifacts caused by metallic implants. *Radiology*, 164(2):576 – 7, 1987.
- [32] S. Kasperl. *Qualitätsverbesserungen durch referenzfreie Artefaktreduzierung und Oberflächennormierung in der industriellen 3D-Computertomographie*. PhD thesis, Technische Fakultät der Universität Erlangen Nürnberg, 2005.
- [33] S. Kasperl. *Qualitätsverbesserungen durch referenzfreie Artefaktreduzierung und Oberflächennormierung in der industriellen 3D-Computertomographie*. PhD thesis, Friedrich-Alexander Universität Erlangen-Nürnberg, 2005.
- [34] S. Kasperl, I. Bauscher, U. Hassler, H. Markert, and S. Schröpfer. Reducing Artifacts in Industrial 3D Computed Tomography (CT). In *VMV'08: Vision, Modeling and Visualization 2008*, pages 51–57, 2002.
- [35] R. Keys. Cubic convolution interpolation for digital image processing. *IEEE Transactions on Acoustics, Speech and Signal Processing*, 29(6):1153 – 1160, 12 1981.
- [36] J. Kniss, R. Van Uitert, A. Stephens, G. Li, T. Tasdizen, and C. Hansen. Statistically quantitative volume visualization. *Visualization Conference, IEEE*, VI:37 – 37, 2005.
- [37] M. Krumm, S. Kasperl, and M. Franz. Reducing non-linear artifacts of multi-material objects in industrial 3D computed tomography. *NDT & E International*, 41(4):242 – 251, 2008.

- [38] J. Kruth, P. Vanherck, and C. Van Den Bergh. Compensation of static and transient thermal errors on CMMs. *Annals of the CIRP, Paris*, 50(1):377 – 380, 2001.
- [39] J. P. Kruth, M. Bartscher, S. Carmignato, R. Schmitt, L. De Chiffre, and A. Weckenmann. Computed tomography for dimensional metrology. *CIRP Annals Manufacturing Technology*, 60(2):821 – 842, 2011.
- [40] C. Lundström, P. Ljung, A. Persson, and A. Ynnerman. Uncertainty visualization in medical volume rendering using probabilistic animation. *IEEE Transactions on Visualization and Computer Graphics*, 13(6):1648 – 55, 2007.
- [41] C. Lundström, P. Ljung, and A. Ynnerman. Local histograms for design of transfer functions in direct volume rendering. *IEEE Transactions on Visualization and Computer Graphics*, 12(6):1570 – 9, 2006.
- [42] M. Reiter and M. Mantler and B. Chyba. McRay - A Monte Carlo Simulation of Projections in Computed Tomography. *Denver X-ray Conference 2007, Denver (US)*, 7-8 2007.
- [43] A. M. MacEachren, A. Robinson, S. Hopper, S. Gardner, R. Murray, M. Gahegan, and E. Hetzler. Visualizing Geospatial Information Uncertainty: What We Know and What We Need to Know. *Cartography and Geographic Information Science*, 32(3):139 – 160, July 2005.
- [44] M. M. Malik, C. Heinzl, and M. E. Gröller. Comparative Visualization for Parameter Studies of Dataset Series. *IEEE Transactions on Visualization and Computer Graphics*, 99, 2010.
- [45] K. Matkovic, H. Hauser, R. Sainitzer, and M. E. Gröller. Process Visualization with Levels of Detail. In *IEEE Symposium on Information Visualization 2002*, pages 67 – 70. IEEE Computer Society Press, 2002.
- [46] M. Mlejnek, P. Ermes, A. Vilanova, R. van der Rijt, H. van den Bosch, F. Gerritsen, and M. E. Gröller. Profile Flags: a Novel Metaphor for Probing of T2 Maps. In *Proceedings of IEEE Visualization 2005*, pages 599 – 606. IEEE CS, Oct. 2005.
- [47] M. Mlejnek, P. Ermes, A. Vilanova, R. van der Rijt, H. van den Bosch, M. E. Gröller, and F. Gerritsen. Application-Oriented Extensions of Profile Flags. In *Proceedings of Eurographics / IEEE VGTC Symposium on Visualization*, pages 339 – 346. IEEE CS, 2006.
- [48] K. Mühler, M. Neugebauer, C. Tietjen, and B. Preim. Viewpoint Selection for Intervention Planning. In K. Museth, T. Möller, and A. Ynnerman, editors, *EuroVis*, pages 267–274. Eurographics Association, 2007.
- [49] NVIDIA. CUDA Programming Guide 2.3, 2009. Accessed: 08/09/209.
- [50] M. Oehler and T. M. Buzug. Sinogram Inpainting for Metal Artifact Reduction in CT Images. In *Proc. 4th European Congress for Medical and Biomedical Engineering, Springer IFMBE Series*, volume 22, pages 651 – 654, 2008.

- [51] S. Owada, F. Nielsen, and T. Igarashi. Volume catcher. In *I3D '05: Proceedings of the 2005 symposium on Interactive 3D graphics and games*, pages 111 – 116, New York, NY, USA, 2005. ACM.
- [52] M. Pauly, N. Mitra, and L. Guibas. Uncertainty and variability in point cloud surface data. In *Eurographics symposium on point-based graphics*, volume 84, 2004.
- [53] T. Pfaffelmoser, M. Reitinger, and R. Westermann. Visualizing the Positional and Geometrical Variability of Isosurfaces in Uncertain Scalar Fields. *Computer Graphics Forum*, 30(3):951 – 960, June 2011.
- [54] S. Popov, J. Günther, H.-P. Seidel, and P. Slusallek. Stackless kd-tree traversal for high performance GPU ray tracing. *Computer Graphics Forum*, 26(3):415–424, Sept. 2007. (Proceedings of Eurographics).
- [55] K. Pöthkow and H.-C. Hege. Positional Uncertainty of Isocontours: Condition Analysis and Probabilistic Measures. *IEEE Transactions on Visualization and Computer Graphics*, 17(10):1393 – 1406, oct. 2011.
- [56] K. Pöthkow, B. Weber, and H.-C. Hege. Probabilistic Marching Cubes. *Computer Graphics Forum*, 30(3):931 – 940, June 2011.
- [57] J.-S. Prassni, T. Ropinski, and K. Hinrichs. Uncertainty-aware guided volume segmentation. *IEEE Transactions on Visualization and Computer Graphics*, 16(6):1358 – 65, 2010.
- [58] J. Radon. *Über die Bestimmung von Funktionen durch Ihre Integralwerte laengs gewisser Mannigfaltigkeiten*. Berichte über die Verhandlungen der Sächsische Akademie der Wissenschaften, 1917.
- [59] V. Rebuffel and J.-M. Dinten. Dual-Energy X-Ray Imaging: Benefits and Limits. In *European Conference on Non Destructive Testing (CD-ROM)*, 2006.
- [60] M. Reiter, M. M. Malik, C. Heinzl, D. Salaberger, M. E. Gröller, H. Lettenbauer, and J. Kastner. Improvement of X-Ray image acquisition using a GPU based 3DCT simulation tool. In *International Conference on Quality Control by Artificial Vision*, 5 2009. not peer reviewed, will appear.
- [61] P. Rheingans and S. Joshi. Visualization of molecules with positional uncertainty. In *Data Visualization '99, Proceedings of the Joint EUROGRAPHICS - IEEE TCVG Symposium on Visualization*, volume 99, pages 299 – 306. Springer-Verlag, 1999.
- [62] P. Rhodes, R. Laramée, R. Bergeron, and T. Sparr. Uncertainty visualization methods in isosurface rendering. In *Eurographics*, pages 83 – 88, 2003.
- [63] A. Saad, G. Hamarneh, and T. Möller. Exploration and visualization of segmentation uncertainty using shape and appearance prior information. *IEEE Transactions on Visualization and Computer Graphics*, 16(6):1366 – 75, 2010.

- [64] W. Schroeder, K. Martin, and B. Lorensen. *The Visualization Toolkit, Third Edition*. Kitware Inc., 2007.
- [65] X. Shao, Z. Liu, and H. Li. An Image Inpainting Approach Based on the Poisson Equation. In *Proceedings of the Second International Conference on Document Image Analysis for Libraries*, pages 368 – 372. IEEE Computer Society, 2006.
- [66] J. Shen and T. F. Chan. Mathematical models for local nontexture inpaintings. *SIAM Journal on Applied Mathematics*, 62(3):1019 – 1043, 12 2002.
- [67] L. A. Shepp and B. F. Logan. The Fourier Reconstruction of a head section. *IEEE Transactions on Nuclear Science*, NS-21(3):21 – 43, 1974.
- [68] B. Shneiderman. The Eyes Have It: A Task by Data Type Taxonomy for Information Visualizations. In *Proceedings of the 1996 IEEE Symposium on Visual Languages*, VL '96, pages 336 – 343, Washington, DC, USA, 1996. IEEE Computer Society.
- [69] B. D. Smith. Image reconstruction from cone-beam projections: necessary and sufficient conditions and reconstruction methods. *IEEE Transactions on Medical Imaging*, 4(1):14 – 25, 1985.
- [70] J. Tabary, R. Guillemaud, F. Mathy, A. Glière, and P. Hugonnard. Combination of high resolution analytically computed uncollided flux images with low resolution Monte-Carlo computed scattered flux images. *Proc. IEEE-MIC, Norfolk*, pages 551 – 558, 11 2002.
- [71] S. Takahashi and Y. Takeshima. A Feature-Driven Approach to Locating Optimal Viewpoints for Volume Visualization. In *IEEE Visualization*, pages 495 – 502. IEEE Press, 2005.
- [72] P. Thévenaz, T. Blu, and M. Unser. Interpolation revisited. *IEEE Transactions on Medical Imaging*, 19(7):739 – 758, 7 2000.
- [73] M. Tory and C. Swindells. Comparing ExoVis, Orientation Icon, and In-Place 3D Visualization Techniques. In *Graphics Interface '03*, pages 57 – 64, 2003.
- [74] H. K. Tuy. An Inversion Formula for Cone-Beam Reconstruction. *SIAM Journal on Applied Mathematics*, 43(3):546 – 552, 1983.
- [75] P.-P. Vázquez, M. Feixas, M. Sbert, and W. Heidrich. Viewpoint Selection using Viewpoint Entropy. In *VMV '01: Vision Modeling and Visualization 2001*, pages 273 – 280, 2001.
- [76] W. J. H. Veldkamp, R. M. S. Joemai, A. J. van der Molen, and J. Geleijns. Development and validation of segmentation and interpolation techniques in sinograms for metal artifact suppression in CT. *Medical Physics*, 37(2):620 – 8, 2010.
- [77] I. Viola, M. Feixas, M. Sbert, and M. E. Gröller. Importance-Driven Focus of Attention. *IEEE Transactions on Visualization and Computer Graphics*, 12(5):933 – 940, Oct. 2006.

- [78] J. Waser, H. Ribić, R. Fuchs, C. Hirsch, B. Schindler, G. Blöschl, and E. Gröller. Nodes on Ropes: A Comprehensive Data and Control Flow for Steering Ensemble Simulations. *IEEE Transactions on Visualization and Computer Graphics*, 17(12):1872 – 1881, December 2011.
- [79] F. Xu and K. Mueller. Ultra-Fast 3D Filtered Backprojection on Commodity Graphics Hardware. *IEEE International Symposium on Biomedical Imaging (ISBI '04)*, pages 571 – 574, 4 2004.
- [80] F. Xu and K. Mueller. Real-time 3d computed tomographic reconstruction using commodity graphics hardware. *Physics in Medicine and Biology*, 52:3405 – 3419, 2007.
- [81] H. Xue, L. Zhang, Y. Xiao, Z. Chen, and Y. Xing. Metal artifact reduction in dual energy CT by sinogram segmentation based on active contour model and TV inpainting. In *Nuclear Science Symposium Conference Record (NSS/MIC), 2009 IEEE*, pages 904 – 908, 11 2009.
- [82] L. Yu, J. Kofler, X. Liu, A. Primak, and C. McCollough. Automatic Metal Artifact Reduction From Reformatted Projections in Multi-Slice Helical CT. *Medical Physics*, 35:2949, 2008.
- [83] L. Zhu, J. Starman, and R. Fahrig. An Efficient Estimation Method for Reducing the Axial Intensity Drop in Circular Cone-Beam CT. *International Journal of Biomedical Imaging*, vol. 2008, 8 2008.
- [84] T. Zuk and S. Carpendale. Theoretical analysis of uncertainty visualizations. In *Proceedings of SPIE*, volume 6060, pages 66 – 79, 2006.

Curriculum Vitae



Contact Information

Name	Artem Amirkhanov
Address	Röttergasse 20/5, 1170 Vienna, Austria
E-mail	artem@cg.tuwien.ac.at

Personal Details

Date of Birth	February 17 th , 1987
Place of Birth	Ufa, Russia
Citizenship	Russian
Sex	Male
Languages	Russian (native), English (fluent)

Education

- 1994 – 2004 Lycee no. 5, Ufa, Russia
Secondary education. Finished with distinction (golden medal).
- 2004 – 2009 Ufa State Aircraft Technology University, Ufa, Russia
Master’s studies (computer science). Successfully completed the master’s thesis with distinction (red diploma).
Faculty: Computational Mathematics and Cybernetics
Specialty: Mathematics and Computer Science
- 2009 – Institute of Computer Graphics and Algorithms, Faculty of informatics, Vienna University of Technology, Austria **Doctoral studies (computer science).** Dissertation in the area of “ Visualization of Industrial 3DXCT Data” Supervisors: Ao.Univ.Prof. Dipl.-Ing. Dr. techn. Eduard Gröller, Dipl.-Ing. (FH) Dr. techn. Christoph Heinzl.

Employment History

- Nov. 2006 – Feb. 2009 Institute of Computer Research, Ufa, Russia
Programmer. Visualization of 3D GeoData for oil fields.
- Oct. 2009 – present Institute of Computer Graphics and Algorithms, Vienna University of Technology, Vienna, Austria **Research assistant.** Visualization and analysis of industrial 3DXCT data.

Publications

A. Amirkhanov, C. Heinzl, M. Reiter and M. E. Gröller. Visual Optimality and Stability Analysis of 3DCT Scan Positions, *IEEE Transactions on Visualization and Computer Graphics*, 16(6): 1477 – 86, Oct. 2010

A. Amirkhanov, C. Heinzl, M. Reiter, J. Kastner, and M. E. Gröller. Projection-Based Metal-Artifact Reduction for Industrial 3D X-ray Computed Tomography, *IEEE Transactions on Visualization and Computer Graphics*, pages 1477 – 1487, December 2011.

C. Heinzl, J. Kastner, A. Amirkhanov, E. Gröller, C. Gusenbauer, Optimal Specimen Placement in Cone Beam X-ray Computed Tomography, *NDT &E International*, 50(0): 42 – 49, 2012.

A. Amirkhanov, C. Heinzl, M. Reiter, J. Kastner, and M. E. Gröller. Evaluation of Projection-Based Metal-Artifact Reduction for Multi-Material Components, *Proc. of Conference on Industrial Computed Tomography (iCT 2012)*, Wels, Austria, pages 279 – 287, September 2012.

A. Amirkhanov, J. Kastner, E. Meister Gröller, and C. Heinzl. Fuzzy ct metrology: Dimensional measurements on uncertain data. *Technical report, Institute of Computer Graphics and Algorithms, Vienna University of Technology*, September 2012. Human contact: technical-report@cg.tuwien.ac.at.

A. Amirkhanov, S. Bruckner, C. Heinzl, E. Meister Gröller. The Haunted Swamps of Heuristics: Uncertainty in Problem Solving. *Technical report, Institute of Computer Graphics and Algorithms, Vienna University of Technology*, September 2012. Human contact: technical-report@cg.tuwien.ac.at.